# Peptide and Drug Interactions in Murine Models

*In vitro and in vivo studies with Microphysiometry, Confocal Microscopy and Functional Magnetic Resonance Imaging.*

INAUGURALDISSERTATION

zur

Erlangung der Würde eines Doktors der Philosophie

vorgelegt der

Philosophisch-Naturwissenschaftlichen Fakultät

der Universität Basel

von

Pierluigi Nervi

aus Bodio, Canton Ticino

Basel, 2004

Genehmigt von der Philosophisch-Naturwissenschaftlichen Fakultät auf Antrag von
Prof. Dr. Joachim Seelig, PD Dr. Anna Seelig and PD Dr. Markus Rudin

Basel, den 28. September 2004

Prof. Dr. Marcel Tanner
Dekan

*‘Commonplace as such experiments have become in our laboratories, I have not yet lost that sense of wonder, and of delight, that this delicate motion should reside in all ordinary things around us, revealing itself only to him who looks for it’*

*(E.M. Purcell, Nobel Lecture, 1952)*

# Table of Contents

# Abbreviations and Constants

| | |
|---|---|
| (Q)SAR | (quantitative) structure-activity relationships |
| ATP | adenosine triphosphate |
| ABC | ATP binding cassette |
| BOLD | blood oxygenation level dependent |
| BSA | bovine serum albumin |
| CBF | cerebral blood flow |
| $CBV_{rel}$ | relative cerebral blood volume |
| CMC | critical micellar concentration |
| CMRglu / $O_2$ | cerebral glucose / oxygen consumption |
| CNR | contrast-to-noise ratio |
| CNS | central nervous system |
| CPP | cell-penetrating peptide |
| DHb | deoxyhemoglobin |
| DMEM | Dulbecco's modified Eagle medium |
| DMSO | dimethylsulfoxide |
| ECAR | extracellular acidification rate |
| EDTA | ethylenediaminetetraacetic acid |
| EU | energy units |
| FACs | fluorescence activated cell sorting (cytometry technique) |
| FBS | fetal bovine serum |
| Fg | fluorescent FITC bound to a spacer peptide g |
| Fg-TATP | fluorescent peptide Fg linked to TATP |
| FITC | fluorescein isothiocyanate |
| FMRI | functional magnetic resonance imaging |
| FOV | field of view |
| g | spacer peptide ((βA)GGGG) used for linking FITC to TATP |
| GABA | γ (gamma)-aminobutyric acid |
| GAGs | glycosaminoglycans |
| GRE | gradient echo |
| HIV | human immunodeficiency virus |
| HS | heparan sulfate |
| HSPG | heparan sulfate proteoglycans |

| | |
|---|---|
| IMEM | Iscove's modified Eagle medium |
| ISFET | ion sensitive field effect transistor |
| ITC | isothermal titration calorimetry |
| LAPS | light-addressable potentiometric sensor |
| MDR | multidrug resistance |
| MOS-FET | metal oxide semiconductor-field effect transistor |
| MTX | matrix |
| $N_A$ | Avogadro's number: $N_A = 6.023 \cdot 10^{23}$ $mol^{-1}$ |
| Pgp | P-glycoprotein |
| $PtcO_2/CO_2$ | transcutaneous oxygen/carbon dioxide tension |
| PTD | protein transduction domain |
| R | universal gas constant R = 8.31 $J \cdot mol^{-1} \cdot K^{-1}$ |
| $R_1$ | spin-lattice or longitudinal relaxivity ($=1/T_1$) |
| $R_2$ | spin-spin or transverse relaxivity ($=1/T_2$) |
| $R_2^*$ | effective spin-spin relaxivity ($=1/T_2^*$) |
| RARE | rapid acquisition with relaxation enhancement |
| RF | radiofrequency |
| ROI | region of interest |
| SE | spin echo |
| $T_1$ | longitudinal relaxation time |
| $T_2$ | transverse relaxation time |
| $T_2^*$ | effective transverse relaxation time |
| TAT | trans-acting activator of transcription |
| TATP | PTD peptide (YGRKKRRQRRR) of HIV-1 TAT |
| TE | echo time |
| TMD | trans-membrane domain |
| TR | repetition time |

# Foreword

During the present thesis, I had the occasion to study living mammalian cells with biophysical techniques that allowed me the fascinating observation of life through the eyes of modern science. What the physicists Heisenberg and Schrödinger postulated in 1926 for the observation of electrons ("The observation itself changes the probability function discontinuously") can be extended to many fields of experimental research, and was certainly true for the observations reported in the present thesis: although the experiments were conducted in living cells, the observation itself required conditions that altered the life of the studied cells. For example, the observation of the entire organism with fMRI required the application of an anaesthetic; the superfusion of the cells in the microphysiometer proceeded with a blood substitute and at different partial gas pressures than found in the body; etc. Such experimental variations are integral part of the observation and the consequences of such conditions are addressed also in the present thesis.

In the last period of my work, I had the chance to work with living mice. Such models are nowadays routinely used for pre-clinical studies in the development of medical drugs and represent a fundamental step preceding phase I clinical trials. Especially the genetic elimination of a single protein (transgenic models) became a helpful tool to study the effects of such proteins on the entire organism and handling of diseases. However, such kind of animal experimentation is subjected to ethical and moral considerations on our rights, as humans, in exploiting other living organisms for our own profits.

While a complete abolition of animal experimentation seems to be utopian at the moment, a concrete effort can actually be done to reduce the number of animals needed for an experiment, to refine the methods employed for the investigation and, where possible, to replace animals with alternative models. Such biocentric, or at least less anthropocentric, philosophy is currently officially adopted by the Swiss Federal Law, and advertised under the acronym RRR (Refine, Reduce, Replace). In the last part of the thesis, it was my intention to actively take part to the RRR effort, by contributing to the development and adaptation of less invasive techniques for animal experimentation.

In summary, it was an interesting experience for me to study the diversity of metabolic responses in animal systems such as living cultured cells and mice, which allowed me to acquire experimental knowledge of the link between basic and preclinical biomedical research.

# Summary

The present thesis describes in three parts how living cells can be investigated on different biological levels, and how these techniques can be used to non-invasively evaluate the effect of drugs in the context of biomedical and pharmaceutical research.

In the first part, Pgp activation is studied in living cells studied in culture. Here, microphysiometry, monolayer techniques and computer modeling were applied to investigate the interaction of drugs with human P-glycoprotein (Pgp). Pgp is a transmembrane ABC-transporter that protects cells from a wide variety of toxic substances. Pgp is helpful under most biological conditions since it provides natural protection from toxins, but its activity can lead to resistance development in chemotherapy e.g. of cancers and microbes. In particular, the reported techniques provided a novel method to study Pgp-substrate interactions in real-time and in living murine cellular systems in which human Pgp have been expressed. Investigation of Pgp-substrate interactions is then extended to the structure-activity relationships (SAR) of potential Pgp substrates, on the basis of a recognition mechanism based on intramolecular hydrogen bond acceptor patterns.

In the second part, living cultured murine cells were studied under the influence of cell penetrating peptides (CPPs). CPPs are a class of compounds that traverse biological membranes very efficiently, although the precise uptake mechanism is not yet known. Elucidation of the exact uptake mechanism is, however, of great interest, given the potential of this class of compounds for pharmacological and biotechnological purposes. A CPP derived from the HIV-1 peptide TAT was studied using fluorescence confocal microscopy and microphysiometry as principal techniques.

In the third part of the thesis, the biological observation level was switched from living cells in culture to the entire organism using magnetic resonance imaging as a non-destructive method to observe biological effects of drugs. In pharmaceutical research the development of a commercial compound requires similar observation levels during the long evaluation process starting from high throughput screening of potential bioactive molecules and ending with the launch of one selected therapeutically successful product. The intermediate steps include basic *in vitro* studies, *in vivo* experimentation with cell culture, pre-clinical assays

with intact animal models and phase I-III clinical trials with humans. For ethical and practical reasons, major attempts are made to replace invasive animal models by non-invasive techniques that can be applied in the same way to the clinical research providing thus a smooth transition between pre-clinical and clinical phases. This last part of the thesis adapts and optimizes such a recent imaging method to detect brain activation non-invasively in mice and to allocate the activated brain areas in mice without the need for surgery.

In particular, the study focused on the activation of metabotrobic GABA(B) receptors in the mouse brain, upon stimulation with baclofen. The technical goal of this project was to adapt functional magnetic resonance imaging (fMRI) protocol at high field (7T) to the small size of the murine brain. The biological goal was to characterize regions in the brain, that show an enhanced activity under the influcence of baclofen - a know stimulator of GABAB receptors.

# Part One: P-Glycoprotein

## Foreword and Context of the Project

A search with the headword "P-glycoprotein" using the common biomedical database pubmed (www.pubmed.org) results in currently (2003) over 7000 scientific publications. This simple example gives a coarse, yet indicative illustration of the interest in this molecule and the effort research has made up to now, June 2003, to understand its function.

P-glycoproteins or Pgps (P stays for permeability) belong to the superfamily of ATP-binding cassette (ABC) proteins, also called ABC transporters or traffic ATPases. The general function of ABC transporters is to transport a large variety of chemicals (from peptides to simple ions) through biological lipid membranes against their concentration gradients, at the expense of ATP hydrolysis.

The ABC transporter superfamily is a large gene family that has been highly conserved during evolution (Miyauchi et al., 1992), and which pertains to organisms from different phyla, from prokaryotes to eukayrotes (Descoteaux et al., 1992). It includes 51 members in humans, 55 in flies, 129 in plants and over 300 in bacteria so far (Cai and Gros, 2003).

Human P-glycoprotein (Juliano et al., 1976; Juliano and Ling, 1976; Kartner et al., 1983; Riordan et al., 1985) is a 170 kDa integral protein composed of two homologous halves, each containing six putative transmembrane domains (TMDs) and an ATP-binding site, separated by a flexible linker polypeptide (Ambudkar et al., 1999). Pgp carries few N-linked glycosylation sites on the extracellular loop joining TMD 1 and TMD 2, and four intracellular phosphorylation sites on the linker domain between TMD 6 and TMD 7 (Figure I.1).

Human Pgp is the product of the MDR1 gene, cloned for the first time in 1986 by Chen et al. (Chen et al., 1986). In the same year, similar genes were sequenced from mice (*mdr 1a* (*mdr 3*)*, mdr 1b* (*mdr 1*) and *mdr 2*) (Gros et al., 1986; Gros et al., 1986) and hamsters (Gerlach et al., 1986), showing pronounced homology in the amino acid sequences.

MDR genes owe their names to a phenomenon called multidrug resistance (MDR). The origins of the MDR phenotype are manifold (Beck, 1989; Cole et al., 1992; Cole et al., 1994; Endicott and Ling, 1989; Gottesman and Pastan, 1993), but the expression of Pgp on cancer

cell surfaces is probably the most studied among them. Such phenotypic peculiarities were reported first by Biedler and Riehm (Biedler and Riehm, 1970), who demonstrated that Chinese hamster cells selected for resistance to actinomycin D became also simultaneously resistant to puromycin, vincristine, vinblastine, mithramycin, daunorubicin, mitomycin C and demecolcine. With the appearance of MDR, tumor cells acquire resistance against a great variety of drugs, often unrelated to the compound applied initially. MDR has also been observed during the pharmacotherapy of epilepsia (Aronica et al., 2003; Rizzi et al., 2002; Tishler et al., 1995), various mycosis (Kontoyiannis and Lewis, 2002; Wirsching et al., 2000), bacterial infections (Putman et al., 1999; Van Bambeke et al., 2000; Van Bambeke et al., 2003; Van Bambeke et al., 2003) and parasitosis. Under these conditions, the transporters are either activated and/or upregulated. This leeds to an efficient export of the intruding chemicals resulting in an increased detoxification (in the case of chemical hazards), but a reduced efficiency of drugs. Indeed, Pgp-like efflux transporters have been found in different pathogenic microorganisms, and in several parasitic protozoa such as *Plasmodium*, *Leishmania* and *Entamoeba*, and have been shown to contribute to the drug resistance phenotype (Howard et al., 2002; Ullman, 1995).

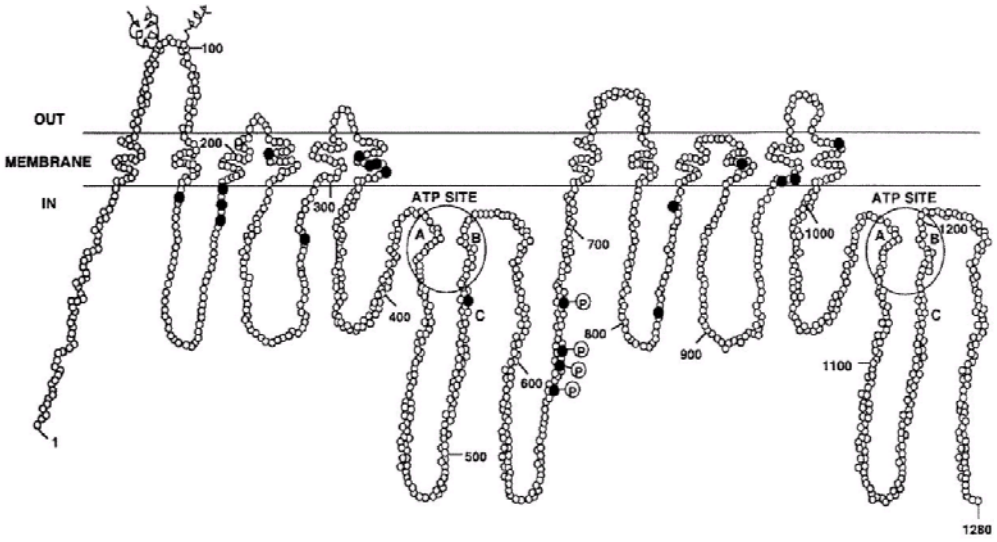


Figure I.1. *Secondary structure of human P.glycoprotein*. Two homologous halves of 6 putative TMD are connected by a flexible linker peptide. Two ATP binding sites are highlighted (circles). Phosphorylated groups and point mutations are shown (black dots). Adapted from (Ambudkar et al., 1999)

To reduce MDR there are also attempts to express Pgp mutants in sensitive tissues (bone marrow) of cancer patients, in order to target tumors with higher drug concentrations while protecting normal tissues (Gottesman, 2003; Podda et al., 1992).

Beyond its inauspicious role, mainly in cancer treatment Pgp plays an important physiological function in healthy organisms. In mammals, Pgp is expressed constitutionally in cells specialized in selective transport, e.g. the apical membrane of small intestine enterocytes (Benet et al., 1999), the endothelial cells of brain capillaries involved in the constitution of the blood-brain barrier (BBB) (Schinkel et al., 1996; Thiebaut et al., 1989), the luminal membrane of hepatocytes (Silverman and Schrenk, 1997), and generally in all tissues in which a highly selective compartmentalization is needed, such as kidney, pancreas, adrenal glands, colon, jejunum, liver, brain (Thiebaut et al., 1987). Functional expression of Pgp is also observed in the luminal surface of secretory epithelial cells of the pregnant uterus (Piekarz et al., 1993) and in the placenta (MacFarland et al., 1994).

The basic challenges in fundamental research consist in understanding how Pgp recognizes its substrates, how the ATP-driven catalytic cycle leading to drug extrusion functions, and how the molecular pathways inducing and modulating Pgp expression on the cell surface are triggered.

The apparent lack of specificity for substrates has been a veritable mystery for a long time. The only accepted homologies among Pgp substrates were their hydrophobic and amphiphilic nature (Ford and Hait, 1990; Gottesman and Pastan, 1993). However, the incompleteness of such an interpretation has been pointed out by the observation that compounds such as morphine, which is rather hydrophilic, can also be recognized by Pgp (Fischer, Gottschlich and Seelig, unpublished results). Based on the analysis of 100 compounds interacting with Pgp a recent model suggests a further common property (Seelig, 1998). According to this model, the ability of a compound to act as a Pgp substrate, inhibitor or inducer of Pgp overexpression is determined by the presence of specific intramolecular electron donor or hydrogen bond acceptor patterns. The patterns consist of two electron donor groups (or hydrogen bond acceptor) with a spatial separation of 2.5 ± 0.5 Å (called type I pattern), and three electron donor groups with a spatial separation of 4.6 ± 0.6 Å between the outer groups (called type II pattern). Recently, Ekins et al. (Ekins et al., 2002) reported three dimensional quantitative structure-activity relationship (3D-QSAR) models for various Pgp inhibitors, outlining again the requirement of multiple hydrophobic and hydrogen bond acceptor features for molecules interacting with Pgp.

It is now commonly accepted that the interaction between Pgp and its substrates takes place from the inner leaflet of the lipid membrane. For this reason, the thermodynamics and kinetics of substrate transport is determined (i) by the lipid-water partition coefficeint, depending in turn on the packing density of the membrane, $\pi$, and the cross-sectional area of the substrate molecule, $A_S$, as well as by the direct interaction of the substrate with Pgp via hydrogen bond formation within the membrane (Seelig et al., 2005).

After a compound is intercepted by Pgp, an allosteric transition, induced by the hydrolysis of one molecule of ATP is likely to take place, however, no direct structural observation exists yet. As a result, the substrate is transferred from the inner leaflet to the outer leaflet of the lipid membrane, and thus can be released extracellularly. Once the molecule is released, Pgp recovers its original conformation at the expense of a second ATP molecule (Sauna and Ambudkar, 2000).

In the absence of xenobiotics, Pgp keeps its ATPase activity, even though at a lower rate, most likely due to the transport or "flip flop" of endogenous substrates such as phospholipids. Pgp thus may play a role in keeping the asymmetry of the lipid membrane (Higgins, 1994; Romsicki and Sharom, 2001).

For the study of the catalytic cycle of Pgp e.g., vanadate trapping (Dey et al., 1997; Kerr et al., 2001; Urbatsch et al., 1995) was used. To monitor substrate transport kinetics, several techniques have been employed, e.g. the calcein-AM assay (Hollo et al., 1994; Liminga et al., 1999), inorganic phosphate release from ATP hydrolysis in inverted plasma membrane vesicles and monoclonal antibody staining (Schinkel et al., 1993).

We developed a method to monitor P-gp-substrate interactions in *living* cells and in real-time, based on microphysiometry (McConnell et al., 1992). First human uterus sarcoma cells were used (Fisher, PhD thesis; (Nervi, 2000) and later pig kidney cells and mouse embryo fibroblasts (Landwojtowicz et al., 2002) were used. The technique consists in measuring modulations of the cellular metabolism associated with the ATPase activity of Pgp, by microphysiometry (Mcconnell et al., 1992). The following chapters will focus on two aspects (Landwojtowicz et al., 2002; Nervi, 2000): (i) The coupling between Pgp ATPase activity and the extracellular release of $H^+$ and (ii) the interaction of drugs and surfactants both carrying appropriate H-bond acceptor groups with Pgp.

# Chapter 1. Pgp-substrates Interactions in *Living* Cells

## 1.1 Introduction

An efficient inhibition of multidrug resistance (MDR) represents a great hope for various pharmacological treatments. This requires a detailed understanding of the mechanisms underlying the MDR phenomenon. In the past, transmembrane ABC-transporters have been identified as main elements responsible for the appearance of MDR phenotype in almost all kinds of living organisms. Human P-glycoprotein, a 170 kDa 12 TMD ABC-transporter coded by the MDR1 gene (Chen et al., 1986), is probably the most extensively studied among them. A detailed understanding of Pgp-substrate interactions would provide useful information for the appropriate design of inhibitors and for improved drug delivery to target organisms.

We measured standard drugs known to be Pgp substrates (Landwojtowicz et al., 2002; Nervi, 2000), in order to test the microphysiometry technique and to assess the correlation with data obtained with conventional ATPase activation assays (Litman et al., 1997). In parallel, our investigation has been extended to compounds generally not or barely acknowledged as specific Pgp substrates, such as detergents (Nervi, 2000).

Already fifteen years ago, observations have been made that surfactants reveal some activity in the reversal of multidrug resistant (MDR) phenotype (Friche et al., 1990; Sehested et al., 1989; Woodcock et al., 1992), and few years later in the alteration of Pgp ATPase activity (Doige et al., 1993; Orlowski et al., 1998; Zordan-Nudo et al., 1993).

In the earliest studies, the hypothesis of a direct interaction of surfactant with Pgp was suggested (Friche et al., 1990; Loe and Sharom, 1993). However, in following studies, the inhibition of Pgp by detergents was considered to rather be the result of an indirect mechanism involving the alteration of the physical chemical properties of the cytoplasmic membrane (Batrakova et al., 2001; Bittner et al., 2002; Buckingham et al., 1996; Hugger et al., 2002; Hugger et al., 2002; Regev et al., 1999).

Despite the lack of a precise understanding of the effect of detergents on Pgp function, recent research focuses on the simultaneous application of nonionic surfactants (and similar molecules) with compounds that have proven to inhibit Pgp: novel applications of Pluronic block copolymers (= a detergent) in the treatment of drug-resistant tumors have been

reviewed by Kabanov (Kabanov et al., 2002). Also preclinical (Jagannath et al., 1999) and clinical trials (Martin-Facklam et al., 2002; Rischin et al., 1996) using these compounds for cancer treatment have already been described.

The use of *Pluronics* (poly(oxyethylene)-poly(oxypropylene) block copolymers) as a vector for drug delivery emerged in 1992, (Kabanov et al., 1992). This investigation showed that pluronic P85 was able to produce a drastic enhancement of the efficiency of cell loading with a fluorescent dye linked to Staphylococcus aureus enterotoxin B (SEB), and suggested endocytosis as possible transport mechanism.

In the following years, several reports described that combinations of pharmacological agents and polyethoxylated surfactants, or similar ester derivates, could improve the oral bioavailability of the drug and lower the multidrug resistance activity of Pgp (Banerjee et al., 2000; Cornaire et al., 2000; Dintaman and Silverman, 1999; Komarov et al., 1996) and related transporters (Miller et al., 1999). By means of flow cytometry with Caco-2 cells it was shown that nonionic detergents, such as Tween 80, reverse MDR even more efficiently than standard non-detergent Pgp-modulators, such as verapamil, trifluoperazine and reserpine (Lo et al., 1998).

Nevertheless, the mechanism of action of detergents on Pgp remained unclear, (see (Kabanov et al., 2003) for a review). Some studies suggest that MDR reversal by Pluronics and other surfactants could occur, apart from membrane fluidization, also through effects on buffer osmolarity, via direct transporter inhibition, or mitochondrial toxicity leading to an induction of energy depletion in the cell, i.e., a decrease of intracellular ATP available for Pgp (Batrakova et al., 2001; Batrakova et al., 2001; Johnson et al., 2002). Other investigations support the assumption, that membrane fluidization is not the only explanation for surfactant-induced Pgp inhibition (Rege et al., 2002). A biological explanation for the cellular uptake of polysorbate 80-coated nanoparticles (Kreuter, 2001) was recently given by Aliautdin and coworkers. They described how drugs could cross the blood-brain barrier (BBB) by endocytotic inclusions from endothelial cells of cerebral vessels, through the adsorption of apolipoproteins of the blood plasma to the particles surface and their interaction with receptors of low-density lipoproteins on endothelial cells (Aliautdin et al., 2003).

Support for a direct interaction of surfactants with Pgp was recently provided by a comparative study that showed selective Pgp versus MRP2 modulation by nonionic polyethoxylated compounds, including polysorbate 80 (Tween 80) (Bogman et al., 2003).

At concentrations below their critical micellar concentration, detergents were generally considered as biologically inactive compounds and, as such, of no or little toxicity (Lo, 2003). However, toxic effects have been reported recently, at a pharmacological as well as at the environmental level. At the pharmacological level, it has been shown that the use of surfactants in drug delivery formulations can produce toxic side effect, e.g., acute anaphylactoid hypersensitivity reactions, peripheral neuropathies (ten Tije et al., 2003; van Zuylen et al., 2001), hyperlipidaemia, abnormal lipoprotein patterns and aggregation of erythrocytes (Gelderblom et al., 2001). At the ecological level, the unceasing accumulation of surfactants, mainly originating from cleaning industry, is an inauspicious reality. Cultured fish hepatocytes P-gp-function was shown to be altered by non-ionic detergents, such as the alkylphenolic surfactant nonylphenol diethoxylate (NP2EO), suggesting that water pollutants most probably can impair the organismal defence of ichthyic fauna against xenobiotics (Sturm et al., 2001).

Very few studies approached the investigation of Pgp-surfactant interaction on a physical-chemical basis. Correlation between surfactant biological activity and their critical micellar concentration have been proposed (Miller et al., 1997; Zastre et al., 2002).

The common characteristic of surfactants interacto with Pgp, despite their more or less pronounced amphyphilic nature, is the presence of a variable number of ethoxylated groups.
The length of the ethoxylated chains was recently shown to play a role in the efficiency of the Pgp-modulatory activity of pluronics (Batrakova et al., 1999; Batrakova et al., 2003; Lo, 2003) and other polyethoxylated compounds (Sauna et al., 2004). These results were interpreted on the basis of classical physical chemical features, such as the variable hydrophobicity and the sterical properties of the compounds. It was further shown that ethoxylated surfactants, which are commonly used detergents in industry and home care products, interact with human Pgp, whereas alkylphenols, which are toxic environmental polluants derived from anaerobic biodegradation of alkylphenol ethoxylates, did not show any effect on Pgp activity (Loo and Clarke, 1998).

The aims of the present work were i) to establish the microphysiometer technique for the study of standard Pgp substrates, ii) to correlate the measured extracellular acidification rate *in vivo* with previous measurements of Pgp ATPase activity in reconstituted systems, and iii) to investigate Pgp activation by surfactants and to then correlate activation with the ability of surfactants to act as H-bond donors.

## 1.2 Theory

### The Cytosensor® Microphysiometer System: Biological Foundations

Chemo-organo-heterotrophic systems (definition: require organic substrates to get their carbon for growth and development), such as mammals, utilize sugars, amino acids and fatty acids as primary carbon sources for metabolic energy. Under natural aerobic conditions, energy is extracted from glucose and stored in the form of ATP via the cytosolic *Embden-Meyerhof* pathway coupled with the mitochondrial TCA cycle and oxidative phosphorylation. Hypoxic conditions, such as commonly present in *in vitro* cell cultures (Mandel, 1986), as well as tumoural features (Warburg, 1926), have been shown to induce a switch in the cell metabolism of pyruvate from the oxidative phosphorylation toward lactic fermentation (Gebhardt et al., 1978). The yield of the latter reaction is 19 times lower in terms of ATP production per glucose molecule (2 ATP/glucose versus 38 ATP/glucose). The rate of acid production of the fermentative pathways is much more pronounced than aerobic respiration, with a yield of 1 $H^+$/ATP compared to 0.167 $H^+$/ATP, respectively.

Mammalian cells in culture can also obtain 30 to 100% of their metabolic energy from glutamine oxidation (Zielke et al., 1984), which leads to an energy yield of 29 ATP/glutamine and a proton production of 0.111 $H^+$/ATP (Owicki and Parce, 1992).

In previous studies it has been estimated that adherent mammalian cells in culture can produce ~ 1 $\cdot 10^8$ $H^+s^{-1}cell^{-1}$ (Parce et al., 1989), corresponding to at least $10^8$ $ATPs^{-1}cell^{-1}$ (Owicki et al., 1990).

The extrusion of acidic metabolites from the cell is performed passively or through several facilitated mechanisms. Some lactic acid and $CO_2$ can exploit the permeability of the lipid membrane and be evacuated by passive diffusion. Lactic acid is also excreted by means of the monocarboxilic acid transporter. Bicarbonate can cross the cytoplasmic membrane through several anion transporters, e.g. the chloride-bicarbonate antiporter. Protons are transported via several $H^+$-channels and pumps, such as the $Na^+/H^+$-ATPase (Fischer et al., 1999).

External stimulation, e.g. exposure to a toxic agent or the activation of a receptor, can induce physiological alterations in the cell, such as changes in the ionic equilibrium or the metabolic

activity. As a consequence, the cellular ATP consumption changes. Since ATP hydrolysis is coupled with the production of acidic metabolites, a variation of the extracellular acidification rate (ECAR) results in parallel. The Cytosensor® Microphysiometer allows a precise detection of the latter parameter.

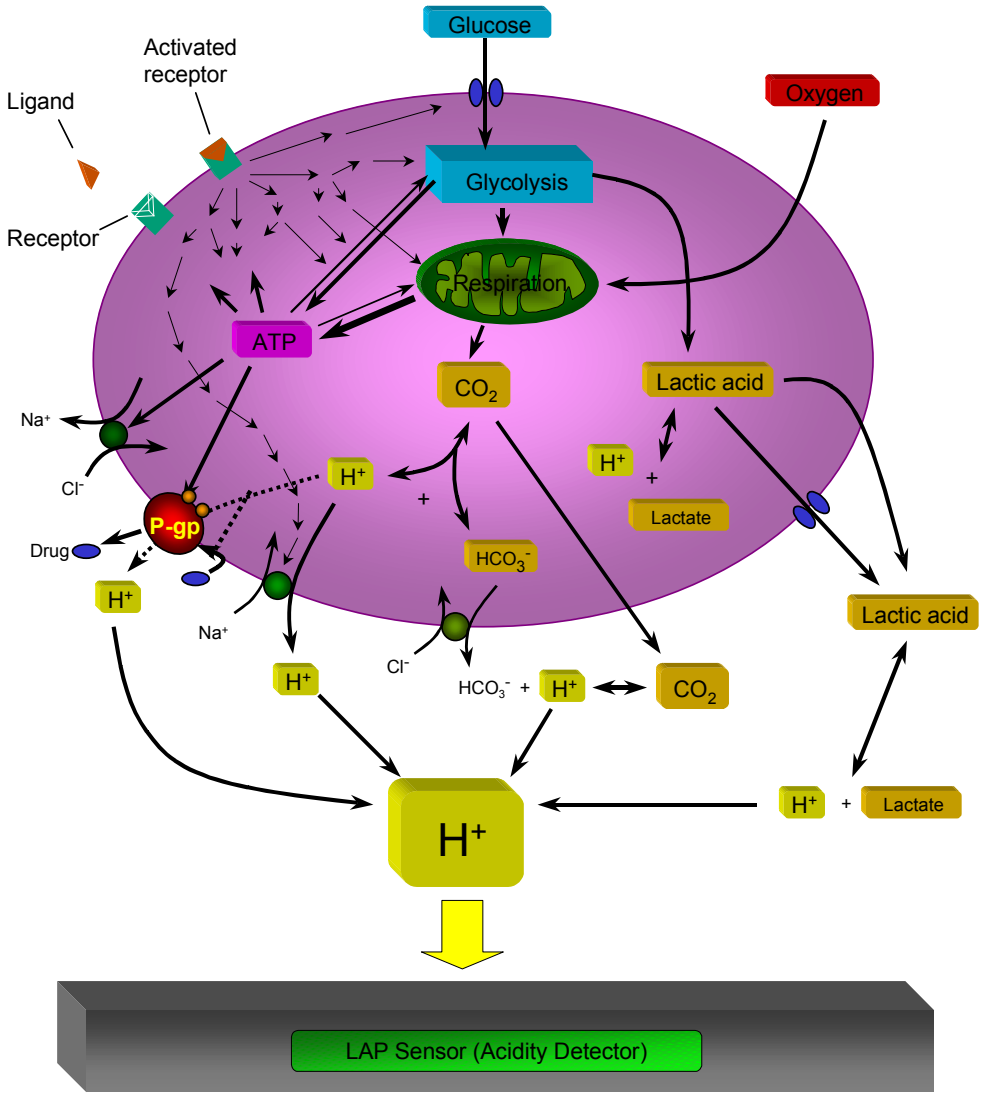


Figure 1.1. *Schematic representation of cellular metabolism and its relationships to physiological processes such as receptor activation.* The principal features of cellular proton economy are shown. Not all the indicated pathways are necessarily used by all cells. The putative contribution of P-glycoprotein (P-gp) is shown.

## The Cytosensor® Microphysiometer System: Physical Basis

The Cytosensor® Microphysiometer System is essentially a very sensitive pH-meter connected with a thermoregulation and a network of peristaltic pumps. Its core is composed by a so called "sensor chamber", which consists of a teflon container with a silicon chip on the bottom. The physical principle of the sensor is similar to that of an ISFET ("Ion Sensitive Field Effect Transistor"). *Living* cells, which continuously produce acidic metabolites from their metabolic activity (see previous section) act as proton source, S.

The surface of the chip exposed to the aqueous environment is covered by a $SiO_2$ insulator layer, as for normal MOS-FET ("Metal Oxide Semiconductor-Field Effect Transistor"). The Si plate is much thicker (order of mm) than a normal industrial transistor (order of μm) and is formed by a pure single-crystal (commercial transistors are contaminated with metals from the chemical periodic system III or V group). To induce an electrical flow, IR-light is used instead of metal contaminations. Indeed, the single-crystal of Si has a very specific absorbance of Electromagnetic (EM) radiation with a wavelength $\lambda$ = 900 nm and, when excited by an amplitude-modulated light-emitting diode (LED), it becomes a conductor. As a consequence of these features, the sensor is called light-adressable potentiometric sensor (LAPS).

An external electronic circuit (connection between ohmic contact and aqueous compartment) controls the potential, $\psi$, applied from the Si to the aqueous solution and measures an alternating photocurrent, $I_p$. Such a photocurrent is alternate current (ac)-coupled and is generated when the LED illuminates the underside of the Si chip.

The potential from the Si to the solution can be adjusted so that the sensor can become (i) forward biased or (ii) reverse biased. In the first case no photocurrent is produced, while in the second a depletion layer, resulting in a potential gradient, is created under the insulator. At the atomic level, this corresponds to a hole-electron pair creation upon radiation absorption from the LED. Because an electric field is present in the chip, holes and electrons move in opposite directions, producing the local current. This situation is similar to a p-/n-channel in transistors. No direct current passes through the insulator.

The applied potential, ψ, at which the photocurrent begins to flow is defined as the sum of several contact potentials of the hardware (which are constant) and the surface potential of the solution-insulator interface. A determination of the changes in ψ required to produce the photocurrent permits thus to measure the variations of the surface potential.

The insulator surface is partially covered by silanol groups (SiOH) and few amino functions ($SiNH_2$), both of which can be titrated as a function of pH. The surface is neutral at pH ~ 3.5. Consequently, at physiological pH the surface becomes negatively charged. This feature makes the surface potential pH-dependent. Such a dependence is Nernstian (= the plot of the potential difference vs. the logarithm of the ionic activity is linear with a slope of 2.303 RT/zAF, e.g. 59.16/zA mV per unit change of $p_aH$ at 298.15 K).) and linear from pH 2 to 11 (Hafeman et al., 1988).

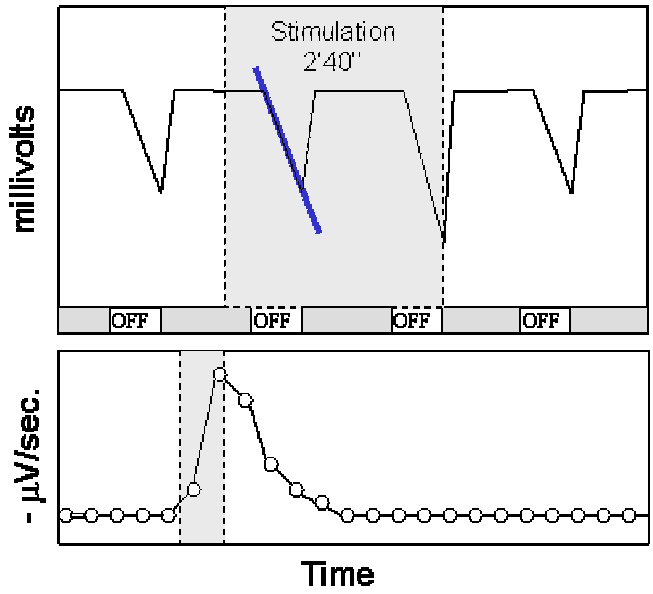


Figure 1.2. *Raw data and Rate data from Cytosensor™ Microphysiometer measurements*. In the upper scheme, the applied voltade ($V_{PIP}$, mV) is plotted versus time. During cyclic pump-off periods (OFF), the ECAR is calculated from the derivative of the photocurrent drop recirded in raw data (blue line) and plotted as a function of time ($-\mu V \cdot s^{-1}$).

The raw data and rate data recorded during the experiments are based on variations of the photocurrent (see Figure 1.2). The system sweeps the applied voltage every second, producing a curve of photoresponse ($I_p$) versus the applied voltage ($V_p$). The inflection point (IP) of the curve is characterized by particular $I_{PIP}$ [µA] and $V_{PIP}$ [mV]. In raw data $V_{PIP}$ is plotted versus time. When the pumps are off, the extracellular acidification causes a weakening of the

surface potential. The corresponding electric field also diminishes and the photocurrent drops. At 37 °C, the $V_{PIP}$ shift corresponds to about 61 mV per pH unit. The derivative of the slope generated in the raw data, during the ECAR -dependent photocurrent drops, is calculated and plotted versus time to illustrate the rate data [$-\mu V \cdot s^{-1}$].

## Surface Activity and the Gibbs Adsorption Isotherm

When an amphyphilic compound is injected into an aqueous solution, a distortion of the surrounding water cluster occurs, leading to a decrease of the entropy of the system. To reach a more stable energetic state, the amphyphilic molecules tend to be extruded from the bulk phase and accumulate at the air-water interface. Such an entropy-driven process is called the *Hydrophobic Effect*. The presence of surfactant molecules at the air-water interface, can be observed macroscopically as a lowering of the interfacial tension of the aqueous solution, defined as

$$\gamma_0 - \gamma = \pi , \qquad (1)$$

where $\gamma_0$ is the surface tension of pure water (~ 72 mN/m at 20 °C), $\gamma$ is the surface tension of the surfactant containing solution, and $\pi$ is the surface pressure. The latter can be determined experimentally with the Wilhelmy vertical plate method (see material and methods).

The thermodynamics of the adsorption of a surfactant to an air-water interface can be described by the *Gibbs adsorption isotherm*. According to Gibbs, the change in the interfacial tension of the solvent can be described as

$$-d\gamma = \sum \Gamma_i \, d\mu_i \ , \qquad (2)$$

where $\mu_i$ and $\Gamma_i$ are the chemical potential and the surface excess concentration of any component of the system, respectively.

At equilibrium between the interfacial and bulk phase, the change of the chemical potential of any component of the system, $d\mu_i$, can be expressed as

$$d\mu_i = RTd \ln a_i , \qquad (3)$$

where $a_i$ is the activity (mole fraction · activity coefficient) of any component of the system, and $RT$ the thermal energy. For solution concentrations < $10^{-2}$ M containing only one non dissociating surfactant, the activity of the solvent and the activity coefficient of the solute can be considered as constant and the mole fraction of the solute can be replaced by its molar concentration, $C_S$ (Rosen, 1989) . Equation (1) can thus be written as

$$d\gamma = -RT\Gamma_S \, d\ln C_S = -d\pi \tag{4}$$

which corresponds to the commonly used form of the Gibbs equation, for aqueous solutions of nonionic surfactants.

The surface excess concentration, $\Gamma_S$, is defined as the excess, per unit area of interface, of the amount of any component actually present in the system over that present in a reference system of the same volume in which the bulk concentrations in the two phases remain uniform up to a hypothetical (Gibbs) dividing surface (Rosen, 1989):

$$\Gamma_S = \frac{\Delta n}{A} = \left(N_A \cdot A_S\right)^{-1} \tag{5}$$

where $A_s$ is the area per molecule required at the interface. In the absence of electrostatic interactions $A_S$ is identical with the cross-sectional area, $A_d$, if the limiting value, $\Gamma\infty$, defined as

$$\Gamma_\infty = \frac{d\pi}{RTd\ln C_S} \tag{6}$$

is reached. Under these conditions the surface pressure, π, increases linearly with the logarithm of concentration, $C_s$. The cross-sectional area of the surfactant molecule can thus be directly calculated from equations (5) and (6), and the plot of $\pi$ versus ln$C_S$ which yields a straight line.

The surface excess concentration, Γ, can also be expressed according to the *Langmuir adsorption isotherm*, by the following equation:

$$\Gamma = \Gamma_\infty \frac{K_{aw} C_{S_{aq}}}{1 + K_{aw} C_{S_{aq}}} \tag{7}$$

where $K_{aw}$ is the air-water partition coefficient. The combination of an integral form of equation (6) with equation (7), gives rise to the Szyszkowsky equation, which relates the

change in the surface tension, dγ, (or surface pressure, π) with the air-water partition coefficient, $K_{aw}$, as

$$\pi = RT\Gamma_{\infty} \ln\left(1 + K_{aw} C_S\right) \quad (8)$$

Monolayer experiments determine directly the lowering of the surface tension, γ, or the increase in surface pressure, π, as a function of the concentration of the surface active compound injected into the aqueous solution. From the fit of the π/logC plot, $K_{aw}$ can be obtained.

The air-water interface can be regarded as model system for the membrane-water interface system due to (i) the similarity of dielectric constant of air ($\varepsilon_{air} \sim 1$) with that of the interior of a lipid membrane ($\varepsilon_{lipid} \sim 2$), (where the dielectric constant of water is $\varepsilon_{water} \sim 80$) and (ii) its ability to orientate amphiphilic molecules in an anisotropic manner. From these points of view, the air-water interface represents a much better model for lipid membranes, than organic solvents, which are isotropic and have higher dielectric constants.

The penetration of a compound into a lipid bilayer requires work which is proportional to the lateral packing density of the lipid bilayer, $\pi_{bi} \sim 32\text{-}34$ mM $\cdot m^{-1}$ (Fischer et al., 1998; Seelig, 1987), and the cross-sectional area of the inserting molecule:

$$\Delta W = \pi_{bi} \cdot A_S \quad (9)$$

The lipid-water partition coefficient has to take into account those impeding factors and can thus be expressed as

$$K_{lw} = K_0 e^{\left(\frac{-A_S \pi_{bi}}{k_B T}\right)} \quad (10)$$

where $K_0$ corresponds approximately to the air-water partition coefficient, $K_{aw}$, if the surface pressure of a surfactant concentration $C_S = K_{aw}^{-1}$ is negligibly small.

## Type I/II Units

According to a model developed by Seelig (Seelig, 1998), compounds can be recognized by Pgp through H-bond acceptor (or electron donor) groups (e.g. carbonyl-, ether-, hydroxy-,

tertiary amino groups, π-electrons systems, and certain halides),arranged in specific special recognition patterns. Such recognition patterns consist of (i) two electron donor groups at a distance of 2.5 ± 0.5 Å, (ii) two electron donor groups with a spatial separation of 4.6 ± 0.6 Å or (iii) three electron donor groups with the two outer groups separated by 4.6 ± 0.6 Å, defined as Type I Units (i) and Type II Units (ii and iii). A graphical representation of hydrogen bond acceptor patterns is shown in Figure 1.3.

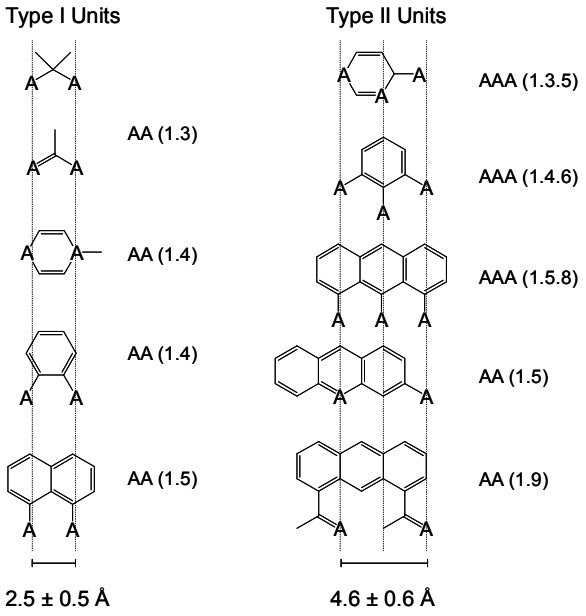


Figure 1.3. *Type I and II Units*. Type I: two electron donor groups distributed at a distance of 2.5 ± 0.5 Å. Type II: two electron donor groups with a spatial separation of 4.6 ± 0.6 Å or three electron donor groups with the two outer groups separated by 4.6 ± 0.6 Å (Seelig, 1998).

## Hydrogen Bond Acceptor Strength

For simplicity hydrogen bond acceptors were divided into two groups: strong ones ("A", e.g., >C=O, -OR, contributing one energy unit, EU, corresponding to maximally 20 kJ/mole) or weak ones ("a", e.g., $-NR_3$, -N=, -RX, -SR, $-C_6H_5$, contributing ½ EU). "AA", "Aa" or "aa" Type I Units correspond thus to 2, 1.5 or 1 EU, respectively.The number of EU of a molecule determines the strength of its binding to the H-bond donor side chains of the TM α-helices of Pgp, which most probably represent the binding sites of the transporter (Seelig et al., 2000).

## 1.3 Material and Methods

### Compounds

The nonionic surfactants n-ethyleneglycol monododecylether ($C12EO_{n=3}$, $C12EO_{n=8}$), Triton X-100, polysorbate-80 (Tween 80), and the zwitterionic detergent Chaps (3-[(cholamidopropyl)dimethylammonio]-propanesulfonate), were purchased from Fluka (Buchs, Switzerland). Amiloride, chlorpromazine, colchicine, trifluoperazine, (R/S) verapamil, and vinblastine were from Sigma (Steinheim, Germany), and calcein acetoxymethyl ester (calcein-AM) from Molecular Probes (Leiden, The Netherlands). Amitriptyline and cyclosporin A were gifts from Merck (Darmstadt, Germany) and Novartis (Switzerland), respectively. For stock solutions, compounds were dissolved in water, except for cyclosporin A, vinblastine, calcein-AM and C12EO3, which were dissolved in DMSO. Final solutions were prepared in DMEM, and actual solvent concentrations were ≤ 0.5%. [u-$^{13}C_6$]-D-glucose was purchased from Cambridge Isotope Laboratories, Inc. (Andover, MA,USA). The P-glycoprotein-specific antibody MRK16 was a gift from Dr. M.M. Gottesman (National Cancer Institute, Bethesda, U.S.A.). Purified mouse standard isotype $IgG_{2a,k}$ and FITC-labeled anti mouse $IgG_{2a}$ were from Pharmingen (San Diego, U.S.A.). Cell culture media and additional compounds required for cell culture were from Gibco-BRL (Basel, Switzerland).

### Cell Lines

Mouse embryo fibroblasts, both wild type (NIH3T3) and transfected with the human MDR1 gene (NIH-MDR-G185) (Cardarelli et al., 1995), were a kind gift from Dr. M.M. Gottesman (National Cancer Institute, Bethesda, U.S.A.). Pig kidney cells LLC-PK1 and MDR-LLC, were provided by Dr. P.Borst (The Netherlands Cancer Institute).

## Cell Culture

Cells were grown as monolayer cultures in sterile cell culture flasks (Costar, 25-75 $cm^2$), and incubated at 37 °C in a Heraeus Incubator, in an air atmosphere supplemented with 5 % $CO_2$ and humidity saturation of 100%. DMEM was chosen as cell culture medium, supplemented with 1% L-glutamine (0.3 g/L), 1% penstrep (100 units/mL) and 10% FBS (v/v). NIH-MDR-G185 cells were kept under growth selection with 0.15 μM (60 ng/mL) colchicine. 1:10 passages were performed twice a week, from confluent cultures, after treatment with trypsin-EDTA (Gibco). Cellular stocks aliquots of $10^7$ cells/ mL were prepared in DMEM, 10% DMSO, 10% FBS and kept in 1.8 mL *Nunc CryoTubes* frozen in liquid nitrogen. Detailed protocols for cell handling are reported elsewhere (Nervi, 2000).

## Cell Doubling Time Determination

Exponentially growing NIH3T3 and NIH-MDR-G185 cells were seeded into 30 mm dishes (2 for each cell line and for each day), in amounts of $10^4$ cells/2.5 mL DMEM/dish. Every 24 hours, the number of cells was determined by averaging the amount of cells counted in two dishes for each cell line, after trypsinization with 0.5 mL trypsin-EDTA solution, using a cell Coulter counter. The latter procedure was repeated for 8-10 days, until a plateau (confluence) was reached.

## Cell extraction

Approximately $10^8$ living mouse embryo fibroblasts (NIH-MDR-G185) were grown for 12 h in DMEM medium containing [u-$^{13}$C] glucose (5 mM) and then removed from the tissue culture dishes by using trypsin-EDTA, as described above. The cells were rinsed twice with PBS and immersed in 5 mL of 6% perchloric acid to precipitate/inactivate all proteins including enzymes that could have metabolized the compounds even after cell lysis. Subsequently, the cells were lyzed by subjecting them for 15 min on an ultrasonic bath (Branson Sonifier, Danbury, CT; 50 W/mL) under a nitrogen atmosphere (at 4°C). Then, the precipitated proteins were removed by centrifugation (Eppendorf, 14000 g) and the supernatant, containing the water-soluble metabolites was neutralized with 4% KOH. KOH in combination with $HClO_4$ was chosen as base-acid system because the solubility for $KClO_4$ is much smaller than any other salt from acid base neutralization, which is important for later residual salt contents in NMR (line broadening). The precipitate of $KClO_4$ was removed by

centrifugation (16000 g) and the supernatant was lyophilized overnight. The lyophilized metabolites were resolved in 0.5 mL of 99.9 % $D_2O$ for further analysis by high-resolution $^{13}C$- and $^{1}H$-NMR spectroscopy. The pH of the solution was adjusted to 7.4 (uncorrected pH reading for deuterated water) using deuterated perchloric acid and potassium deuteroxide (KOD). Five µL of a 0.5 M solution of [2,2,3,3-D4]-3-(trimethylsilyl)-propionic acid sodium salt (TSP) was added to provide an internal concentration standard and chemical shift reference.

## In vitro high-resolution $^{13}C$ and $^{1}H$ NMR spectroscopy

*In vitro* high-resolution $^{13}C$-NMR spectra (at 9.4 Tesla, 100 MHz) of cell extracts were obtained on a Bruker Avance 400 NMR spectrometer using the following settings: 50,000 scans, 45° pulses, 250 ppm spectral width, $^{1}H$ broadband decoupling and a repetition time of 3 s. *In vitro* high-resolution $^{1}H$-NMR spectra were acquired at 400 MHz using the following settings: 64 scans, 90° pulses, 12 ppm spectral width and a longer repetition time of 20 s to avoid saturation of the proton signals.

## Detection of P-gp Expression

The cellular expression level of P-gp was estimated by FACs analysis. Aliquots of $2\text{-}3\cdot10^5$ cells were incubated in IMEM containing 5% FBS at 37 °C for 30 min in the presence of the human Pgp-specific monoclonal antibody MRK16 or the mouse standard isotype antibody $IgG_{2a,k}$. After washing, cells were reincubated at 37 °C for 30 min in the dark, in the presence of FITC-labeled anti mouse $IgG_{2a}$. Cells were then washed (IMDM), centrifuged (1000 rpm, 5 min) and resuspended in PBS (supplemented with 1% BSA) and FACs analysis was performed using a FACscalibur flow cytometer (BD Biosciences).

## ATPase Assay

Reagents:

1) *$P_i$ reagent*.1% ammonium molybdate (or molybdic acid, ammonium salt) in 2.5 N sulfuric acid and 0.014% antimony potassium tartrate. Then 50 mL distilled water and 6.9 ml concentrated sulfuric acid (36.2 N) were added in a 250 ml beaker. To the mixture, 1 g ammonium molybdate (powder) and 14 mg of antimony potassium

tartrate were added and stirred for 20 min in a hood. Distilled water was then added to reach a total final volume of 100 ml. The final solution was stored at room temperature, in a glass bottle covered with aluminum.

2) *100 mM MES-Tris, pH 6.8*. 100 mM MES solution (1.95 g/100 mL). PH adjusted to 6.8 with Tris solution (2M).
3) *2x Assay buffer* (5 mL). 4.12 mL 100 mM MES-Tris (pH 6.8); 0.5 mL of KCl (1 M); 0.2 mL sodium azide (0.25 M), 0.16 mL EGTA (0.125 M, pH 7.0); 7.5 mg ouabain powder; 20 µL DTT (1M). Before use, 50 µL $MgCl_2$ (2 M) was added per 5mL buffer.
4) 5% SDS solution
5) 1% ascorbic acid (100 mg/10 mL water; freshly prepared and stored on ice)
6) 10 mM sodium ortho-vanadate: 9.2 mg/5 mL water. Freshly prepared solution incubated at 100 °C for three min (calibration: OD=3.6 at λ=268 nm corresponds to 1 mM).
7) 100 mM ATP (disodium salt, pH 7.0, stored at –80 °C).
8) 1mM potassium phosphate (stored at –20 °C)
9) several Pgp substrates dissolved in DMSO or water.

For the ATPase assay, all reactions were performed in 15 mL glass tubes immersed in a water bath at 37 °C. In one tube, 50 µL buffer, 31 µL $H_2O$, 3 µL vanadate (10 mM) or water, and 10 µL membrane extracts (~ 1 mg membrane/mL; ~ 20 ng proteins) were mixed and incubated for 5 min. After addition of 1 µL Pgp substrate or an equivalent amount of solvent, the solution was again incubated for 3 min. In a third step, 5 µL ATP (100 mM, pH 7.0) was added. The final solution was incubated for 20 min, during which ATP hydrolysis occured. To stop the reaction, tubes were rapidly removed from the bath, 100 µL SDS (5%) were added and the tubes were quickly vortexed. After addition of 400 µL $P_i$ reagent, 500 µL $H_2O$ and 200 µL ascorbic acid (1%), the system was incubated for 10 min at room temperature. Finally, optical density was measured at λ=880 nm. Inorganic $P_i$ concentrations were calculated from the absorbance values, according to a standard phosphate curve (multiplication of absorbance by a factor ~ 61). The turnover of ATP hydrolysis was then obtained in nmoles $P_i \cdot min^{-1} \cdot (mg\ protein)^{-1}$, by normalizing the $P_i$ concentration obtained (multiplication by a factor 5).

One complete assay for one substrate concentration, required 10 glass tubes, i.e., A) two negative controls (no vanadate, no membrane extract, no drug), B) two controls for basal endogenous ATPase activity (only membrane extract), C) two controls for the inhibition of

endogenous ATPase activity (vanadate, membrane, no drug), D) two assay for drug induced ATPase activity (no vanadate, membrane extracts, active compound) and E) two controls for inhibition of drug-induced ATP hydrolysis (vanadate, membrane and active compound). Where no drug was added, the same volume of solvent alone (1 µL DMSO or water) was injected in test tubes. For the determination of the drug-induced Pgp activation (fold), data obtained from the difference between D) and E) were divided by the difference between B) and C).

## Cytosensor Measurements

Extracellular acidification rates (ECAR) of cells were monitored in real time using a four or eight channels Cytosensor® Microphysiometer (Molecular Devices, Menlo Park, CA, U.S.A.) (Mcconnell et al., 1992). This device is based on silicon technology and allows detection of pH changes down to 0.001 pH units/min by means of a light addressable potentiometric sensor (LAPS). Protons excreted by cells upon stimulation come into contact with the LAPS and induce a change in the applied voltage in the order of a few µVolts/sec. The instrument was calibrated at 37 °C, and a correspondence of 1 pH unit = 60.37 ± 1.28 mV was measured.

Aliquots of 3-4 $\cdot 10^5$ cells were seeded into capsule cups (12 mm diameter plates with a microporous polycarbonate membrane bottom) and were left in the incubator overnight for sedimentation in the presence of the same medium used for culture (see above). For the cytosensor measurement, capsule cups were transferred into the sensor chambers, adequately covered with capsule spacers and inserts, in order to create a void volume of 6 mm diameter and 50 µm height. Thus, the actual number of cells available for the measurement is reduced to ~1/4 of the total amount. The system was stabilized at 37 °C and cells were superfused by peristaltic pumps with ~ 100 µL/min DMEM without sodium bicarbonate, to limit pH buffering.

Peristaltic pumps were programmed to function for 1 min 40 sec, and then to stop for a period of 20 sec, in a periodic cycle. During the 20 sec pause interval, acidic metabolites accumulated in the sensor chamber. ECAR measurements, in µV/sec, started 5 sec after pump stop and lasted for 13 sec. All data were directly processed by the software Cytosoft for Macintosh (Molecular Devices, Menlo Park, CA, U.S.A.). Before P-gp stimulations, cells

were allowed to reach a stable ECAR (30 min to 1 hour). For stimulations, the normal running medium was switched to the drug containing medium for 2 min 40 sec. During this period, two ECAR data points were recorded, one after 40 sec (transient situation) and the second two minutes later (steady-state conditions established). For data analysis, the cellular ECAR change corresponding to the latter point was considered, normalized to the basal activity, and therefore expressed in percentage (or fold) of the basal ECAR.

Cytosensor microphysiometry detects pH changes as a function of time in the sensor chamber solution. For a quantification of $H^+$ release rate the measured ECAR was corrected for the buffering capacity of the superfusing medium. To this purpose, the phosphate buffer of DMEM was taken into account, and the buffer capacity was calculated as $\beta = 0.35$ mM for 1mM buffer at pH 7.40. The buffer capacity of other medium components, such as amino acids, was neglected. The calculated $\beta$ corresponds thus to the lower buffering limit.

## Kinetic Model.

The drug concentration dependent ECAR modulations were fitted with a modified Michaelis-Menten equation, described in detail by Litman et al. (Litman et al., 1997; Litman et al., 1997). The model assumes a transporter activation, if one substrate molecule (S) per transporter (T) binds, and it assumes inhibition after a second substrate molecule per transporter binds as described by the following scheme:

$$\begin{array}{l} S_{aq} \underset{k_{-0}}{\overset{k_0}{\rightleftharpoons}} S_1 + T + ATP \underset{k_{-1}}{\overset{k_1}{\rightleftharpoons}} T(ATP)S_t + S_1 \underset{k_{-2}}{\overset{k_2}{\rightleftharpoons}} T(ATP)S_{t_2} \xrightarrow{k''} T(ADP) + P_i + 2\,S_{rel} + H^+ \\ \qquad\qquad\qquad\qquad\qquad\qquad\qquad\qquad\qquad\qquad \downarrow k' \\ \qquad\qquad\qquad\qquad\qquad\qquad\qquad\qquad\qquad\qquad T(ADP) + P_i + S_{rel} + H^+ \end{array} \qquad (1)$$

where $T(ATP)S_t$ and $T(ATP)S_{t2}$ are Pgp-ATP complexes with one and two substrate molecules bound, respectively. $T(ADP)$ is the Pgp-ADP complex, $P_i$ is the inorganic phosphate released into the cytosol, and $S_{rel}$ is the substrate molecule released extracellularly.

As reported in scheme (1), the kinetic parameters describing the ATPase hydrolysis during the substrate transport by Pgp can be obtained either from the quantification of $P_i$ release or from the quantification of $H^+$ release according to equation (2):

$$V_{S_{aq}} = \frac{K_1 K_2 V_0 + K_2 V_1 C_{S_{aq}} + V_2 C_{S_{aq}}^2}{K_1 K_2 + K_2 C_{S_{aq}} + C_{S_{aq}}^2} \quad (2)$$

where $V_{Saq}$ is the ECAR as a function of the substrate concentration in solution, $C_{Saq}$, $V_0$ is the basal activity in the absence of substrate, $V_1$ is the maximum transporter activity (if only activation occurred), and $V_2$ is the activity at infinite substrate concentration.

## Surface activity measurements

Surface activity measurements of surfactants were performed at room temperature, with the *Wilhelmy* vertical plate method, as described in detail elsewhere (Nervi, 2000; Seelig et al., 1994). Stock solutions were prepared in pure water and serial aliquots were injected by means of *Hamilton* syringes into a home built 20 ml or 3 ml teflon trough filled with 10 mM Tris/HCl buffer (pH 7.40) and 114 mM NaCl.

## Estimation of Hydrogen Bond Energy

The models of the three-dimensional structures of the compounds as well as the spatial distances between hydrogen bond acceptor groups in Pgp recognition patterns were obtained using a modified version of the Allinger's MM2 force field approach (Burkert and Allinger, 1982) implemented in the software ChemOffice (CambridgeSoft Corporation, Cambridge, MA, U.S.A.). The hydrogen bond acceptor strength of the compounds was estimated in arbitrary energy units (EU), according to the model described in section 3.2 (Seelig, 1998).

## 1.4 Results

### Cell growth characterization

In order to investigate the behavior of mouse embryo fibroblasts under the culture conditions chosen, the growth rate of cells has been followed during 8 days. From the exponential growth phase, the doubling time has been calculated for NIH3T3 and NIH-MDR-G185. The latter were grown in DMEM (1% Penstrep, 1% L-glutamine, 10% FBS) or in the presence of DMEM and the selecting agent colchicine (60 ng/mL), to take into account potential alterations in the cell cycle under selection pressure.

Results are reported in Figure 1.4.

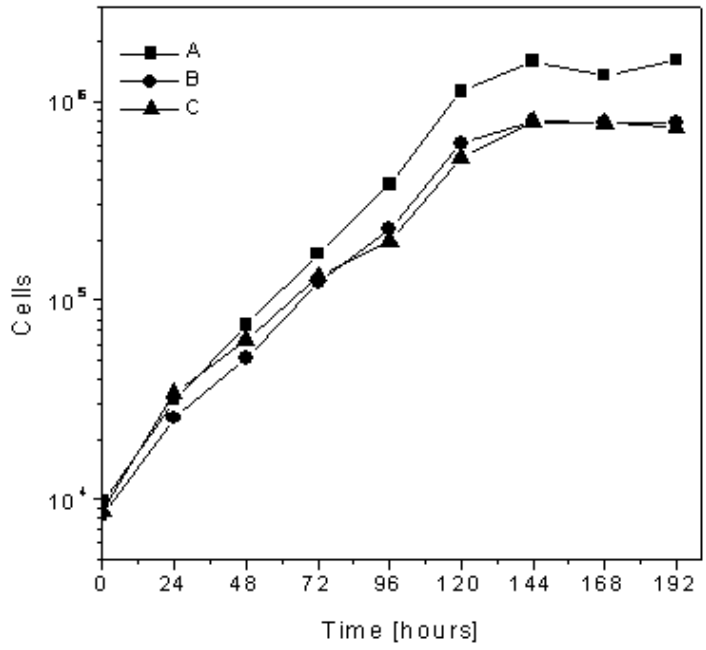


Figure 1.4. *Cellular Growth Curve*. The number of cells grown in culture is plotted against time. (A) NIH3T3 cells, (B) NIH-MDR-G185 cells grown in DMEM, (C) NIH-MDR-G185 cells grown in DMEM supplemented with 60 ng/ml colchicine.

From an exponential growth fit of the plots, the population doubling rate was determined as 22.7 ± 1.2 hours for NIH3T3, 25.2 ± 2.1 hours for NIH-MDR-G185 grown in DMEM and 27.2 ± 4.3 hours for NIH-MDR-G185 cells grown in the presence of colchicine.

The growth curves show that transfected cells (~ $1.10 \cdot 10^5$ NIH-MDR-G185/$cm^2$) become confluent at a lower density than wild type cells (~ $2.15 \cdot 10^5$ NIH3T3/ $cm^2$) and that colchicine does practically not affect cell growth.

## Assessment of the Expression Level of P-glycoprotein on the Cell Surface

To assess the expression of Pgp in the plasmamembrane of MDR1 transfected cells, an immunocytochemical assay was performed using the human Pgp specific antibody MRK16. After appropriate antibody staining (see section 1.3) NIH-3T3 and NIH-MDR-G185 mouse fibroblasts were analyzed by FACS. For comparison, the same essay was applied to pig kidney LLC-PK1 and LLC-MDR cells (Landwojtowicz et al., 2002).

Figure 1.5 shows that the relative fluorescence intensity of wild type mouse embryo fibroblasts NIH3T3 (A) is negligibly small in comparison to that of Pgp expressing NIH-MDR-G185 cells (B, blue line) and that the fluorescence resulting from NIH3T3 staining with MRK16 (blue) does not differ from the unspecific binding with the control antibody (green) or the FITC-labeled anti-mouse $IgG_{2ak}$ (black). The slightly shifted position of the stained cell populations, from the endogenous fluorescence of untreated cells (red), is a normal effect resulting from unspecific binding. Possible differences in the integrals of curves are a consequence of the choice of the region of interest in the dot plot obtained from the cytometric assay (plot not shown), which can include a variable number of events for different samples. Transfected fibroblasts NIH-MDR-G185 (Figure 1.5B), however, showed a relative fluorescence intensity three orders of magnitude higher than that of the corresponding untreated or Pgp unspecifically stained cell populations. Distribution curves in Figure 1.5B) did not show any overlapping region, indicating that almost all NIH- MDR-G185 cells were stably transfected and thus expressing a high level of human Pgp.

The situation of wild type pig kidney LLC-PK1 cells (Figure 1.5C) is similar to that of NIH3T3. Despite a generally broader Gaussian distribution of the fluorescence, no significant distinction could be made between MRK16-stained cells (blue) and unspecific binding controls (green and black). However, in analogy to NIH-MDR-G185 cells, MRK16 labeling of transfected pig kidney LLC-MDR-PK1 cells (Figure 1.5D, blue and magenta lines) revealed a relative fluorescence intensity of almost three orders of magnitude higher than observed in control populations (green, black and red). Interestingly, the fluorescence distribution of LLC-MDR-PK1 cells grown in DMEM without the presence of vinblastine as

selecting agent (Figure 1.5D) blue line) shows two distinct peaks at relative fluorescence intensities of ~ $10^1$ and ~ $10^3$, respectively. This corresponds to two distinct cell populations: the peak with fluorescence intensity ~ $10^1$ shows that 30-40% of cells were not transfected (or had lost the MDR1 gene). Indeed, in MRK16-stained LLC-MDR-PK1 cells, grown in the presence of selective agent, the lower peak disappeared.

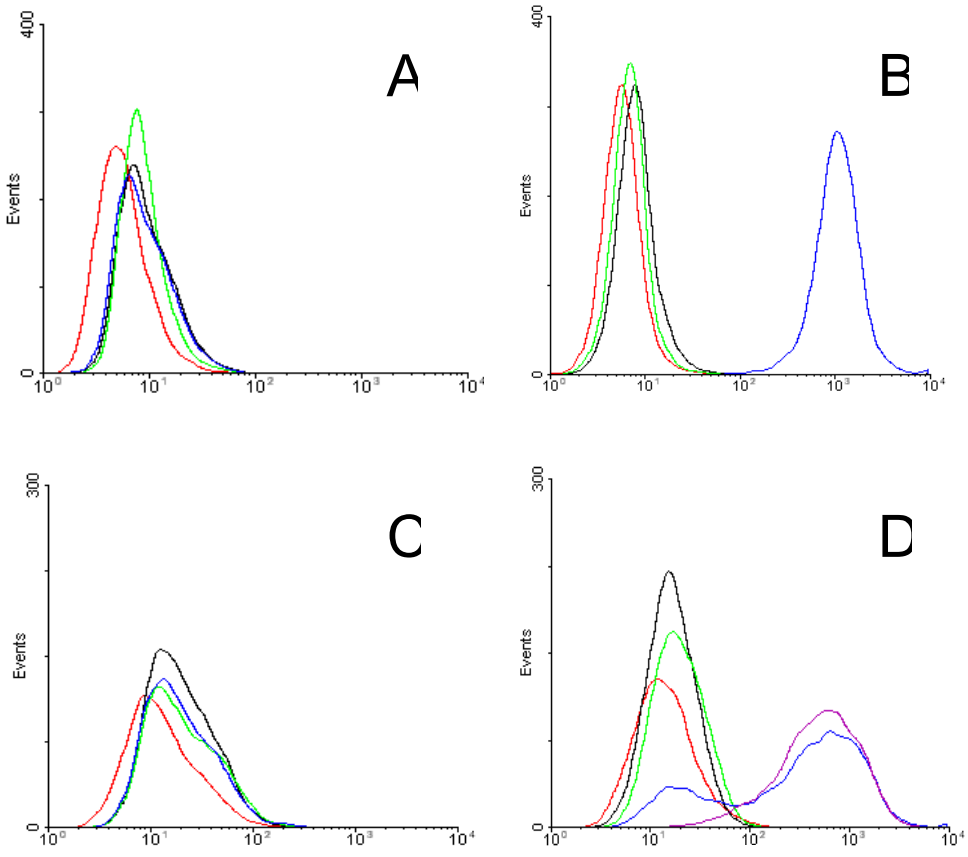


Figure 1.5. *Assessment of P-glycoprotein Expression by Immunocytochemical Staining and FACs Analysis*. Plots report the number of events versus the relative fluorescence intensity, reported in arbitrary units (logarithmic scale). Cell lines: mouse embryo fibroblasts A) wild type NIH3T3 and B) human MDR1 transfected NIH-MDR-G185; pig kidney cells C) wild type LLC-PK1 and D) transfected LLC-MDR-PK1 grown with (magenta) or without (blue) selecting agent vinblastin. Colored lines correspond to (red) untreated cells, (black) control antibody, (green) FITC-labeled anti-mouse $IgG_{2ak}$, and (blue and magenta) MRK16.

For comparison, the measurements of all cell lines with immunocytochemical MRK16 staining are summarized in Table 1.1.

| | NIH3T3 | LLC-PK1 | NIH-MDR-G185 | LLC-MDR-PK1 (vin) | LLC-MDR-PK1 |
|---|---|---|---|---|---|
| peak | 5.94 | 13.34 | 1027.35 | 632.09 | 620.82 |
| mean | 9.14 | 19.69 | 1044.49 | 475.44 | 248.51 |
| events | 8542 | 6655 | 9311 | 6485 | 7044 |

*Table 1.1. Quantification of fluorescence intensity upon MRK16-staining*. Peak: relative intensity corresponding to the top of the distribution curve. Mean: average of relative fluorescence intensity of the cell population. Events: number of cells representing the population included in the region of interest.

## Glycolytic Predominance in the Metabolism of Cultured Cells.

The predominance of glycolytic metabolites in cultures of mouse embryo fibroblasts, NIH-3T3, was investigated by $^{13}$C-NMR spectroscopy. For this experiment, 3.5 g/L [u-$^{13}$C]-D-glucose was added to the culture medium DMEM (containing 1 g/L normal D-glucose). After 24 hours incubation, cells were removed from culture and metabolites extracts were analyzed as described in section 1.3.

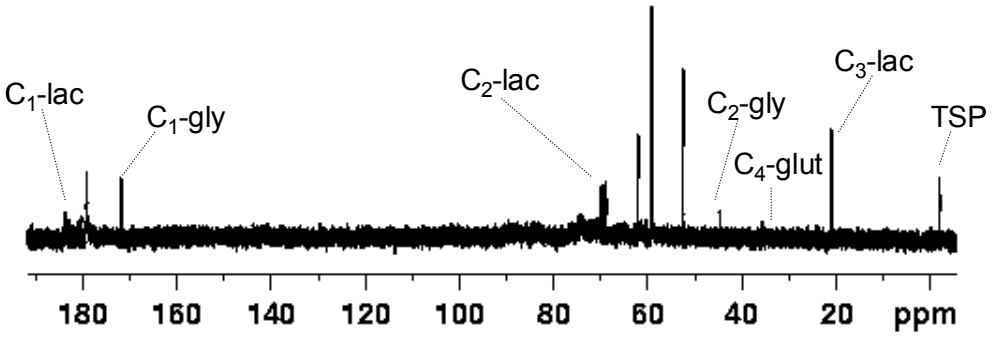


Figure 1.6. In *vitro* $^{13}$*C-NMR Spectroscopy of cell metabolite extracts.* Metabolites extracts of NIH3T3 fibroblasts after 24 hours incubation with 3.5 g/L [u-$^{13}$C]-D-glucose. The predominance of glycolysis is demonstrated by the incorporation of $^{13}$C in the resonance of lactate (C1: 179 ppm (doublet, 56 Hz coupling), C2: 69.5 ppm (doublet of doublet), C3: 21 ppm (doublet, 36 Hz coupling)). TSP (tetrasilanephosphate) was used as reference.

The uniformely $^{13}$C-labeled [u-$^{13}C_6$]-D-glucose was chosen, because the resulting homonuclear $^{13}$C spin coupling allows the unambiguous assignment of every metabolite that is produced from the glucose. As shown in Figure 1.6, most of the $^{13}$C was detected in the resonance of lactate ($C_1$: 179 ppm (doublet, 56 Hz coupling), C2: 69.5 ppm (doublet of doublet), C3: 21 ppm (doublet, 36 Hz coupling)) and not in TCA cycle derived metabolites. Indeed, the signal at 34 ppm, corresponding to C4-glutamate, is not higher than 2% of the C3-lactate signal, demonstrating that the cells prefer the anaerobic glucose metabolism over the

oxidative metabolism. The singlet resonances at 52, 59, 62 and 181 are assigned to a natural abundance compound not originating from the u-labeled glucose (13C-13C couplings) and is most likely pyro-glutamate formed by intramolecular condensation of supplemental glutamine from the cell culture medium. (Willker et al., 1995).

## Determination of Physical Chemical Parameters of Surfactants

As cited above, Pgp recognizes and binds its substrates directly from the inner leaflet of the lipid membrane. Passive diffusion is thus an important step in the kinetics of binding of compounds from the aqueous extracellular surroundings to the transporter. To characterize Pgp substrates from a physical chemical point of view, surface activity measurements have been performed (see section 1.3). From the Gibbs adsorption isotherms (π/logC plots) the following parameters have been obtained, i.e., the concentration of surface activity onset, $C_0$, the surface excess concentration, $\Gamma_\infty$, from which the cross-sectional area, $A_S$, can be calculated, the critical micellar concentration, CMC, and the air-water partition coefficient, $K_{aw}$, from which the lipid-water partition coefficient, $K_{lw}$, can be evaluated. Measurements of every single parameter are described in detail elsewhere (Nervi, 2000).

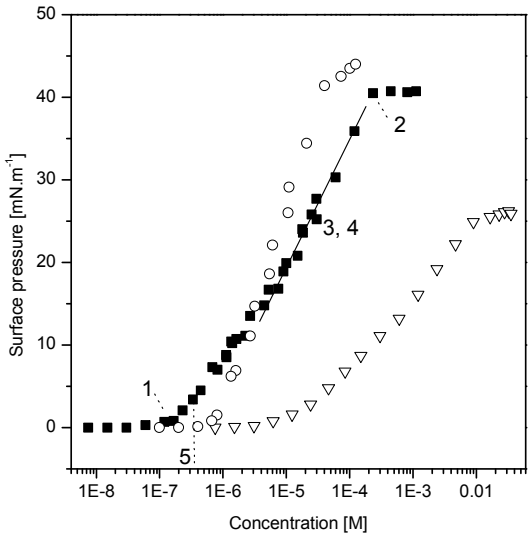


Figure 1.7. Gibbs Adsorption Isotherms (π/logC plots). The surface pressure, π, is plotted versus logC. (■) Triton X-100, (○) C12EO8, (▽) Chaps. From the plot, surface activity onset concentration (1), critical micellar concentration (2), surface excess concentration (3), cross.sectional area (4) and air-water partition coefficient (5), can be obtained.

The air-water partition coefficient, $K_{aw}$, the critical micelle concnetraiton, CMC, and the cross-sectional area, $A_s$, of the compounds are relevant for the present investigation and are

therefore listed in Table 1.2. Figure 1.7 shows π/logC plots of three nonionic surfactants i.e., Triton X-100 (■), C12EO8 (○) and Chaps (▽) as an example.

## Pgp-substrates Interactions observed in *Living* Cells by Microphysiometry.

### *A Transient Metabolic Change Occurs in Pgp-Overexpressing Cells Exposed to Pgp Substrates.*

In our experiments, the extracellular excretion of acidic metabolites in NIH3T3 and NIH-MDR-G185 mouse fibroblasts was used to monitor the cellular metabolism associated to Pgp ATPase activity. The extracellular acidification rate (ECAR) of cells was recorded in real time by microphysiometry. The ECAR of NIH3T3 and NIH-MDR-G185 in the presence of cell culture medium alone (see section 1.3) was considered as basal metabolic rate and defined as was defined as 100% (percent) or 1 (fold). All modulations of the ECARs induced by Pgp substrates were thus reported as fold or percentage variations of the basal rate.

Wild type NIH3T3 ($n$=13) and transfected NIH-MDR-G185 ($n$=25) cells induced an electrical potential variation of -66±(SD18;SE5) $\mu V \cdot s^{-1}$ and -64±(SD22;SE4) $\mu V \cdot s^{-1}$, respectively, corresponding to a pH variation of 1.1±0.3(SD) $mpH \cdot s^{-1}$ (NIH3T3) and 1.06±0.4(SD) $mpH \cdot s^{-1}$ (NIH-MDR-G185) on the silicon chip, where $n$ is the number of experiments made. The number of cells in the measuring chamber was ~ $4 \cdot 10^5$. Considering the phosphate buffer capacity of DMEM, a quantification of the ECAR leads to values of $(7.42 \pm 2.0) \cdot 10^6$ $H^+ \cdot s^{-1} \cdot cell^{-1}$ for NIH3T3 and $(7.15 \pm 2.7) \cdot 10^6$ $H^+ \cdot s^{-1} \cdot cell^{-1}$ for NIH-MDR-G185 cells. Such values illustrate the minimum amount of possible proton release, since the buffer capacity of other compounds, e.g. amino acids, has been neglected.

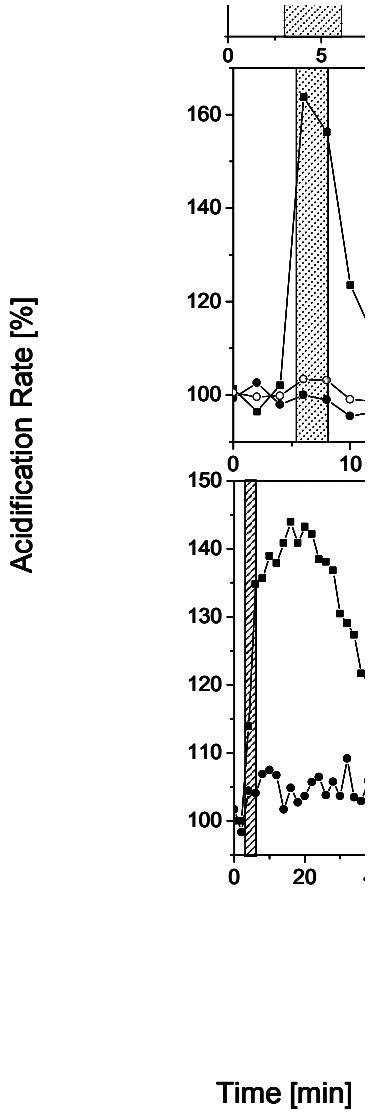


Figure3.4.x. Drugs and surfac
modulation of extracellular
rates (ECAR) in NIH-MDR-C
and NIH3T3 (?,?) cells by
verapamil; B) 10 µM triton
10 µM Tween 80. Results are
% of the basal activitv. whicl

Figure 1.8. *Drugs and Surfactant-induced* as *Modulation of Extracellular Acification* ''. *Rate (ECAR).* NIH-MDR-G185 (■,◆,▲) and NIH3T3 (●,○) cells. Stimulatons by A) 10 µM verapamil, B) 10 µM Triton X-100 and C) 10 µM Tween 80. Results are expressed in % of the basal activity, defined as 100%. Outlined areas indicate the stimulation period of 2'40''. The different time scale should be noted.

Figure 1.8 shows the reaction of wild type and transfected fibroblasts to the exposure of 10 µM verapamil (A), 10 µM triton X-100 (B), or 10 µM Tween80 (C), during and interval of 2 minutes and 40 seconds. The administration of these compounds induced a transient ECAR increase in Pgp-overexpressing, but not in wild type cells. For verapamil, a maximum ECAR of ~170% was reached in NIH-MDR-G185 cells after 40 sec, which returned to the basal value after ~30 min. Triton X-100 induced a maximum ECAR increase to ~160% after 40 sec and the recovery time was ~20 min, whereas Tween80 induced a maximum ECAR of ~145% after only 20 min and required ~90 min for complete recovery to the basal rate. For wild-type NIH3T3 cells, the drug-induced ECAR modulation of all compounds is much lower, if not negligible.

Drug- and detergent-induced ECAR modulations in NIH-MDR-G185 cells were investigated over a wide concentration range. The ECAR variation induced after 2'40'' of exposure to the compound was chosen for data evaluation (see section 1.3). In a first step, we screened several well-known Pgp-substrates, such as amitriptylin, cyclosporin A, verapamil and vinblastin, in order to asses the relationship between Pgp ATPase activation and ECAR. Data are reported in Figure 1.9.

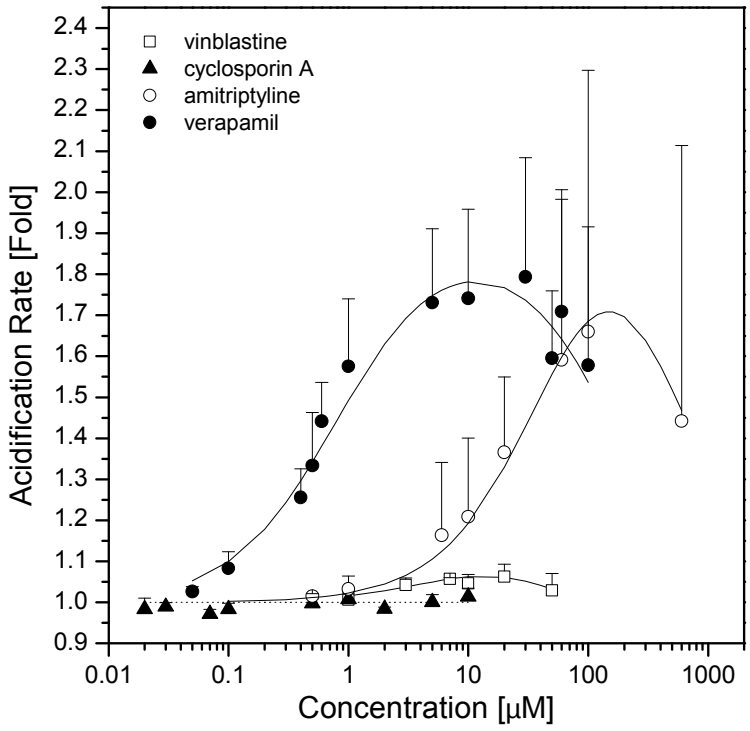


Figure 1.9. *Extracellular Acidification Rate (ECAR) of NIH-MDR-G185 Cells, as a Function of Drug Concentration*. Amitriptylin (○), vinblastin (□), cyclosporin A (▲), and verapamil (●). Dashed and continuous lines describe fits of the measurements according to a modified Michaelis-Menton model assuming activation with one and inhibition with two substrate molecules bound to the transporter (see equation 1 in section 1.3). Vertical bars show standard deviations.

Amitriptyline and verapamil showed a bell-shaped dependence of the ECARs as a fuction of concentration with maxima of about 1.8 - 2.0 times the basal activity. In one experiment, amitriptyline stimulation of cells led to very high ECAR values ($V_1 > 4.5$), which explains the high values for standard deviation. Vinblastine increased the ECAR of NIH-MDR-G185 less than 1.1 fold, whereas cyclosporine A (0.02 μM and 10 μM) did not induce any relevant ECAR modulation. Data were evaluated with a multiparameter fit (dashed and continuous lines) based on a modified Michaelis-Menton model (see Material and Methods) developed for previous investigations of inorganic $P_i$ release upon ATPase activity of Pgp (Litman et al., 1997). The kinetic parameters obtained from the fits are reported in Table 1.2. The comparison of data obtained in the present work, with data obtained from a parallel work (Landwojtowicz et al., 2002) with LLC-PK1 cell line, and from previous measurements of inorganic $P_i$ release data (Litman et al., 1997) is discussed in the next section.

### *Detergents can Act as Specific Modulators of the Cellular Metabolism Associated to Pgp ATPase Activity.*

To assess a possible specificity of the surfactant effect on Pgp ATPase activity, one zwitterionic detergent (chaps) and four nonionic detergents were chosen, i.e., two *n*-ethyleneglycol monododecylethers ($C_{12}EO_n$ , $n$=3 and $n$=8), triton X-100, Tween 80,. Experiments were performed the as for standard Pgp substrates in NIH-MDR-G185.

Whereas transient ECAR modulations were specifically induced by Triton X-100, Tween 80, and $C_{12}EO_8$ (see Figure 1.10B) and C)), no consistent selective ECAR modulations were produced with $C_{12}EO_3$ and Chaps.

Figure 1.10 shows the ECAR modulations induced by surfactants on NIH-MDR-G185, over a concentration range of four orders of magnitudes. On average (n=10 experiments) triton X-100 showed the ability to increase the ECAR of NIH-MDR-G185 cells up to ~ 1.4-1.6 fold of the basal activity, at a concentration around 10-12 μM. For higher concentrations, a progressive, reversible inhibition was observed. Likewise, $C_{12}EO_8$ enhanced the ECAR of NIH-MDR-G185 cells, with a maximum of ~ 1.8 fold of the basal activity at a concentration of ~ 6 μM. Tween 80 had also a specific effect on NIH-MDR-G185 cells (see also figure 1.8C), even though at a different time scale compared to triton X-100 and $C_{12}EO_8$. In contrast, $C_{12}EO_3$, induced a very low concentration-dependent ECAR modulation which was, however, observed in both transfected and wild type cells, and therefore was considered as not related to Pgp activity. Chaps which is known to be a non-substrate for Pgp, did not induce any ECAR modulation both in wild type and transfected fibroblasts, in a concentration range between 0.5 μM and 100 μM. Data could be fitted to the modified Michaelis-Menten model used for standard substrates. The kinetic parameters are reported in Table 1.2.

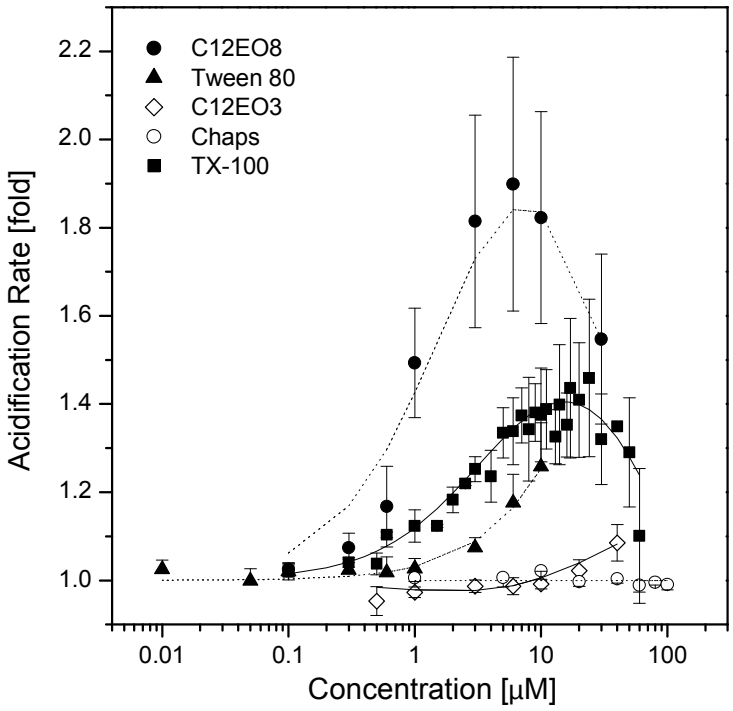


Figure 1.10. *Extracellular acidification rates (ECAR) of NIH-MDR-G185 cells, as a function of surfactant concentration*. Solid symbols represent: Triton X-100 (■), C12EO8 (●), Tween 80 (▲), C12EO3 (◇), and Chaps (○). Dashed and continuous lines report measurements fit according to the modified Michaelis-Menton model described as in figure 2. Standard deviations are shown.

The evidence for a direct interaction with Pgp was further investigated for Triton X-100. In Figure 1.11 the ECAR modulation induced by 8 μM Triton X-100 is shown in the presence of increasing concentrations (0 μM (A), 1 μM (B), and 10 μM (C)) of cyclosporin A. In the presence of 10 μM cyclosporin A, the effect of triton on NIH-MDR-G185 cells could be suppressed. This argues in favor of a specific competition mechanism.

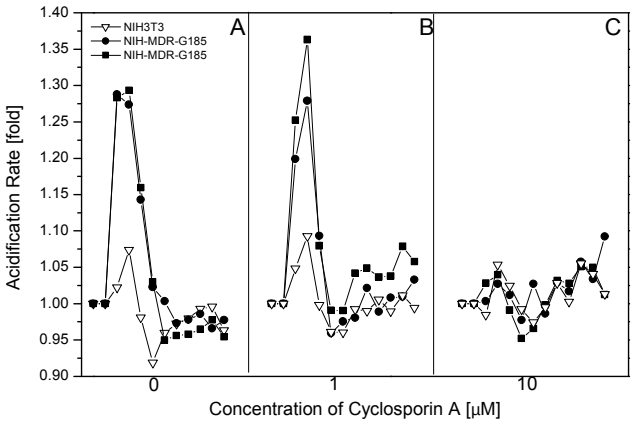


Figure 1.11. *Inhibition of Triton X-100-induced ECAR Increase by Cyclosporin A*. ECAR modulations in NIH-MDR-G185 (■,●) and NIH3T3 (▽) cells are shown, after 2'40'' exposure to 8 μM triton X-100 alone (A), and in the presence of 1 μM (B) and 10 μM (C) cyclosporin A, respectively.

## *Membrane Solubilizing Effect of Triton X-100.*

So far, the effect of detergents on the ECAR of Pgp overexpressing cells were investigated at concentrations below the critical micellar concentration (CMC). Under these conditions the effects of detergents were fully reversible. Figure 1.12 shows the response of NIH-3T3 and NIH-MDR-G185 cells to an exposure of Triton X-100 (0.3 mM) above the critical micelle concentration (CMC = 0.23 mM) during the same period of time as applied in experiments shown in Figure 1.8 (2'40''). This lead to a rapid and irreversible ECAR decrease in both, wild type and transfected cells and can be attributed to cell lysis.

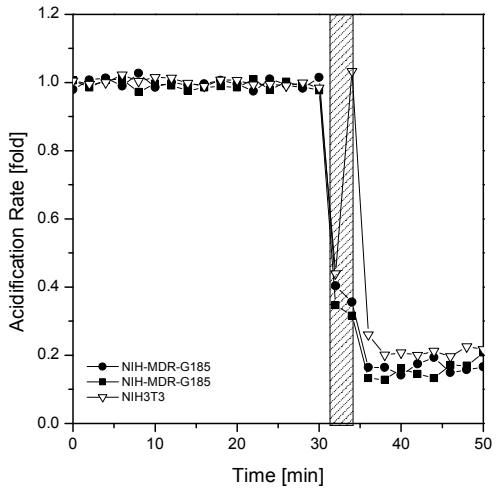


Figure 1.12. Cell lysis upon detergent action. Exposure of NIH-MDR-G185 (■,●) and NIH3T3 cells to 300 μM triton X-100 during a period of 2'40'' (outlined area). ECAR modulations are expressed in fractions of the basal activity, which is arbitrarily defined as 1.0.

| Substrate | MW [g/mol] | HAP Type | HA Dist. [Å] | EU [a.u.] | pKa | 1/Kaw [uM] pH7.4 | CMC [uM] pH7.4 | ΔΔGam [kJ/mol] pH7.4 | AD [Å] pH8.0 | K1 [uM] * | K2 [uM] * | V1 [fold] * | V2 [fold] * | K1 [uM] ** | K2 [uM] ** | V1 [fold] ** | V2 [fold] ** | K1 [uM] *** | K2 [uM] *** | V1 [fold] *** | V2 [fold] *** |
|---|---|---|---|---|---|---|---|---|---|---|---|---|---|---|---|---|---|---|---|---|---|
| Amitriptyline | 277.4 | aa (1, 3) | 2.55 | 2 | 9.4 | 277.8 | 5000 | -6.96 | 52 ± 4 | 50.00 | 550 | 2.2 | 0.75 | 80 | 400 | 1.47 | 0.8 | 108 | 110 | 2.3 | 0.9 |
| | | aa (1, 4) | 2.86d | | | | | | | | | | | | | | | | | | |
| C12EO3 | 318.5 | AA(1;7) | | 0(2) | - | 1.35 | 50 | | 35 | 1 | 36.25 | 0.95 | 1.19 | n.d. | n.d. | n.d. | n.d. | n.d. | n.d. | n.d. | n.d. |
| C12EO8 | 538.8 | AA(1;7) | | 6 | - | 0.455 | 110 | | 58 | 1.67 | 57.5 | 2.1 | 0.3 | n.d. | n.d. | n.d. | n.d. | n.d. | n.d. | n.d. | n.d. |
| | | AA(1;10) | | | | | | | | | | | | | | | | | | | |
| | | AA(1;13) | | | | | | | | | | | | | | | | | | | |
| Calcein-AM | 994.9 | AA (1, 3) x 9 | 2.28 | 23 | 5 | 0.38 | 3 | -4.88 | 69 | 7.2 | 10 | 1.29 | 1.24 | 0.12 | 0.25 | 0.8 | 1.1 | n.d. | n.d. | n.d. | n.d. |
| | | AAa (1,3,7) x 2 | 4.54 | | | | | | | | | | | | | | | | | | |
| Chaps | 614.9 | - | | - | | 29.16 | 600 | | 93 | - | - | - | - | n.d. | n.d. | n.d. | n.d. | n.d. | n.d. | n.d. | n.d. |
| Cyclosporine A | 1203 | Aa (1, 3) x 7 | 2.27 | 12.5 | - | 0.05 | n.d. | n.d. | n.d. | 0.05 | 7 | 1.06 | 0.98 | 0.02 | 2 | 1.08 | 0.8 | 0.1 | 1.7 | 1.1 | 0.6 |
| | | AA (1, 5) | 4.74 | | | | | | | | | | | | | | | | | | |
| Diltiazem | 414.5 | AA (1, 3) | 2.28 | 3.5 | 8.06 | 37.15 | 480 | -6.13 | 70 ± 3 | n.d. | n.d. | n.d. | n.d. | 25 | 190 | 1.45 | 0.8 | 73 | 677 | 3.3 | 0 |
| | | Aa (1, 3) | 2.28 | | | | | | | | | | | | | | | | | | |
| Progesterone | 314.5 | Aa (1, 3) | 2.63 | 1.5 | - | 28.82 | 80 | -2.22 | 100±10 | n.d. | n.d. | n.d. | n.d. | 17 | 200 | 1.41 | 0.6 | 18 | 294 | 2.6 | 0.3 |
| Trifluoperazine | 407.5 | aa (1, 3) | 2.14 | 3 | 3.91 | 5.13 | 170 | -8.33 | 58 | n.d. | n.d. | n.d. | n.d. | 12 | 100 | 1.33 | 0.7 | 6.5 | 24 | 2 | 0.6 |
| | | aa (1, 3) | 2.6 | | 8.09 | | | | | | | | | | | | | | | | |
| | | aa (1, 4) | 2.94 | | | | | | | | | | | | | | | | | | |
| Triton X-100 | 647 | AA(1;7) x2 | | 6 | - | 0.81 | 230 | | 54 | 4.24 | 150 | 1.63 | 0.3 | n.d. | n.d. | n.d. | n.d. | n.d. | n.d. | n.d. | n.d. |
| | | AA(1;22) | | | | | | | | | | | | | | | | | | | |
| Tween 80 | 1310 | AA (1, 3) | | 6(+2n) | - | 0.12 | 10 | | 69 | 41 | 200 | 2.1 | 0.7 | n.d. | n.d. | n.d. | n.d. | n.d. | n.d. | n.d. | n.d. |
| | | AA (1, 4) | | | | | | | | | | | | | | | | | | | |
| | | AA (1, 5) | | | | | | | | | | | | | | | | | | | |
| | | AA (1, x) xn | | | | | | | | | | | | | | | | | | | |
| R/S-Verapamil | 454.6 | AA (1, 4) | 2.69 | 5 | 8.6 | 6.02 | 320 | -9.47 | 71 ± 2 | 0.8 | 210.8 | 1.89 | 0.8 | 1.5 | 100 | 1.25 | 0.9 | 2.5 | 99 | 2.1 | 0.6 |
| | | AA (1, 4) | 2.69 | | | | | | | | | | | | | | | | | | |
| | | aa (1, 7) | 4.73 | | | | | | | | | | | | | | | | | | |
| Vinblastine | 811 | AAA (1, 3, 5) | 3.54d | 8.5 | 5.4 | 2.14 | 100 | -9.21 | 140 ± 4 | 5.33 | 40 | 1.12 | 0.93 | 7 | 55 | 1.11 | 1 | 1.3 | 17 | 1.5 | 0.5 |
| | | AA (1, 3) x 2 | 2.28 | | 7.4 | | | | | | | | | | | | | | | | |
| | | Aa (1, 5) | 4.95 | | | | | | | | | | | | | | | | | | |

* Scientist: Pierluigi Nervi; Cell Line: NIH-3T3/NIH-MDR-G185; Method: Cytosensor

** Scientist: Ewa Landwojtowicz; Cell Line: LLC-PK1/LLC-PK1-MDR; Method: Cytosensor

*** Scientist: Thomas Litman; Cell Line: Caco-2; Method: Reconstituted vesicles, Pi release

Table 1.2. *Physical Chemical and Kinetical Parameters of Standard P-gp Substrates and Surfactans.*

## 1.5 Discussion

The aim of the present project was to contribute to the elucidation of the multidrug resistance (MDR) phenotype, associated to the expression of Pgp in the plasma membrane of living cells by studying the interactions between the human *MDR1* gene product, P-glycoprotein (Pgp), and its substrates. To this purpose we established a method based on microphysiometery which allows studying standard Pgp-substrate interactions in *living* cultured mammalian cells.We then applied this technique (i) to investigate the relationship between ECARs in MDR1 transfected cells *in vivo* and Pgp ATPase activity in inverted plasma membrane vesicles (Litman) both induced by well-known Pgp substrates and ii) to analyze surfactants, as potential Pgp substrates in *living* cells. (iii) The kinetic data obtained for the interaction of detregents with Pgp were then related to their physical chemical parameters, conformational properties and hydrogen bond acceptors patterns (Seelig, 1998).

### P-glycoprotein ATPase Activation can be monitored on-line in Living Cells

Conventional studies of drug-induced Pgp ATPase activity are usually based on measurements of inorganic phosphate ($P_i$) release as a result of ATP hydrolysis and are performed either in reconstituted systems, or in inverted plasma membrane vesicles extracted from cells overexpressing Pgp (Litman et al., 1997; Sauna and Ambudkar, 2000). Here, we adapted a technique that allows, real-time monitoring of the metabolic activity of intact living cells, to the investigation of drug-induced stimulation of Pgp ATPase activity.

The turnover of energy production and consumption through the complex metabolic network of a cell is coupled with the production of waste acidic metabolites which need to be excreted into the extracellular environment, in order to keep a favourable intracellular pH. Using a Cytosensor™ Microphysiometer System (McConnell et al., 1992), it has been possible to detect the extracellular release of acidic metabolites ($H^+$), by measuring extracellular pH changes during cell stimulation with various compounds as a function of time, with a sensitivity of 0.001 pH units/min. Extracellular acidification reflects the overall cellular metabolism. Therefore, to monitor activation of a specific transporter or receptor, such as Pgp, reference and model systems with background activity as similar as possible are required. Wild type mouse embryo fibroblasts, NIH3T3, and the same cell line transfected

with the human MDR1 gene, NIH-MDR-G185, showed to be an ideal system for the study of Pgp-substrates interactions with the microphysiometer. In NIH-MDR-G185, FACs analysis showed a stable Pgp expression level higher than that in NIH3T3 by a factor of $10^3$, while the amount of Pgp in NIH3T3 cells was insignificant (see Figure 1.5 A) and B)).

As shown in Figures 1.8 and 1.9, ECAR changes were induced in NIH-MDR-G185 cells, after exposure to Pgp substrates, but not in wild type cells. Since the Pgp expression level is the main difference (other minor differences in gene expression may have been induced by the transfection; M. Gottesman, personal communication) between wild type and transfected cells, one can conclude that extracellular acidification is a response to the drug induced ATPase activation of the transporter. Moreover, the drug induced ECAR modulations measured as a function of concentration in Pgp expressing cells could be fitted with a modified version of the Michaelis-Menten equation, a model initially proposed by Litman and coworkers (Litman et al., 1997) for the assessment of inorganic phosphate release in CR1R12 inverted membrane vesicles. This model assumes activation with one substrate molecule bound, and an inhibition after a second drug molecule binds to the transporter (see section 1.3). A linear correlation between the activation constants, $K_1$, and the maximum velocities, $V_1$, derived from ECARs and phosphate release measurements,respectively, were also observed for LLC-MDR1 pig kidney cells, (Landwojtowicz et al., 2002). Interestingly, consistent shifts of the maximum velocities, $V_1$, induced by different Pgp substrates were observed depending on the system used for the measurements. For example, the concentration-dependent ECAR profile induced by verapamil stimulation, showed a shift of $V_1$ by a factor of ~ 1.55 between NIH-MDR-G185 cells ($V_1$ ~ 1.8-1.9 · basal rate) and LLC-MDR1 cells ($V_1$ ~ 1.2-1.3 · basal rate). This difference was assumed to be correlated to the different amount of Pgp expressed in the model employed. To test this assumption, we investigated the Pgp expression level in NIH-MDR1 and LLC-MDR1 cells. As shown in Figure 1.5 (data reported in table 1.1), FACs analysis by MRK16 monoclonal antibody staining (see section 1.3) showed that the Pgp expression level in NIH-MDR-G185 cells is a factor ~ 1.6 higher than in LLC-MDR1 cells, which is in good agreement with the difference found for the maximum ECARs in the two cell lines. From this, it was concluded that also the difference between $V_1$ in LLC-MDR1 cells (Landwojtowicz et al., 2002) and reconstituted vesicles was related to different Pgp expression levels.

The validity of microphysiometry as a method for on-line monitoring of drug-induced Pgp ATPase activation in living cells was further supported by a quantitative determination and comparison of the turnover numbers of Pgp, calculated from our ECAR data (NIH-MDR-G185 fibroblasts) and previous data obtained from $P_i$ release experiments. In a previous study, the amount of Pgp molecules/cell was estimated as ~ $1.95 \cdot 10^6$ Pgp copies/cell (≅ 0.56 pg Pgp/cell) for NIH-MDR-G185 cells by Ambudkar and coworkers (Ambudkar et al., 1997), by titrations with Pgp-specific monoclonal antibody UIC2. From these values, the same group determined the turnover of Pgp during pumping of verapamil, in terms of $P_i$ release. At maximum activation, the turnover was estimated as ~3.26 $P_i \cdot s^{-1} \cdot Pgp^{-1}$ (Kerr et al., 2001). We thus calculated the corresponding turnover number from ECAR data obtained by microphysiometry. Taking into account the number of cells (~ 1-4 $\cdot 10^5$) contributing to the observed acidification rate in the capsule cups and the minimal buffer capacity of the running medium, turnover numbers at basal rate and maximum activation were calculated. For verapamil, a turnover at maximum Pgp activation was estimated as ~ 3.2 $H^+ \cdot s^{-1} \cdot Pgp^{-1}$, which is in striking agreement with the number determined for $P_i$ release. Data are reported in Table 1.3. It should be noted that these calculations involve several approximations. For example, the actual buffer capacity of DMEM would be higher, taking into account the contribution of compounds other than phosphate buffer (e.g. amino acids). Nevertheless, these results provide a reasonable estimation of the Pgp turnover, and support the assumption of a direct correlation between ECAR and intracellular $P_i$ release from ATP hydrolysis by Pgp.

| Compound | Vmax fold | Turnover $H^+*s^{-1}*Pgp^{-1}$ | ECAR $H^+*s^{-1}*cell^{-1}$ |
|---|---|---|---|
| amitriptyline | 2.2 | 4.324 | 8579640 |
| C12EO3 | - | - | - |
| C12EO8 | 2.1 | 3.964 | 7864670 |
| Calcein-AM | 1.29 | 1.045 | 2073413 |
| Chaps | - | - | - |
| Cys A | - | - | - |
| Triton X-100 | 1.63 | 2.27 | 4504311 |
| Tween 80 | 2.1 | 3.964 | 7864670 |
| verapamil | 1.89 | 3.21 | 6005748 |
| vinblastine | 1.12 | 0.432 | 857964 |

Table 1.3. *Turnover numbers for P-glycoprotein activity during maximum activation upon interaction with substrates*. The maximum velocity (Vmax, fold of basal value) was determined in Pgp overexpressing living mouse embryo fibroblasts, NIH-MDR-G185, by fitting drug concentration-dependent ECAR profiles with a modified Michaelis-Menton model. The turnover numbers, expressed in terms of extracellular proton release/cell/second, is calculated assuming the presence of ~ 0.56 pg Pgp/cell.

## Direct involvement of Pgp in the substrate transport-coupled proton excretion.

Several factors reported here suggest a direct coupling between Pgp ATPase activity (therefore $P_i$ and substrate transport) and the drug-modulated excretion of protons by cells, i.e. i) the linear correlation between kinetic constants obtained from extracellular $H^+$ release and intracellular $P_i$ release in independent studies (Landwojtowicz et al., 2002); ii) the correspondence between the maximum velocities for drug-induced proton transport and the cellular Pgp expression level; iii) the quantitative correspondence of turnover numbers obtained independently from ECAR and $P_i$ release data (see above); iv) the possibility to competitively inhibit the compound-induced ECAR change with Cys A (see Figure 1.11 here and Figure 5 in (Landwojtowicz et al., 2002)), and v) the exclusion of the contribution of other important pH regulating transporters, such as $Na^+/H^+$ and $Cl^-/HCO_3^-$ antiporters, to the drug-induced ECAR (Landwojtowicz et al., 2002)

Moreover, we have shown that lactate is the main acidic product resulting from wild type cell activation, pointing to an essentially glycolytic pathway of ATP synthesis. It can therefore be assumed that ATP for driving Pgp activation in MDR1 transfected cells is also produced via the glycolytic pathway.

## The Effect of Drugs on Pgp ATPase Activity is related to their Hydrogen Bonding Potential and their Partition Coefficient for Lipid Membranes.

As described previously (Seelig and Landwojtowicz, 2000), the inverse of the concentration required for half-maximum activation of the transporter ($K_1$) can be linearly correlated with the air-water partition coefficient ($K_{aw}$) of the substrate molecule, in a double logarithmic plot. Moreover, $K_{aw}$ provides a good estimation of the lipid-water partition coefficient, $K_{lw}$ (see section 1.2) It was therefore assumed that the membrane insertion step,is rate limiting for the interaction of a substrate with Pgp.

Pgp substrates structural features were further screened according to the recognition pattern model proposed earlier (Seelig, 1998). Figure 1.13 shows the maximum ($V_1$) and minimum ($V_2$) ECARs induced by drugs and surfactants in living Pgp-overexpressing cells, plotted as a function of the number of H-bond acceptor patterns (HAU's) on substrates. The maximum activity, $V_1$, is high for compounds with a low affinity for the transporter (=low number of H-bonding (or energy) units, see section 1.3) and decreases exponentially with increasing substrate affinity for the transporter (=higher H-bonding strength (see Table 1.2)). For example, compounds like cyclosporin A, which is considered as a Pgp inhibitor, possesses 12.5 EU's, and gives almost no ECAR activation. On the other hand amitriptyline, which has only 2 EU, induced an ECAR increase up to ~ 2 fold, compared to the basal metabolic activity.

The comparison of these kinetic data obtained from the two cell lines, namely LLC-MDR1 (Landwojtowicz et al., 2002) and NIH-MDR-G185, reflects the different Pgp expression levels detected by FACs analysis (see Figure 1.5). Although the shapes of the curves are similar, NIH-MDR-G185 induces consistently higher $V_1$. A less distinct correlation is observed for $V_2$. This is most probably due to the fact that the minimum rate is obtained mathematically from the fitting procedure and can not be measured.

From the combination of these parameters, i.e., maximum ECAR activation and H-bonding strength, the potential of a substrate to act as modulator or inhibitor can be assessed. As shown in Figure 1.10 of the present study and elsewhere (Landwojtowicz et al., 2002), further experiments demonstrate a direct competition between two compounds for H-bonds formation with the transporter. In this sense, inhibitors like cyclosporin A would block the action of other substrates, by occupying much more "binding sites" of Pgp per drug molecule.

Indeed, the higher the number of EU of the competing molecule, the weaker the inhibitory effect of cyclosporin A.

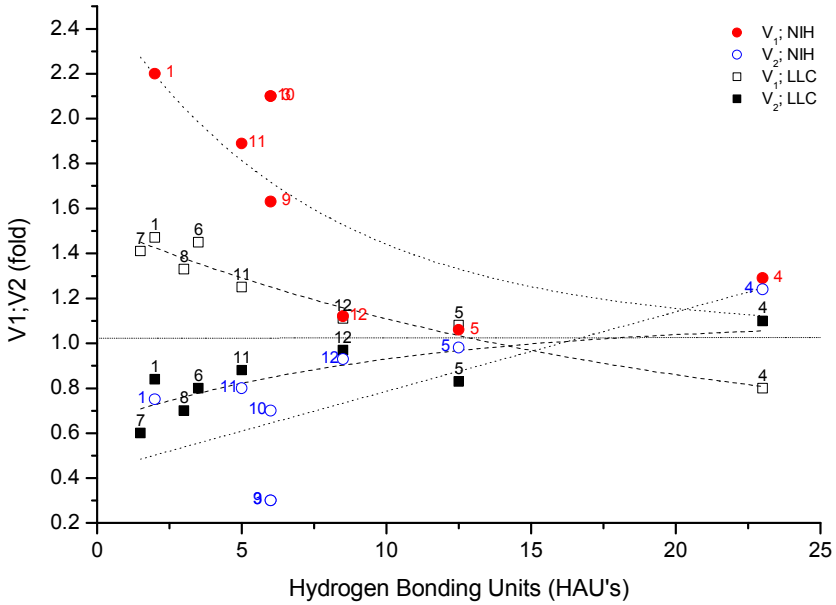


Figure 1.13 *Influence of the H-bonding energy on the rate of drug-induced ATPase activation in living MDR1 overexpressing cells*. The maximum ($V_1$) (open black squares, solid red circles) and minimum ($V_2$) (open blue circles, solid black squares) extracellular acidification rates (ECAR) are plotted as a function of the H-bonding energy. 1) amitriptylin; 2) C12EO3; 3) C12EO8; 4) calcein-AM; 5) cyclosporine A; 6) diltiazem; 7) progesterone; 8) trifluoperazine; 9) Triton X-100; 10) Tween 80; 11) verapamil; 12) vinblastin. Circles indicate data from NIH-MDR-G185 cells, while the squares correspond to data from LLC-MDR1 cells taken from (Landwojtowicz et al., 2002) for comparison.

## Surfactants as specific modulators of P-glycoprotein ATPase activity

The successful development of microphysiometry for the study of Pgp-substrate interaction with standard substrates, suggested the possibility to investigate the role of surfactants as potential substrates for Pgp. To this purpose, we screened four nonionic detergents, e.g. Triton X-100, C12EO8, C12EO3, Tween 80 and a zwitterionic, Chaps, for their effect on the ECAR of NIH3T3 and NIH-MDR-G185 cells. In agreement with previous observations, Chaps showed to be a non-substrate for Pgp, as no ECAR change was observed. From a physical chemical point of view, two characteristics make this compound a non-substrate for Pgp. Indeed, i) Chaps is a zwitterionic molecule and therefore the rate of flip-flop into the inner leaflet of a biological membrane (an essential step for the recognition from Pgp) is extremely low, and ii) in agreement with the reported recognition pattern model (Seelig, 1998) no H-bond acceptor patterns are present on this compound.

Polyethoxylated nonionic surfactants, e.g, Triton X-100, Tween 80, C12EO8 and C12EO3 are in contrast electrically neutral, which allows a fast flip-flop. In addition, polyethoxylated detergents carry a variable number of hydrogen bond acceptor groups.

Triton X-100 showed an evident concentration dependent effect on the ECAR of NIH-MDR-G185 cells, as shown in Figure 1.10. Such molecule carries several (7 to 15) ethoxylated groups in the hydrophylic tail, which could form H-bonds with Pgp. However, in contrast to other Pgp substrates, like most drugs which show rather rigid H-bond acceptor patterns the highgly flexible polyethoxylated chains most likely form only transient H-bond acceptor patters. Therefore the number of EU's given has to be considered as an upper limit. Computer 3D-modelling and the comparison of the maximum velocity, $V_1$, with standard compounds such as verapamil, allowed an estimation of the potential H-bond energy of Triton X-100 of ~ 5-6 EU.

The hypothesis of a direct interaction of Triton X-100 with Pgp was supported by competition experiments with cyclosporin A. Stimulations with Triton X-100 (8 μM) were performed after 20 min incubation with cyclosporin A (1 μM and 10 μM, respectively). While 1 μM cyclosporine A had little effect on the Triton X-100 induced ECAR, 10 μM of the same compound could inhibit the Pgp response to Triton X-100 stimulation almost totally (see Figure 1.11).

The octaethyleneglycol monododecilether, C12EO8, showed an effect on Pgp ATPase activity similar to Triton X-100, even though with higher $V_1$ values. Even though an analogous number of EU's has been evaluated by computer modelling simulation *in vaco*, the broad range of the length of the ethoxylated chains in Triton X-100 (n = 7 to 15) may lead effectively to different number of EU. Moreover the two compounds, C12EO8 and Triton X-100, differ in the structure of the hydrophobic cores, resulting in different amphyphilicities.

To reduce the influence of structural differences and to thus assess the role of H-bond acceptor patterns for the interaction with Pgp more precisely, we also investigated the non-ionic detergent triethyleneglycol monododecylether, C12EO3. This surfactant differs from C12EO8 due to its shorter ethoxylated, hydrophylic tail. Despite its detergent action (Heerklotz and Seelig, 2000), C12EO3 had almost no influence on the ECAR of NIH-MDR-G185, arguing again in favour of a direct detergent-Pgp interaction through a specific recognition pattern as a basis for the ECAR increase.

Finally, Tween 80, which carries four polyethoxylated tails with totally 20 ethoxylated groups, produced a selective increase of the ECAR of NIH-MDR-G185 cells, similarly to C12EO8 and Triton X-100. The higher hydrophilicity of Tween 80, compared to that of the other nonionic detergents was evident in surface activity measurements. In addition the time required to reach a stable surface pressure was much longer than for Triton X-100 or C12EO8 (data not shown). The slow partitioning into the air-water interface most likely reflects the slow partitioning into the membrane-water interface. As a result the membrane concentration has not reached its maximum value at the stimulation time appropriate for the other compounds invsdtigated ( 40s + 2min) as seen in figure 1.8C.

The maximum ECARs induced by detergents in NIH-MDR-G185 cells are plotted together with standard Pgp substrates, in Figure 1.13. It is evident that the detergents fit the exponential curve drawn through standard Pgp substrate quite well, except tween for which the number of effective H-bond acceptor patterns seems to be clearly over estimated. Considering the flexible structure of these ethoxylated detergents and thus the lack of rigid H-bond acceptor patterns, the $V_1$ can be traced back to the exponentially decay tendence, as for standard compounds. Probably, the actual HAU number of such detergents is a bit less than what determined by vacuum 3D-modelling, considering the restriction of freedom when inserted in a membrane. Finally, as mentioned in several works, the action of detergents in

disturbing Pgp activity indirectly by changing the order parameters of a biomembrane, is well possible. However, this feature is also observed in standard Pgp substrates (Schuldes et al., 2001).

Our findings show that the presence of H-bonding donor groups plays a role in the interaction of detergents with Pgp, similarly to that found for standard Pgp substrates. Most probably, the exact description of the mechanism of action of these molecules in alterating Pgp ATPase activity involve the synergistic contribution of both solubilizing effect and a specific H-bond mediated interaction with the transporter (Seelig and Gatlik, Minireviews, in press).

In conclusion, our results suggest therefore that not only drugs, but any compound which has recognition patterns, e.g. drug additives, can interact with P-glycoprotein. Drug additives with such features may have profound effects on drug absorption and should therefore be considered carefully for the development of drug formulations.

# Part Two: The Cell Penetrating Peptide HIV-1TAT-PTD


## Summary

The aim of the present work was to find possible interaction mechanisms of the cell-penetrating peptide (CPP) HIV-1 TAT-PTD with *living* cells. Recently, it has been postulated that the penetration mechanism observed in several studies is, actually, an artifact occurring during cell fixation with paraformaldehyde or methanol, a commonly used treatment for the preparation of cells for epifluorescence microscopy analysis. Our intent was to perform observations of the interaction of the CPP with cells, while preserving *in vivo* conditions without the use of fixation. Microphysiometry and confocal microscopy turned out to be adequate methods for our purpose. By means of these techniques, we measured (i) the ability of HIV-1 TAT-PTD to penetrate into non-fixated living mouse embryo fibroblasts, NIH-3T3, (ii) the kinetics of the uptake process, (iii) the inhibition of the peptide uptake with exogenous heparan sulfate or by enzymatic digestion of the extracellular glycosaminoglycans with heparinases, and (iv) the possible occurrence of structural alterations on the cells, as well as (v) functional changes, e.g., metabolic modulations. Our experiments showed clearly that HIV-1 TAT-PTD penetrates into intact cells, thus excluding the hypothesis of a fixation artifact: the penetration occurred in a time scale of seconds. However, not all cells integrated the peptide.

Morphological alterations appearing as dense dark aggregates, to which the trivial denomination of “dark spots” was attributed, were observed on the cell surface using differential interference contrast (DIC) microscopy. Such aggregates were present exclusively on fibroblasts presenting TAT-PTD uptake and their size increased during the uptake process. The enzymatic removal of extracellular heparan sulfate, as well as the simultaneous addition of exogenous heparan sulfate with TAT-PTD reduced the uptake of TAT-PTD and the appearance of aggregates. Moreover, in the case of simultaneous addition of heparan sulfate, the appearance of small aggregates in the surrounding medium was observed. The latter observations argue in favor of the theory that the aggregates are composed of TAT-PTD bound to the GAG heparan sulfate.

The experiments *in vivo* were supported by measurements *in vitro*. The binding constant of the fluorescent CPP interaction with heparan sulfate, $K = 4.6 \cdot 10^4\ M^{-1}$, was determined by isothermal titration calorimetry (ITC). The interaction of Fg-TAT-PTD and heparan sulfate *in vitro* induced fluorescence quenching and formation of aggregates, in analogy to the observations with confocal microscopy. Finally, we found that the administration of TAT-PTD specifically induced alterations of the extracellular acidification rate (ECAR) of NIH-3T3 fibroblasts, which reflects a disturbance of the overall cellular metabolism. These latter findings allow at the same time some considerations on the potential toxicity of such a compound to mammalian cells.

# Chapter 2. Interactions of HIV-1 TAT Protein Transduction Domain with Living Fibroblasts.

## 2.1 Introduction

A biological lipid bilayer constitutes an efficient barrier against the intracellular penetration of biomolecules. This property is essential for the protection of tissues and for the appropriate compartmentalization of different biological environments inside an organism. However, such a protective mechanism can represent a disadvantage during the pharmacological treatment of diseases, by reducing the bioavailability of therapeutic and diagnostic agents. Therefore, during the last half century, pharmacological research has been directed towards the development of drugs and pharmaceutical delivery formulations that optimize the passage of the drug through the cell membrane in order to reach biological targets (organs, tissues, cells). The developed administration strategies include encapsulation of the active compounds into liposomes or their linkage to so called cell-penetrating peptides (CPPs, not yet commercialized). The latter are polypeptides with many positively charged amino acids, which enhance the intracellular transport of almost every kind of covalently attached molecule, from proteins (Schwarze et al., 1999; Stein et al., 1999) to nucleic acids (Eguchi et al., 2001), from small drug molecules (Nori et al., 2003; Rothbard et al., 2000; Wender et al., 2002) to large liposomal or metal particles (Lewin et al., 2000; Torchilin et al., 2001). If Fe is taken up by the cells, then the MRI image contrast changes in analogy to the intravascular contrast agent endorem used in chapter 3.

The first report on the involvement of polycationic peptides as enhancers of drug delivery appeared in 1968. Twenty years after the first observation of genetic transformation in pneumococci (Avery, 1944, J. exp. Med. 79, 137), attempts were made to achieve genetic transformation of higher organisms by means of nucleic acids extracted from infectious or oncogenic viruses, in order to initiate infection or malignant transformation. Focusing on the biological effect of infection or transformation, little importance was attributed to the specific physiology of uptake of the exogenous molecules. This gap was clearly highlighted in a report of H. J.-P. Ryser (Ryser, 1968) who showed interest in the details of adsorption and uptake of macromolecules by mammalian cells. In his work (Ryser, 1968), Ryser discovered that incubating cultured mammalian cells with natural histones (Lys-rich) or synthetic polycationic peptides, such as polylysine, polyarginine or polyornithine, led to an improved cellular uptake of exogenous proteins.

Twenty years later, a natural compound with similar physical chemical features was discovered. A natural polycationic peptide was derived from the HIV-1 tat protein, an 86-amino acid protein that was identified as the trans-acting activator of the transcription (TAT) of the human immunodeficiency virus (HIV-1) (Frankel and Pabo, 1988; Frankel and Pabo, 1988). This peptide was able to cross efficiently the cytoplasmic membrane of mammalian cells in culture (Frankel and Pabo, 1988; Green et al., 1988) and, moreover, was able to carry and transport covalently attached heterologous proteins and fluorescent dyes into cells (Fawell et al., 1994; Mann and Frankel, 1991). More recently, further polycationic peptides with membrane translocating activities were discovered, both of synthetic or natural origin, e.g. transportan (Pooga et al., 1998; Soomets et al., 2000), antennapedia (AntP) (Derossi et al., 1994; Lindsay, 2002), and herpes simplex virus HSV-1 VP22 (Bennett et al., 2002). These compounds have different primary structures and different natural biological functions. However, because of their common functionality in the enhancement of cellular uptake, they all have been classified as cell-penetrating peptides (CPPs) (Lindgren et al., 2000) or trojan horse peptides (Derossi et al., 1998). In spite of its similar physical chemical features, polylysine is less efficient and has not been included in this group (Mitchell et al., 2000).

The proper physical mechanism of uptake of CPPs is actually still unknown (Silhol et al., 2002). It is also not known whether all these different peptides penetrate into a cell by means of the same mechanism. Early studies showed that uptake mechanisms, such as classical endocytosis, receptor- or transporter-mediated active import, can probably be excluded

(Derossi et al., 1996). The transport also seems to be energy-independent, as it could be observed even at 4 °C (Derossi et al., 1996). On the other hand it was reported that sodium azide-induced inhibition of oxidative phosphorylation could block CPPs translocation (Mitchell et al., 2000). The uptake of CPPs by passive diffusion through the cytoplasmic membrane can also be rejected, because of the highly positively charged nature of these peptides. Recent theories suggested alternative mechanisms for CPPs uptake, based on complex formation of the polycationic peptides with anionic molecules on the cell membrane, such as glycosaminoglycans (Frankel and Pabo, 1988; Sandgren et al., 2002; Tyagi et al., 2001) or lipids (Derossi et al., 1996; Prochiantz, 2000), which would reduce the electrical charge of the peptides and allow the intracellular translocation in some way across the lipid bilayer . Recently, it has also been suggested that the uptake of CPPs is only an artifact caused by chemical cell fixation with paraformaldehyde, which is a widely adopted procedure for epifluorescence microscopic analysis (Lundberg and Johansson, 2001). Skeptical reports (Lundberg and Johansson, 2001) clash therefore with other works that share an optimistic line of thinking and suggest potential applications involving CPPs in pharmacology and biotechnology (Zhao and Weissleder, 2004). As mentioned above, there is hope, that linking CPPs covalently to other molecules could enhance the cellular uptake of these compounds and thus increase the efficiency of drug delivery, improve biotechnological techniques, or provide gene therapy strategies without the employment of viral vectors (Schwarze et al., 2000). However, prior to clinical applications, the import mechanisms and the exclusion of possible toxic effects of CPPs should be clearly ascertained.

The present work focuses on one particular cell penetrating peptide, namely the HIV-1 TAT-PTD. The trans-acting activator of transcription, TAT (Sodroski et al., 1985), is one of the 15 proteins encoded by the human immunodeficiency virus type 1, HIV-1. It is an 86 (or 101 in human blood (Rana and Jeang, 1999)) amino acids long polypeptide specified by a regulatory gene composed of two coding exons. TAT plays an essential role in the upregulation of viral DNA transcription. It acts in the nucleus by binding to a specific viral RNA stem-loop called tat-responsive element (TAR) and to other host cell kinases that enhance the processivity of RNA polymerase II at early elongation steps (Clavel et al., 1986; Karn, 1999). Indeed, in the absence of TAT, the RNA pol II complex interrupts prematurely the transcription after about 100 nucleotides (Laspia et al., 1989).

The TAT sequence can be subdivided into several distinct regions on the basis of its amino acid composition, i.e., a N-terminal activation acidic region (amino acids 1 - 19), a cysteine-rich domain (amino acids 20 - 31), a hydrophobic core region (residues 32 - 47), a basic region (residues 48-57), a glutamine-rich region (residues 60-71), and a RGB motif (residues 72-86). The cysteine-rich fragment plays a role in the activation of the RNA pol II transcription complex, whereas the basic region together with the hydrophobic core are responsible for the binding of TAT to the TAR sequence of viral mRNA (Long and Crothers, 1995; Luo et al., 1993; Weeks et al., 1990).

A number of studies showed that small regions of TAT were able to enter cells within 5 - 10 minutes and to import covalently attached compounds of various nature (Frankel and Pabo, 1988). The minimal amino acid sequence of TAT required for cellular internalization was found to be the sequence of amino acid 47-57 ($H_3N$-YGRKKRRQRRR-$COO^-$) in the basic region, and was called TAT protein transduction domain, TAT-PTD (Ho et al., 2001; Vives et al., 1997).

In a number of studies the potential toxicity of TAT-PTD was tested for cultured cells, by exposing them to different amino acid sequences of the peptide (for variable period of time). For example, residues 31-61 of the TAT peptide (82 amino acid residues) were shown to cause concentration-dependent neurotoxicity (Mabrouk et al., 1991; Nath et al., 1996; Sabatier et al., 1991). However, no neurotoxic effects were observed for the TAT-PTD (residues 48-82) (Fawell et al., 1994). Two other studies investigated the toxicity of TAT-PTD on cell cultures (Hallbrink et al., 2001; Vives et al., 1997). Long (24 hours) exposures of cells to TAT-PTD at concentrations of 20 – 100 μM induced necrosis in 60 % of cells (Vives et al., 1997), whereas no acute toxic effect were observed for short incubation times (≤ 30 minutes).

Considering the biomedical potential of CPPs, and given the controversial aspects summarized above, the interaction of the TAT-PTD was studied in living cells to elucidate the mechanisms of action of TAT-PTD. Recently, thermodynamical analysis have been performed, to prove the interactions between TAT-PTD and three different glycosaminoglycans, e.g., heparan sulphate, heparin, and chondroitin sulphate B, *in vitro* (Ziegler et al., 2003; Ziegler and Seelig, 2004). These studies provided first quantitative data

for the evaluation of the possible uptake mechanisms based on a CPPs–GAGs complex formation.

The aim of the present study was to further characterize the TAT-PTD interaction with *living* cells. For this purpose, a fluorescent derivate of TAT-PTD was employed to study *in vivo* the possible translocation mechanism by confocal laser scanning fluorescence microscopy (CLSM), without taking recourse to fixation techniques. In parallel, several experiments were performed in order to assess the role of the GAG heparan sulfate in the uptake of TATP. Moreover, information on the metabolic activity of cells *in vivo* when exposed to TAT-PTD and heparan sulfate were obtained by means of microphysiometry.

The experiments reported here provided dynamical, morphological and functional information on the interactions of TAT-PTD with mammalian cells that can contribute to an understanding of the behavior of CPPs and their potential for possible future biological and clinical applications.

## 2.2 Theory

### The Confocal Laser Scanning Microscope

The Leica TCS SP confocal microscope is equipped with three lasers for the simultaneous excitation of three different fluorescent wavelenghts and three different detectors. Each detector (photomultipliers) can be independently controlled for gain and offset in order to obtain an optimal image quality. The lasers (power ~ 25 mW) connected to the instrument include an argon laser (488 nm excitation line), a krypton laser ($\lambda_{ex}$ = 568 nm), and a helium neon laser ($\lambda_{ex}$ = 633 nm). These laser allow the collection of fluorescent images in the green range (FITC, GFP), near red range (rhodamine, TRITC, Texas red), and far red range (Cy5). In addition, the lasers can be used to obtain bright field images with differential interference contrast (DIC) optics or phase contrast. The Leica TCS SP, equipped with individual spectrophotometers for up to 4 detection channels eliminating the need for emission filters in the scan head, allows continuous selectable wavelength bands for various fluorescent dyes. Images are first viewed on a Leica DMIRBE inverted microscope equipped with an UV filter set, FITC filter set and a rhodamine filter set. The lasers are interfaced to the microscope via a fiber optic cable. Images are collected through acoustical optical tunable filters (AOTF) which provide a precise control of the laser intensity and can also turn the laser beams on or off at exactly the correct time and place. Attached to the Leica inverted microscope is a multiphoton laser that allows acquisition of fluorescent images in the UV to near red range. The control of data collection and manipulation of the scan parameters can be performed through the Leica TCS SP software running under Windows NT. Images are stored as TIFF files with resolutions ranging from 256 x 256 to 2’048 x 2’048 pixels (Leica Microscopy and Scientific Instruments Group, Heerburg, CH).

## 2.3 Material and Methods

### Cell Line

Mouse embryo fibroblasts, NIH-3T3, were a kind gift of Dr. M.M. Gottesman (NCI, NIH, Bethesda (MD), USA).

### Cell Culture

NIH-3T3 cells were grown in DMEM supplemented with 10% (v/v) fetal bovine serum, 0.3 g/L L-glutamine, 100 units/mL penicillin, and 100 units/mL streptomycin and incubated in standard cell culture conditions, i.e., humidity saturated air supplemented with 5% $CO_2$ and temperature of 37 °C.

### Compounds

Heparan sulfate, sodium salt (fraction I[17], average MW = 14.2 ± 2 kDa; sulfate content of 6.44 %; about 30 sulfated disaccarides units) was purchased from Celsus Laboratories (Cincinnati (OH), USA). Heparinase III and all other compounds of HPLC grade were obtained from Fluka (Buchs, Switzerland).

### Peptide Synthesis

The synthesis of TATP ($H_3N^+$-YGRKKRRQRRR-$COO^-$), g ($H_3N^+$-(βA)GGGG-$COO^-$) and g-TATP ($H_3N^+$-(βA)GGGGYGRKKRRQRRR-$COO^-$) was performed by Dr. André Ziegler on a solid phase resin using an Abimed EPS221 peptide synthesizer (Langenfeld, Germany) (Ziegler and Seelig, 2004). Before removing the resin and the protection groups, the amino terminus of g-TATP and g were covalently linked to fluoresceine isothiocyanate (FITC, F) via a thiourea bond (Ho et al., 2001). The beta-alanine (βA) was required to prevent the loss of the FITC during the subsequent removal of the resin and the protection groups by treatment with trifluoroacetic acid. Peptide purification was performed by preparative high pressure liquid chromatography (HPLC). The masses of TATP (1560.8), g (704.7) and Fg-TATP (2247.5) were determined by electrospray ionization mass spectrometry. Peptide purity (>97%) was assessed by analytical HPLC.

### Determination of Binding Parameters *In Vitro*

The binding of Fg-TATP to heparan sulfate was assessed in vitro by static right-angle light scattering, fluorescence quenching and high-sensitivity isothermal titration calorimetry.

## Buffer

Solutions were prepared in 10 mM TRIS, 100 mM NaCl and pH 7.40. The samples were filtered (0.44 μm) and degassed immediately before use (140 mbar, 8 min).

## Static Right-Angle Light Scattering

Static light scattering at right angle was measured with a Jasco FP 777 fluorimeter (Tokyo, Japan) at a wavelength λ = 350 nm and a temperature of 28 °C, under constant stirring. For light scattering experiments, quartz cuvettes of 3.5 mL volume and a cell length of 1 cm were used. The cells were filled with 2.8 mL of Fg-TAT-PTD solution and 4 μL aliquots of heparan sulfate solution were added at injection intervals of 1 minute. Control experiments were performed by injecting heparan sulfate into buffer, without the peptide.

## Isothermal Titration Calorimetry

The binding process of TAT-PTD to heparan sulfate was measured with high-sensitivity isothermal titration calorimetry, using a Microcal VP-ITC calorimeter (Microcal, Northamton, MA, USA) with a reaction cell volume of $V_{cell}$ = 1.4037 mL. For the unlabeled TAT-PTD, the calorimeter cell contained the heparan sulfate solution at a concentration $C_{HS}^{0}$ ~ 12 μM and aliquots of volume $V_{inj}$ = 10 μL of a concentrated TAT-PTD solution ($C_{p}^{0}$ ~ 800 μM) were injected. With each injection, the total peptide concentration in the calorimeter chamber increased by δC = 5.7 μM. The increase of the total reaction volume was also taken into account for the HS concentration and the correction factor applied was:

$$C_{i,HS} = C_{HS}^{0} \frac{V_{cell}}{(V_{cell} + n_i V_{inj})},$$

where $C_{i,HS}$ is the heparan sulfate concentration after $n_i$ injections. For the peptide solution the corresponding correction factor is:

$$C_{i,p} = C_{p}^{0} n_i \frac{V_{inj}}{(V_{cell} + n_i V_{inj})},$$

where $C_{i,p}$ is the peptide concentration in the calorimeter cell, after $n_i$ injections.

For the fluorescent-labeled Fg-TAT-PTD, a peptide solution of concentrations $C_{p}^{0}$ ~ 70-80 μM was placed into the calorimeter cell and was titrated with glycosaminoglycan solutions of 500 μM.

Control experiments were performed by injecting TAT-PTD and heparan sulfate solutions into pure buffer. The heats of dilution of the control titrations , typically -1 to +1 μcal for heparan sulfate and -10 to -20 μcal for the concentrated TAT-PTD solutions, were subtracted from the heats measured for the binding reactions. All solutions were degassed immediately before use by placing them in a 140 mbar atmosphere, for 8 min.

## Cytosensor Measurements *In Vivo*

The equipment and measurement methods used for microphysiometry experiments using the Cytosensor™ Microphysiomenter were identical to that described in section 1.3 of the present work.

## Confocal Laser Scanning Microscopy *In Vivo*

For CLSM analysis, mouse embryo fibroblasts were directly seeded onto sterile non-coated microscopic cover slips especially inserted into six-well dishes. Cells aliquots were incubated for ~ 48 h in order to reach a confluency of ~ 40-60 % at the time of measurement.

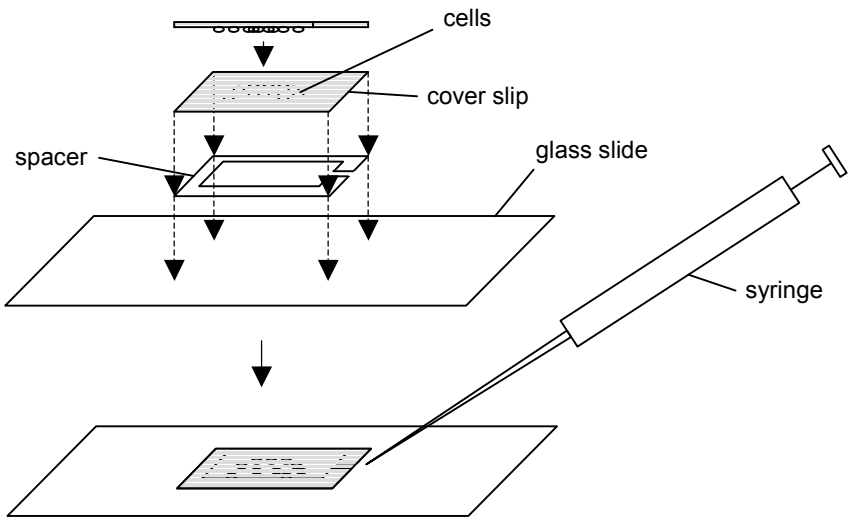


Figure 2.1. *Perfusion chamber for Confocal Laser Scanning Microscopy.* Cells are directly grown as monolayers on uncoated glass cover slips, until 40-60% confluence. For measurements, the cover glass is placed upside down on a microscopic glass slide, separated by an appropriately cut filter paper spacer of 1 mm thickness. The chamber is filled with DMEM to keep cell culture conditions. The construction allows microinjections using a micropipette. In addition, medium flow can be produced by placing an additional filter paper on the side opposite to the aperture of the chamber (not shown on the scheme).

Cell-carrying cover slips were transferred in an up-side-down position on top of a custom-made microscopic perfusion chamber (volume ~ 0.25 mL), allowing image acquisitions and

the injection of labeled peptides, simultaneously (see Figure 2.1). For the experiments, the perfusion chamber was initially filled with DMEM containing the fluorescent peptide, except for kinetic studies, for which the fluorescent peptide (or heparane sulfate) was injected into DMEM at the indicated time (see results). Confocal images were acquired using a Leica TCS-NT-SP1 scanning system mounted on an inverted microscope DMIRBE (Leica Microsystems, Heerbrugg, Switzerland) with a PL APO (planapochromats) datapoints for both lateral dimensions of 250 μm (see section 2.2 for details). Monochromatic Argon laser excitation (488 nm) was used for the excitation of FITC and the recorded fluorescence intensity was plotted using a false-color green scale. Detection with a FITC/TRITC filter (emission bands of 503-533 nm and 582-622 nm, respectively) was used for simultaneous measurements of FITC and propidium iodide.

## 2.4 Results

### Uptake of Fg-TAT-PTD by Mouse Embryo Fibroblasts

The uptake of the fluorescent HIV-1 TAT-PTD peptide by *living* mouse embryo fibroblasts, NIH-3T3, was investigated by confocal laser scanning microscopy and differential interference contrast microscopy. In order to preserve *in vivo* conditions, cells were directly grown in complete cell culture DMEM on sterilized uncoated cover slips and mounted immediately before the observation up-side down on top of a home-made microscopic perfusion chamber of volume V ~ 250 µL (see Figure 2.1).

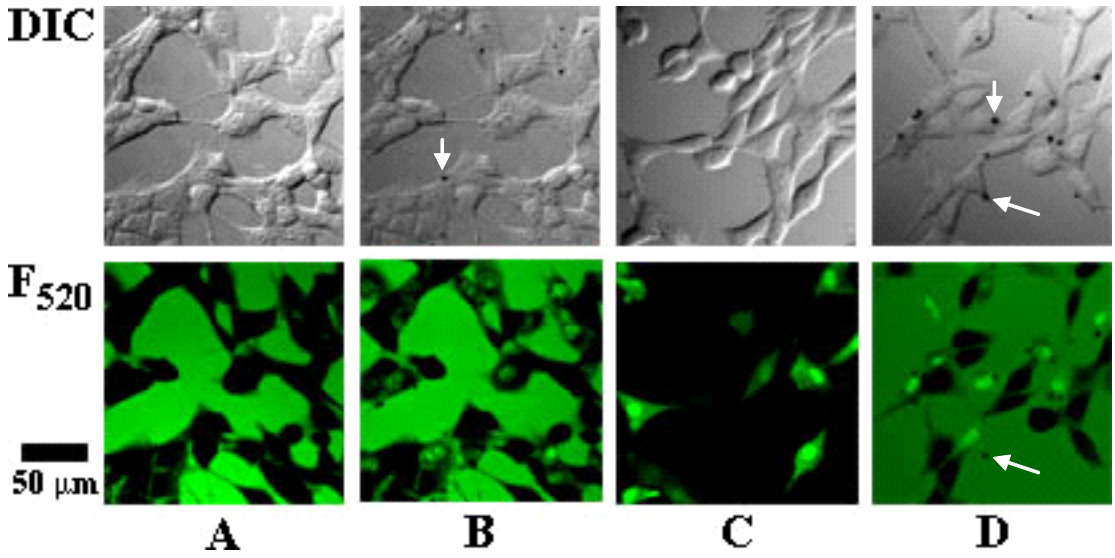


Figure 2.2. *Confocal Laser Scanning Microscopy of Living Mouse Embryo Fibroblasts*. Simultaneous recordings of differential interference contrast images (DIC, upper row, green scale) and fluorescence signal at 520 nm (F520, lower row, false green scale). A) NIH-3T3 cells were grown on uncoated cover slips and mounted upside down on top of a microscopic perfusion chamber filled with 0.25 mL of fluorescent marker peptide, Fg, at 20 µM. Images were recorded 4 min after exposure to Fg. No uptake from the cells. B) 30 µL of 200 µM of Fg-TATP were added to the same fibroblasts, yielding to a concentration of ~ 21 µM of Fg-TATP. Images depict the situation after 4 min from the injection of Fg-TATP. Note the appearance of dark spots (white arrow in DIC) and fluorescent labeling of the nucleus (F520 image). C) Same sample shown in B), 2 minutes later (different field of view), after being rinsed 3 times with 0.5 mL DMEM. The fluorescence in the extracellular space is removed, as well as the dark spots. D) Different fibroblast pool exposed directly to 100 µM Fg-TATP for 4 min. Few dark spots and fluorescent cells are highlighted (white arrows). Bar represent 50 µm.

In a first set of experiments, the perfusion chamber was filled with a solution containing 20 μM of the fluorescent marker peptide Fg. After a 4 minutes incubation, cells were observed under the microscope. As shown in the lower image of figure 2.2A), pronounced fluorescence became visible in the extracellular surroundings. No evident morphological changes of cells occurred and no sign of an uptake of the fluorescent compound could be observed.

In a second step, 30 μL of a 200 μM solution of the fluorescent marker Fg, covalently linked to the HIV-1 TAT-PTD, were administered to the same fibroblasts population, corresponding to a final concentration of ~ 21 μM of Fg-TAT peptide. Figure 2.2B) reports the situation after a 4 minutes contact with the Fg-linked cell penetrating peptide HIV-1 TAT-PTD. Two aspects deserve attention, i.e. i) the appearance of intracellular fluorescence in the F520 image (lower row), and ii) the formation of "dark spots" in the DIC image (highlighted by white arrows in figure 2.2). Further observations (see later in the text) confirm that there is a correspondence between the appearance of the "dark spots" and the uptake of the peptide. Moreover, it is interesting to note that the highest intracellular signal was localized in the nucleus. Figure 2.2C) shows the same fibroblasts population 2 minutes later than in figure 2.2B), after being rinsed 3 times with 0.5 mL of DMEM, to remove the fluorescent compounds from the extracellular space. The difference of the cell distribution is simply due to the snapshot taken in another field of view. Here it is interesting that, after washing, the "dark spots" disappeared, and that the cells labeled with the fluorescent TAT peptide became better distinguishable. The pictures shown in figure 2.2D) illustrate another population of fibroblasts, immersed directly into 100 μM of Fg-TAT peptide, for 4 minutes. The situation is very much analogue to what observed in figure 2.2B) but with more cells labelled per population.

## Dynamical Morphological Considerations – Confocal Microscopy

One advantage of confocal microscopy of intact living cells is the possibility to monitor the cellular incorporation of the fluorescent Fg-TATP with almost real-time (2s-resolution). Indeed, to our knowledge, uptake of CPP was never imaged with such a time resolution. Dynamical recordings were performed by taking serial snapshots images under the confocal microscope, at intervals of 2 seconds, during the administration of 60 μL of a 500 μM solution of fluorescent Fg-TATP stock solution (corresponding to a final concentration $C_{Fg\text{-}TATP}$ ~ 100

μM) to mouse embryo fibroblasts, NIH-3T3. The first appearance of the fluorescent label in the cell nucleus occurs as early as 4 seconds after the exposure of cells to the CPP.

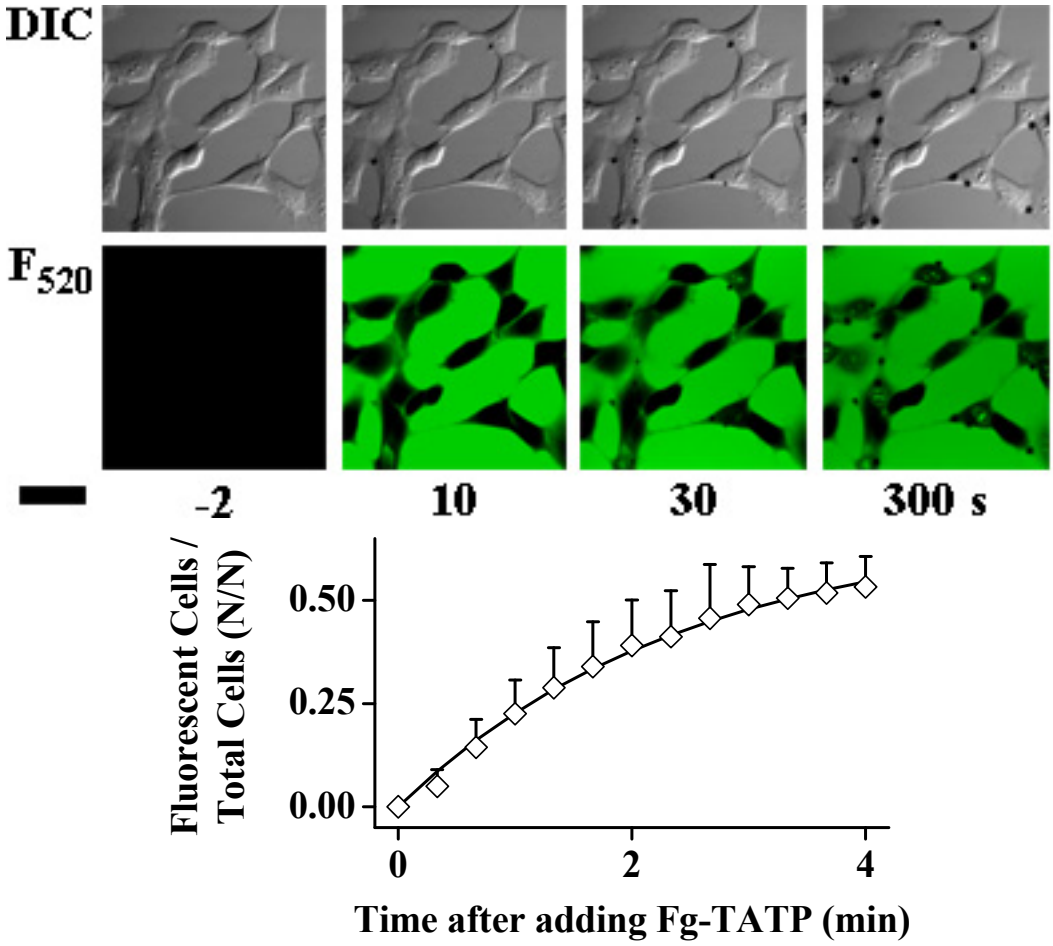


Figure 2.3. *Kinetics of Fg-TAT-PTD uptake from Mouse Embyo Fibroblasts, NIH-3T3*. Dynamical recordings with DIC (gray scale images) and CLS microscopy (520 nm, green images) were performed every 2 seconds. At an instant defined as t = 0 s, 60 μL of a 500 μM Fg-TAT-PTD solution were injected into the 250 μL perfusion chamber, yielding a final concentration of ~ 100 μM Fg-TAT-PTD. For practical reasons, only snapshots at times -2, 10, 30 and 300 seconds are shown. Note the time-dependent increasing size of the dark aggregates in DIC images, and the correspondent appearance of intracellular fluorescence in $F_{520}$ images. The bar represents 50 μm.
*Graph*: dynamics of Fg-TAT-PTD averaged over 11 different fibroblast populations. The number of labeled cells visible in the $F_{520}$ images was divided by the total number of cells seen in the DIC images. The mean ratios obtained are plotted as a function of the exposure time to Fg-TAT-PTD (empty squares). Bars indicate standard deviations (n = 11). A fit of the mean values with a monoexponential function ($f(\%) = 0.68 \cdot (1-e^{(-0.41 \cdot t_{min})})$) is shown (solid line).

The percentage of cells incorporating the peptide increased with time of exposure in an exponential-like way (figure 2.3). However, a relevant fraction of cells (~ 50 % of the total population) did not incorporate Fg-TATP, even after 4 minutes. The time-dependent cellular uptake of the Fg-TATP was fitted for 11 different cell preparations with a monoexponential function , such as

$$Labeled\ Cells\,(\%) = 0.68 \cdot (1 - e^{(-0.41 \cdot t_{\min})}),$$

leading to a half-time of ~ 1.8 min for the uptake of Fg-TAT by the cells, which corresponds to a first-order rate constant k = 0.007 $s^{-1}$ at the particular peptide concentration employed in our measurement ($C_{Fg\text{-}TATP}$ ~ 100 μM) (see graph in figure 2.3).

Another interesting phenomenon observed is the temporal correlation between the incorporation of Fg-TATP and the formation of the "dark spots" on the cell surface. As mentioned above, the spots appeared only on cells that integrated the peptide. Moreover, i) the formation of the spots slightly preceded the intracellular appearance of fluorescence, and ii) the size of the spots increased as a function of the contact time of the fibroblasts with the peptide. As it will be discussed in the next section, the "dark spots" are considered to be molecular aggregates of the peptide and the cellular GAGs.

## Dynamical Functional Considerations – Microphysiometry

We wanted to know whether the metabolism of the cells was affected by incorporation of the Fg-TATP. We exposed mouse embryo fibroblasts, NIH-3T3, to the CPPs and measured the proton extrusion rate with the Cytosensor™ Microphysiometer (Mcconnell et al., 1992).

Extracellular acidification rates (ECAR) of fibroblasts were monitored in real time upon stimulation with increasing concentrations of TAT-PTD, i.e., 5, 50 and 500 μM. As shown in figure 2.4, the ECAR is influenced by the presence of TAT-PTD in a concentration dependent manner. Indeed, a 160 seconds exposure of fibroblasts to TAT-PTD resulted in a rapid decrease of the ECAR, which denotes an apparent slow down of the general cellular metabolism. After switching back to normal DMEM, the original basal ECAR was recovered completely within 2-4 minutes. Figure 2.4 depicts the ECAR alteration upon stimulation with 5 μM (A), 50 μM (B), and 500 μM (C) of TAT-PTD. Three cell populations are displayed,

i.e., a control line stimulated only with normal DMEM (green), and two lines stimulated with TAT-PTD (red and black). No remarkable ECAR decrease was observed in the presence of 5 µM TAT-PTD, However, a 10 % inhibition of the basal ECAR could be obtained upon addition of 50 µM TAT-PTD. In the presence of 500 µM TAT-PTD, fibroblasts reduced their ECAR by 25-40 % (the case reported in figure 2.4C) showed one of the strongest effects). Even at such high concentration, the basal ECAR could be re-stabilized completely in a short time. Repeated stimulations with 500 µM TAT-PTD (n > 4) ) led to a progressive decrease of the basal ECAR and thus to an incomplete recovery (data not shown).

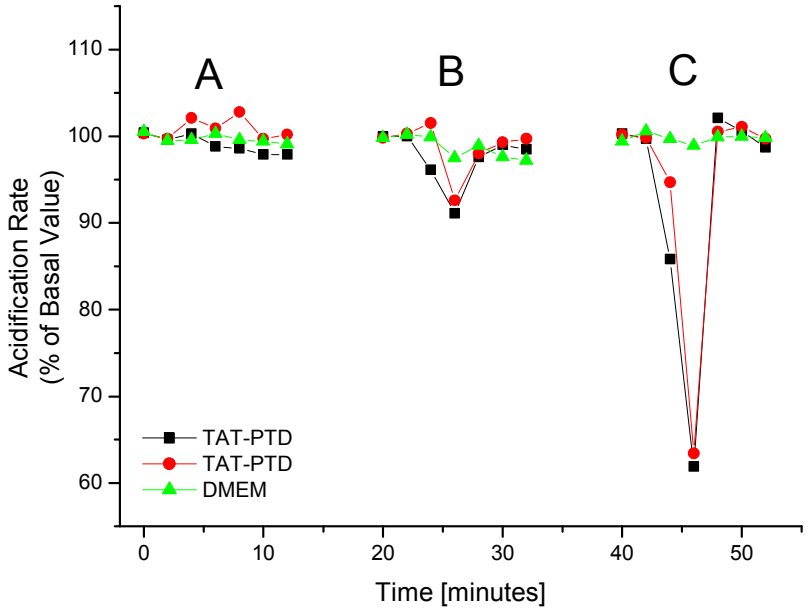


Figure 2.4. *Concentration-Dependent ECAR decrease induced by TAT-PTD.* The effect of TAT-PTD on NIH-3T3 mouse embryo fibroblasts (red and black lines) was tested by microphysiometry at concentrations of A) 5 µM, B) 50 µM and C) 500 µM. Control stimulations with only DMEM are also shown (green line). The extracellular pH change is measured every 2 min, during 20 sec., and expressed in percent of the basal ECAR.

The effects of CPPs on the cellular metabolism could be neutralized by a simultaneous administration of HS. As shown in Figure 2.5B) a co-administration of 500 µM TAT-PTD and 36 µM HS (red and black lines) inhibited the effect of TAT-PTD on the ECAR, completely after 40 seconds stimulation (3d points from left) and slightly after 2'40'' (4$^{th}$ points from left). The effect was even more pronounced by adding 72 µM HS to the TAT-PTD (figure 2.5C)), which completely reversed TAT-PTD induced ECAR decrease after 40 s and reduced the effect of more than 50 % after 2'40''. The behavior of two other cell populations measured simultaneously in different sensor chambers is shown in figure 2.5B) and C) (lines blue and magenta). Here, only HS was added. Exogenous HS alone also caused an ECAR decrease in NIH 3T3 fibroblasts of just 5 -7 % for both concentrations tested ( B) 36 µM and C) 72 µM).

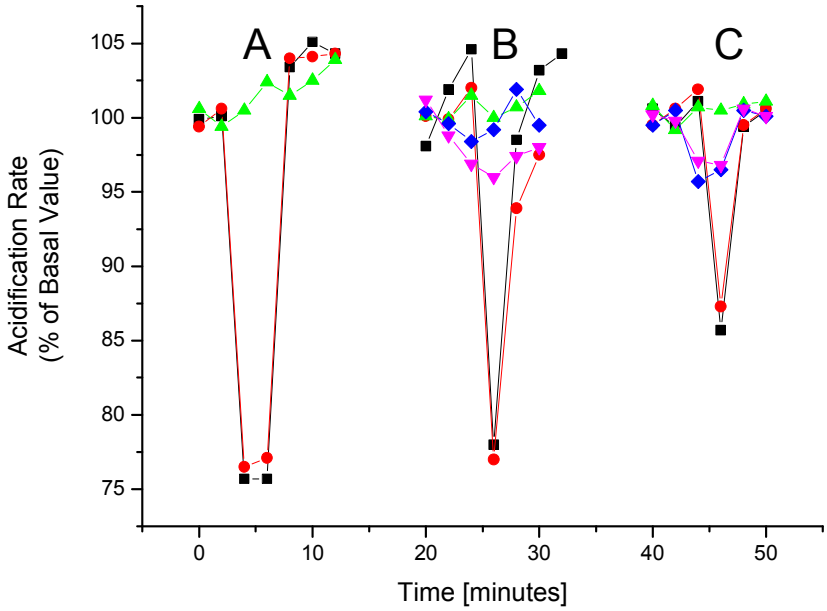


Figure 2.5. *Heparan Sulfate Inhibits TAT-PTD Activity.* Cytosensor™ Microphysiometer recordings of NIH-3T3 mouse embryo fibroblasts extracellular acidification rate. A) cells were stimulated with 500µM TAT-PTD (red, black lines). B) Co-administration of 36 µM heparan sulfate and 500 µM TAT-PTD (red, black) and stimulation with only HS 36 µM (blue, magenta). C) Co-administration of 72 µM HS and 500 µM TAT-PTD (red, black) and stimulation with only 72 µM HS (blue, magenta). Control stimulations with DMEM are shown (green lines).

The effect of the TAT-PTD on the ECAR of 3T3 cells was further investigated by administrating equivalent amounts of amino acids, i.e., lysine, arginine, glycine, glutamine and tyrosine in the monomeric forms. The effect of monomeric aminoacids was significantly lower than that of the TAT-PTD peptide. All results are summarized in figure 2.6.

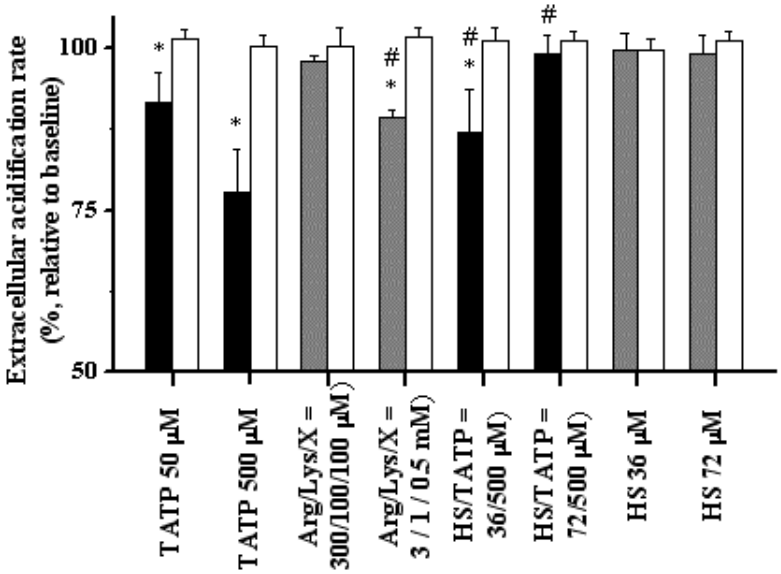


Figure 2.6. *Effect of TAT-PTD, Heparane Sulphate and Monomeric Amino Acids on NIH 3T3 fibroblasts metabolism.* Cells ($5 \cdot 10^5$- $1 \cdot 10^6$) seeded in sensor chambers of a Cytosensor™ Microphysiometer were supplemented with ~ 120 µL/min medium. The extracellular pH was measured every two minutes cycles, during a "pump off" interval of 20 seconds. Selective switch of perfusing medium were performed, to supplement cells for 2 min 40 sec with the different compounds (indicated under the x-axis of the graph). Alteration of the ECAR upon selective stimulations are reported (black and gray bars). The ECAR recovery are depicted (white bars) 2 pump cycles after the end of stimulations, during which cells were supplemented with DMEM. All data are expressed in percent of the basal acidification rate measured before the stimulation. HS, heparan sulphate; TATP, TAT-PTD; X, glycine, glutamine and tyrosine each at 50 or 500 µM. (*, $P < 0.05$ versus baseline; #, $P < 0.05$ versus 500 µM TAT-PTD).

## Heparane Sulfate Induces Fluorescence Quenching and Inhibits Fg-TATP Uptake

We tested the effect of the glycosaminoglycan heparan sulfate on the uptake of Fg-TATP by NIH-3T3 cells. In a similar experimental setup for confocal microscopy as described above, a cell population already in contact with Fg-TATP for 4 minutes (figure 2.7A), upper image), was next exposed to heparan sulfate in a molar ratio of HS/Fg-TATP ~ 0.16.

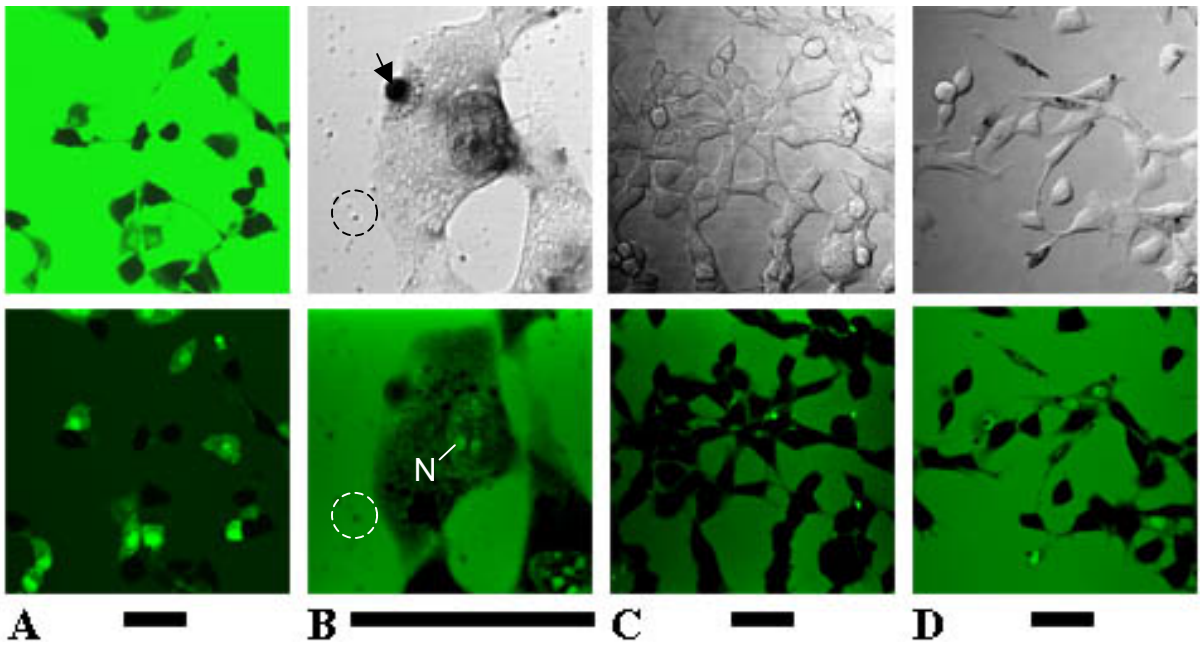


Figure 2.7. *Exogenous Heparan Sulfate and Heparinase III affect Fg-TAT-PTD Uptake.* A) Mouse Embryo Fibroblasts, NIH-3T3, were incubated in a 100 µM Fg-TAT-PTD solution. After 4 minutes, from Fg-TAT-PTD injection, exogenous heparan sulfate, HS, was added, yielding a molar ratio HS/Fg-TAT-PTD of ~ 0.16. CLSM F520 snapshots were recorded before (upper image) and directly after (lower image) HS addition. Note the extracellular fluorescence quench in the presence of HS. B) Magnification of one fibroblast from the preparation shown in A) (lower image). In both DIC (upper) and F520 (lower) images, aggregates of different size are visible on the cell surface (black arrow in DIC) and in the extracellular medium (dashed circles). C) Recordings a new preparation, 4 minutes after *simultaneous* administration of HS/Fg-TAT-PTD at a ratio of ~ 0.16. Intracellular labeling of fibroblasts and aggregates are conspicuously inhibited. D) Fibroblasts were grown 1 hours in the presence of 15 mU heparinase III, then rinsed with DMEM, and exposed for 4 minutes to 100 µM Fg-TAT-PTD. This treatment reduced the uptake of Fg-TAT-PTD. Bars represent 50 µm.

As a result, the fluorescence of the extracellular medium was quenched as shown in the lower image of figure 2.7A) and the preparation became similar to that seen after removal of the extracellular medium by repeated rinse, shown in figure 2.2C), i.e., the contrast of the intracellular versus extracellular fluorescence signal was definitely enhanced.

At a higher magnification (figure 2.7B)), the appearance of tiny aggregates in the free medium was observed (dashed circles), presenting similar optical features than the "dark spots" occurring on the cell surface of labeled fibroblasts.

The effects of heparan sulfate depended, however, on the sequence of its addition with respect to the peptide addition. While injecting HS 4 minutes after the cellular exposure to Fg-TATP had only effects on the extracellular environment, the *simultaneous* addition of HS and Fg-TAT consistently inhibited the uptake of the peptide by the cells, as shown in figure 2.7C). Moreover, the efficiency of the inhibition of peptide uptake depended on the molar ratio of heparan sulfate/Fg-TATP. Indeed, a decrease of the fraction of CPP incorporating cells from 46 % to 6 % was observed by changing the molar ratio heparan sulfate/Fg-TATP from 0/100 to 16/100 (see graph in figure 2.8).

## Heparinase III reduces TATP Uptake

To further test the involvement of heparan sulfate in the binding and uptake process of the HIV1-TAT PTD peptide, we performed confocal microscopy measurements of fibroblasts populations previously treated with 15 mIU of heparinase-III (Suzuki et al., 2002), during 1 hour.

This enzyme is able to degrade the heparan sulfate chains at the low sulfation regions (Linhardt et al., 1990). The fraction of the cell population that integrated the peptide subsequently to the enzymatic treatment was reduced by 32 % as compared to preparations shown in figure 2.7D),

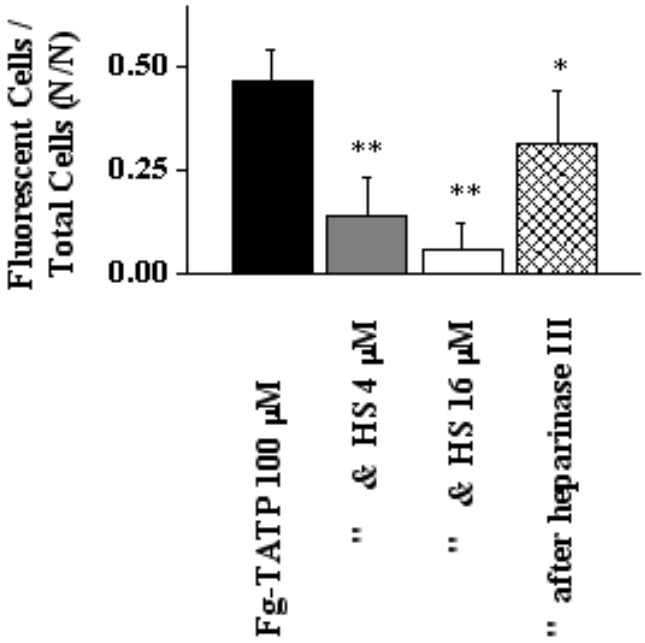


Figure 2.8. *Quantitative analysis of Heparan sulfate- and heparinase III-induced Fg-TAT-PTD uptake inhibition.* NIH-3T3 cells were immersed into 100 µM Fg-TAT-PTD without i) and with ii) 4 µM and iii) 16 µM hepapan sulfate. iv) After 1 hour incubation with heparinase III. The number of fibroblasts that incorporated the peptide (counted in F520 images) was divided by the total number of cells (counted in DIC images). Mean values obtained from 5 different experiments, and 4 different fields of view for each experiment (>150 cells), are depicted in the graph (mean±SD, n=5). $P < 0.05$ (*), and $P < 0.001$ (**) versus the peptide alone.

## In vitro assessment of Binding, Aggregate Formation and Fluorescence Quenching.

The experiments described above showed that the glycosaminoglycan heparan sulfate interacts with the uptake mechanism of TAT-PTD peptide. In order to better define the direct interaction of heparan sulfate with the cell penetrating peptide, *in vitro* analysis have been performed to quantify the binding strength between the two compounds and the efficiency of the fluorescence quenching observed with confocal microscopy.

The thermodynamic parameters of binding were determined by high sensitivity isothermal titration calorimetry and are shown in figure 2.9A).

The binding of heparan sulfate to Fg-TATP, at 28 °C, is exothermic and the reaction enthalpy is $\Delta H^0 = -3.60 \pm 0.23$ kcal per mol of Fg-TATP. The binding constant is $K_0 = (4.6 \pm 1.2) \cdot 10^4$ $M^{-1}$ and is one order of magnitude smaller than what measured in a previous work for a non-fluorescent TATP (Ziegler and Seelig, 2004). The difference between fluorescent and non-fluorescent TATP is probably caused by the hydrophobic fluorescent reporter group.

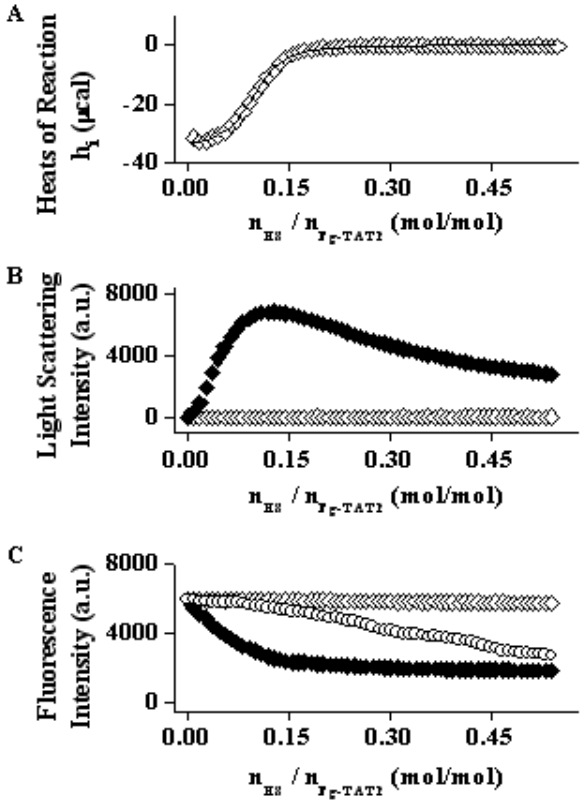


Figure 2.9. *In Vitro Assessment of Fg-TAT-PTD Interactions with Heparan Sulfate. Binding Parameters, Aggregate formation, and Fluorescence Quenching.*. A) The binding of HS to Fg-TAT-PTD was measured by isothermal titration calorimetry (ITC). Data (◇) report the heat release from a titration of 2 μL HS (0.50 mM) aliquots into 78.1 μM Fg-TAT-PTD. Injections were performed every 5 min, at 28 °C. Thermodynamic analysis of the binding isotherm (line) yields a reaction enthalpy $\Delta H^0 = -3.60 \pm 0.23$ kcal/mol of Fg-TAT-PTD, a binding constant $K_0 = (4.6 \pm 1.2) \cdot 10^4$ $M^{-1}$ and n = 6.7 ± 0.4 binding sites (at 28 °C). B) Right-angle light scattering at λ = 450 nm of a titration of 4 μL of 0.10 mM HS (◆) or 4 μL pure buffer (◇) aliquots into a 2.8 mL of a 15.6 μM Fg-TAT-PTD solution, at injection intervals of 1 min and 28 °C temperature. C) Fluorescence quenching in 2.8 mL of 15.6 μM Fg-TAT-PTD at 28 °C, after serial additions of 4 μL aliquots of 100 μM HS (◆), 5.2 mM KI (○), or buffer (◇), respectively. Experiments were performed under constant stirring.

The employed HS has a maximum of 6.7 ± 0.4 independent binding sites for Fg-TATP. A Fg-TATP molecule carries 8 positive charges, which allows a simultaneous interaction with several HS molecules. In a solution containing Fg-TATP and HS, crosslinking is likely to

occur, depending on the molar ratio of the two compounds. A consequence of crosslinking is the formation of aggregates. In our study, the tendency to aggregation was analyzed quantitatively as a function of the molar ratio HS/Fg-TATP, using right-angle light scattering. Figure 2.9B) shows a titration of Fg-TATP with heparan sulfate. The light scattering intensity at 450 nm is reported against the molar ratio HS/Fg-TATP. For the experiment, serial injections of 4 µL of HS 0.10 mM were performed at intervals of 1 min into a 15.6 µM solution of Fg-TATP. As a control, the same amount of pure buffer was injected instead of HS. From the graph in figure 2.9B) it can be observed that a concentration dependent light scattering occurs during the titration of Fg-TATP with HS. The light scattering intensity resulting from HS addition increased almost linearly up to a molar ratio HS/Fg-TATP = 0.16 ± 0.02 (solid squares). For higher concentrations of HS, the scattering intensity decreased again. Differently, the control titration using pure buffer showed no significant light scattering (empty squares).

In a similar experiment, the fluorescence intensity of Fg-TATP was measured during a titration of the latter compound with HS. Figure 2.9C) shows the occurrence of fluorescence quenching of Fg-TATP upon addition of HS *in vitro*, at 28 °C, under constant stirring. Fluorescence intensity decreased during the serial injection of 4 µL aliquots of a 100 µM HS solution and reached a plateau for a HS/Fg-TATP molar ratio = 0.14, which corresponds virtually to a complete binding of the peptide (as shown by ITC, figure 2.9A)). Further addition of heparan sulfate had no longer significant effect on the fluorescence signal. This suggests that the presence of negative charges (HS) had a higher effect on the fluorescence quenching than the aggregation which disappeared after this equivalence point. As a comparison, the same experiment was performed by titrating Fg-TATP with 4 µL aliquots of potassium iodide, KI, 5.2 mM (figure 2.9C), empty circles), a commonly used salt for quenching the fluorescent signal of fluorescent proteins in a non-denaturing manner. Figure 2.9C) shows clearly that the fluorescence quenching of HS was more efficient than an addition of 0.4 M potassium iodide. As a control, the same titration was performed with equivalent amounts of pure buffer (figure 2.9C), empty squares). No consistent reduction of the fluorescence intensity was observed in this case.

## Assessment of Membrane Integrity

In order to determine whether the intracellular inclusion of Fg-TAT-PTD was related to an impairment of the cytoplasmic membrane of cultured fibroblasts and handling under the microscope, we performed a test to assess membrane integrity. A compound known to be unable to cross an intact lipid bilayer, namely propidium iodide, was taken for this purpose (fluorescence at $\lambda$ = 617 nm). Cells were kept in the presence of 33 µM propidium iodide for 4 minutes and then, after appropriate rinse with DMEM, analyzed by confocal microscopy by laser scanning at 617 nm. As shown in figure 2.10A), a small portion of cells were leaky (2 cells visible in the field of view). Directly thereafter, ~ 100 µM Fg-TAT-PTD were injected in the perfusion chamber containing the same cell population. Four minutes later, the snapshot shown in figure 2.10B) was recorded at 520 nm. No correlation could be observed between Fg-TAT-PTD and a lack of membrane integrity. Indeed, from a comparison of figure 2.10A) and B), one can easily see that several intact cells not labeled with propidium iodide were able to integrate Fg-TAT-PTD.

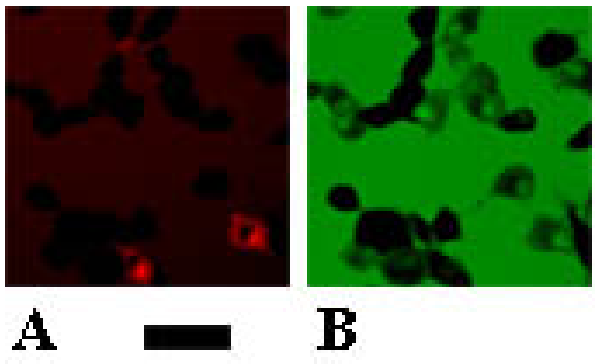


Figure 2.10. *Assessment of Membrane Integrity in cultured NIH3T3 Mouse Fibroblasts*. The correlation of TAT-PTD uptake and possible damage of the cytoplasmic membrane was investigated. A) Mouse embryo fibroblasts were incubated for 4 minutes with 33 µM propidium iodide, a compound incapable of crossing an intact cytoplasmic membrane. Two minutes later, after washing twice with DMEM, cells were observed under a CLS microscope at $\lambda$ = 617 nm. Two cells show incorporation of the dye (red signal). B) The same cells were then exposed to ~ 100 µM Fg-TAT-PTD. The image was recorded at $\lambda$ = 520 nm, 4 minutes from the injection of Fg-TAT-PTD. There is no relation between Fg-TAT-PTD and propidium iodide incorporation. Bar corresponds to 50 µm.

## Notes on an Interesting Observation

The microliters-injection of Fg-TATP into the microscopic chamber used for confocal microscopy measurements requires particular attention. For example, air bubbles have to be carefully avoided. Indeed, a small air bubble between two close glass slides can have a dramatic effect on the cells grown on the microscopic cover slip. Figure 2.11 shows the passage of an air bubble over cultured fibroblasts, NIH-3T3, placed in the space of the perfusion chamber, between the two glass slides separated by the spacer of 1 mm (see figure 2.1, in section 2.3).

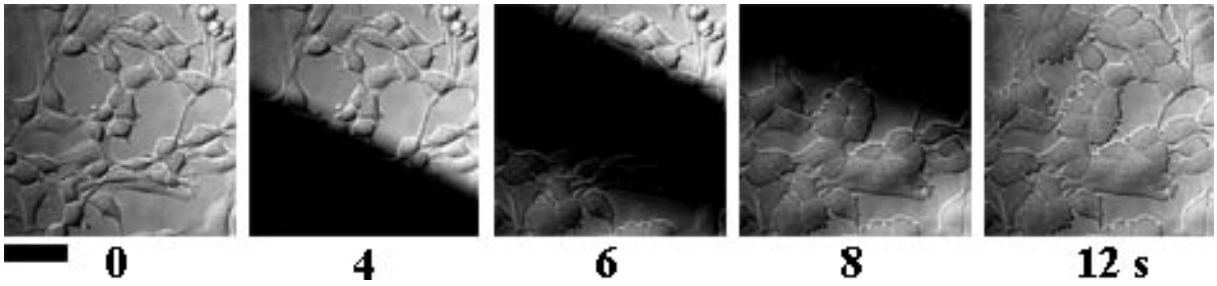


Figure 2.11. *Effect of an Air Bubble-Induced Hydrostatic Pressure on Fibroblasts Monolayers in Microscopic Preparations.* The perfusion chamber used for CLSM analysis, limited by two glass slides separated by ~ 1 mm, was filled with DMEM. The figures sequence shows the effect of the passage of an air bubble over mouse embryo fibroblasts, NIH-3T3, in the chamber. The dark shadow in the images taken at time t = 4, 6, 8 seconds is the migration front of the bubble. As a consequence of this, the cells were squeezed against the glass slide resulting in a drastically different, budding-like form (visible in images at t = 6, 8, and 12 s). This artifact is not observable by simple contact with air and it is distinctly different from the other observations in DIC microscopy, i.e., aggregates formation and Fg-TAT uptake. Bar corresponds to 50 μm.

The front of the air bubble can be easily recognized by the large black front moving, in a few seconds, from the left lower to the right upper corner in the DIC images. The hydrostatic pressure created by the air bubble between the slides is apparently high enough to squeeze the cells. As a result, the fibroblasts assume a completely deformed shape, characterized by a pronounced budding of the cell membrane. This feature is distinctly different from the dark aggregates produced by Fg-TATP administration, described above. This bubbling effect is most pronounced for cells lifted from the glass plate, a situation that occurs periodically during the normal cell cycle of adherent cells in cell culture. In contrast, fibroblasts that are well spread on the slide, are less morphologically affected by the bubble-induced hydrostatic pressure. Indeed, the simple exposure of cells to air, or even artificial drying on a single glass plate does not produce a similar effect.

## 2.5 Discussion

The biological mechanism of cell penetrating peptides is quite controversial, and not understood. The aim of the present work was to provide a better understanding of the interaction of a particular CPP, HIV1-Fg-TAT-PTD, with living mouse embryo fibroblasts, NIH-3T3, the cell line chosen as model for our experiments.

### Advantages of Confocal versus Epifluorescence Microscopy

The special feature of the present investigation was the use of confocal microscopy, which allowed a distinction between intracellular and extracellular fluorescence, without the need to remove the fluorescent peptide from the extracellular medium or without the need of chemical cell fixation. The spatial resolution was sufficient to identify the intracellular label: as shown in figure 2.2B), the number of cells that presented Fg-TAT uptake in unwashed preparations was not different from that after the removal of extracellular dye (figure 2.2C)). A rinse with DMEM is however of some usefulness to the improvement of the image contrast.

A good distinction between intracellular and extracellular fluorescent signal in a microscopic preparation *in vivo* is only possible because of the confocal nature of the images. In the measurements reported here, the sampled image plane thickness was 0.5 μm, and was the same for the intracellular and extracellular peptide. In contrast, the conventional epifluorescence microscopy used in many earlier studies on TATP recorded the fluorescent signal from a larger sample thickness. Under such conditions, where the sample depth is usually 0.1 - 1 mm, the large amount of fluorescent dye in the extracellular layers above the cells is much more abundant than that at the interior of the cells, which have an axial depth in the order of ~ 10 μm. In conventional fluorescence microscopy, removal of the extracellular Fg-TATP and fixation of cells is a prerequisite for the detection of intracellular signal coming from Fg-TATP, thus excluding the possibility to observe the uptake phenomenon and to record kinetical data in *living* cells.

## The Uptake of CPP is Not an Artifact of Fixation

The present experiments clearly exclude the possibility that the uptake of CPP is due to an artifact occurring during cell fixation with paraformaldehyde or methanol (Lundberg and Johansson, 2001),, a procedure currently done for analysis with epifluorescence microscopy. The uptake of Fg-TATP showed in figure 2.2B-D is, to our knowledge, the first report of this phenomenon in intact, non fixated and *living* cells. As such, this observation supports more than 40 previously published studies on *chemically fixated* cells (see (Schwarze et al., 2000) for a review). The main critic to those studies published in the past was the potential damage of the cell membrane upon chemical fixation which could lead to an increased membrane permeability (Lundberg and Johansson, 2001). In the present work, any chemical fixation was avoided and physiological osmotic conditions were respected. Under these conditions, mouse embryo fibroblasts, NIH-3T3, incorporated the peptide Fg-TATP within a very short time, i.e., already after a few seconds, and definitely after 4 minutes. Therefore, the present results show that the uptake of Fg-TATP is not an artifact of cell fixation (Lundberg and Johansson, 2001). Moreover, the control experiment reported in figure 2.2A) illustrates that i) the Fg marker dye alone is not able to penetrate into the fibroblasts, and that ii) the cell membranes were intact before the administration of the fluorescent dye. As shown in Figure 2.10, the integrity of the cell membrane was further tested by incubating cells with propidium iodide, a commonly used marker to assess plasma membrane integrity. Here, only a few damaged cells were present in the preparation (which is a normal fraction of cells grown in culture) as evidenced by confocal microscopy at 617 nm, the wavelength of propidium iodide fluorescence. However, healthy cells that resisted the uptake of propidium iodide, were able to incorporate Fg-TATP. This integrity of the cytoplasmic membrane of fibroblasts before the exposure to Fg-TATP cannot support a recent report where only cells with flawed membranes showed accumulation of TAT (Kramer and Wunderli-Allenspach, 2003).

## Morphological Alterations occur on The Cytoplasmic Membrane upon TAT-PTD Exposure

Exposure of mouse embryo fibroblasts, NIH-3T3, to the cell penetrating peptide Fg-TAT leads to the appearance of “dark spots” on the cell surface, as shown in figure 2.2D). In general, there was only one spot per cell, sometimes two. The specific characteristics of the DIC (Nomarski, 1955) suggests that such dark spots are actually dense aggregates on the cell membrane of fibroblasts. It is interesting to note that the aggregates appeared only on the cells that integrated the fluorescent Fg-TATP. This aggregate formation was not reported in

previous studies, most probably due to the fixation procedures. Indeed, the aggregates could be removed by rinsing the cells 2-3 times with DMEM. Another reason could be the specific heparan sulfate/peptide ratio that is needed for aggregate formation (see figure 2.9B)).

However, the aggregate formation observed *in vivo* is in excellent agreement with observations reported in a recent study *in vitro* (Ziegler and Seelig, 2004). The formation of aggregates was observed between the heparan sulfate and the non-fluorescent peptide HIV1 TAT-PTD. Moreover, it was found that the size of the aggregates was dependent on the molar ratio and the order of mixing of the two compounds (the aggregates are larger, if the peptide is first in the tube/excess - this way a single HS added will cross-link several peptides).

In analogy to these *in vitro* observations, the results obtained from the experiments *in vivo* suggested that the dark aggregates shown in figure 2.2 could result from the binding of Fg-TATP to heparan sulfate or other type of glycosaminoglycans present on the plasma membrane of the fibroblasts. This hypothesis was tested by adding exogenous heparan sulfate to cells, after their exposure to the fluorescent peptide. As shown in figure 2.7B), the presence of free HS resulted in an additional formation of aggregates in the extracellular medium, previously limited to the cell plasma membrane only confirming that mixing Fg-TATP to HS also produces aggregates. It is important to point out that the free aggregates and those anchored to the cell membrane had the same image contrast in DIC microscopy. A major difference was the size. The aggregates found in the extracellular space had a diameter < 1 μm, whereas those present on the cell surface were distinctly bigger, with a diameter < 5 μm. This may be due to different molar ratios of the compounds used, the time of exposure of the cells to the Fg-TATP (see dynamical observations) and differences in the chemical nature of the glycosaminoglycans involved in the reaction. Indeed, the exogenous heparan sulfate added consisted of a fraction of HS with a low molecular weight (average MW ~ 14'200), whereas heparan sulfate chains extracted from cellular proteoglycans of fibroblasts have molecular weights in the order of ~ 45'000 (Turnbull and Gallagher, 1991).

## Dynamics of Fg-TAT-PTD Incorporation by Fibroblasts

In the present work, it has been shown that the Fg-TATP is taken up by living mouse embryo fibroblasts, NIH-3T3, in a very short time. Indeed, fluorescent labeling of the nucleus

occurred already 4 seconds after the exposure to the peptide. Interestingly, and as already reported in previous works (Frankel and Pabo, 1988; Green et al., 1988; Hallbrink et al., 2001), around 50 % of cells did not incorporate the Fg-TATP. The reason for this difference remains unclear yet. It could be speculated that this is due to a differential expression of glycosaminoglycans on the cell surface, at different steps of the cell cycle. The rate constant for the velocity of labeling of the cell population, calculated from our results as $k = 0.007/s$ is also in agreement with what reported in other studies (Frankel and Pabo, 1988; Green et al., 1988). However the uptake in the experiments reported here was faster than that obtained from studies based on a cell-coulter assay using a fluorescence quenching test, where a first-order rate constant for TATP uptake was estimated around 0.0003/s (Hallbrink et al., 2001). Such differences could be attributed to experimental conditions chosen for the investigation and also to the cell strain employed.

The temporal resolution obtained in our experiments allowed observations of the growth of the aggregates of Fg-TATP on the cell membrane. The aggregates preceded the appearance of the intracellular fluorescence by some seconds, and increased in size as a function of the contact time (afer 4 min up to ~ 5 μm). This phenomenon could suggest the hypothesis of an initial homogeneous distribution of glycosaminoglycans on the cell membrane, which could be consecutively recruited to a particular region of the cell, with a particularly favorable electrostatic environment for the binding of polycationic compounds like TATP.

The accumulation of large aggregates on the cell membrane displays certainly an unphysiological condition and, as such, may be toxic for the cells. This is supported by previous reports. A 24 hours exposure of HeLa cells to similar concentrations of TATP as employed here was shown to induce cell necrosis in 60 % of the cells.

## Inhibition of Fg-TATP Uptake by Heparan Sulfate

The Inhibition of Fg-TATP Uptake by heparan sulfate is a further indication of the role of cellular glycosaminoglycans such as heparan sulfate for CPP uptake. The inhibition of Fg-TATP uptake by the addition of exogenous HS is, however, not unique. In a previous work, the cellular uptake of cationic polylysine could be inhibited by a simultaneous administration

of exogenous heparin (Morad et al., 1984), an intracellular compound of similar structure than extracellular heparan sulfate.

### Fluorescence Quenching by Heparan Sulfate

The fluorescent signal was an important parameter for the qualitative evaluation of the measurements. However, the intensity of confocal images depends on a variety of parameters and therefore it cannot be exploited for a quantitative evaluation of the Fg-TATP concentration in the cells or in the extracellular space: A possible binding to cellular compounds, such as heparan sulfate, could lead to fluorescence quenching and thus distort the analysis.

### Enzymatic Removal of HS results in a Decrease of TATP Uptake.

Further evidence that the recognition of Fg-TATP by cells occurs through a interaction with glycosaminoglycans was provided by the experiments shown in figure 2.7D). In these experiments, cells were treated with heparinase III prior to the administration of Fg-TAT. Under these conditions, a decrease in the number of labeled fibroblasts by ~ 30 % was observed. The fact, that the inhibition upon enzymatic digestion was not complete, suggests that other similar membrane polysaccharides, such as chondroitin sulfate, could be involved in the recognition process or that heparinase treatments cannot achieve a total removal of the glycosaminoglycans, for example because of sterical hinderance (Schulz et al., 1998).

The role of glycosaminoglycans for the uptake of CPP is still a matter of debate. One of the first studies on TAT uptake (Mann and Frankel, 1991) proposed that the absorption of TAT proceeded via non-specific endocytosis, and that glycosaminoglycans were not involved in the uptake, because heparinase treatment could not inhibit TAT uptake completely (in analogy to the present experiments). Alternative uptake mechanisms were proposed by other groups (Derossi et al., 1996; Prochiantz, 2000) such as lipid binding. However, an increasing number of studies is now supporting the idea that TAT uptake proceeds through a specific binding to heparan sulfate (Belting, 2003; Rusnati et al., 1997; Sandgren et al., 2002; Tyagi et al., 2001). The findings of the present work are also in favor of the hypothesis of specific binding to HS.

## TAT can alter Cellular Physiology

Only a few studies investigated the toxicity of TAT-PTD. In one work, it was observed that 100 μM of TAT-PTD induced necrosis in 60 % of cells after a 24 hours exposure time. However, no acute toxic effects were observed for exposure times < 30 min (Vives et al., 1997). Observations made in the present work by microphysiometry, clearly show that TAT-PTD was able to decrease the overall cellular metabolism of mouse embryo fibroblasts, NIH-3T3. This phenomenon is an indicator of some cytotoxicity. However, the acute cytotoxic effect could be rapidly reversed when the peptide was removed from the culture medium. On the other hand, repeated exposures to high concentrations of TAT-PTD produced irreversible cell changes, decreasing permanently their basal ECAR. Combining CLSM and Cytosensor observations, one can conclude that the adsorption of TAT-PTD onto the plasma membrane results in a decrease of the metabolic activity. The molecular nature of this process remains unknown and could be a blocking of ion channels by aggregate formation, a transient membrane structure distortion (resulting in a general malfunctioning of membrane related energy-driven processes), or other mechanisms.

Another interesting correlation can be made between CLSM imaging with the fluorescent TAT-PTD analogue and functional microphysiometry obtained with TAT-PTD. The presence of the glycosaminoglycan heparan sulfate could inhibit both the Fg-TAT-PTD uptake in the image experiments and the decrease of the TAT-PTD-induced extracellular acidification rate. These observations point again towards an interaction of TAT-PTD with cells associated GAGs because a competitive inhibition occurs between exogenous HS and the putative binding partners of TAT-PTD on the cells membrane.

The toxicity of TAT-PTD is a property of the polypeptide only. Adding of the individual amino acids in their monomeric form and at concentrations employed for TAT-PTD does not produce any decreases in the ECAR. This suggests that cross-linking of TAT-PTD with the negatively charged binding partners is necessary for the internalization process, as well as for the ECAR alteration. It is also noteworthy that some amino acid sequences can act as key signals, for example for the entry into the cellular nucleus (Weis, 2003). As seen in CLSM, the nuclear internalization of Fg-TAT-PTD occurred also within seconds.

The observation of the fast intracellular labelling of fibroblasts with Fg-TAT-PTD, in particular the fast concentration of the dye inside the nucleus, may also explain the slow-

acting toxicity of this peptide. Indeed, compounds with high DNA affinity, such as ethidium bromide, are well known for their mutagenic activity. Because of its large positive charges, TAT-PTD may bind very efficiently to the negatively charged nuclear DNA. Therefore, a mutagenic activity of TAT-PTD could be possible.

## 2.6 Conclusion

### Mechanism of TAT-PTD Cellular Uptake

The aim of the present study was to investigate the mechanism(s) of the incorporation of HIV1 TAT-PTD into living cells. To this purpose, *in vivo* confocal microscopy and microphysiometry experiments were performed, extended by *in vitro* observations using isothermal titration calorimetry, right-angle light scattering and fluorescence quenching tests. Specifically we aimed at testing whether (i) cellular glycosaminoglycans could be involved in the CPP uptake, and ii) whether CPP incorporation is an artifact of cell fixations.

In the present work the second point could be excluded by performing measurements *in vivo*, avoiding chemical fixation. An uptake of fluorescent FITC-labeled HIV1-TATP derivate was clearly observed under *in vivo* conditions. In particular, the uptake of the fluorescent TAT-PTD occurred within a few seconds from the time of administration. The appearance of the intracellular labeling was preceded by the formation of dense aggregates, exclusively associated with the cell surface of labeled cells. Neither aggregate formation nor intracellular fluorescence were observed for cells incubated only with the Fg-marker, indicating the specific role of the TATP fragment for transport through the membrane.

The involvement of GAGs was tested to identify the nature of the observed dense aggregates. Co-administration of exogenous heparan sulfate with the peptide inhibited both the incorporation of TAT-PTD and the formation of aggregates. Moreover, heparan sulfate induced fluorescence quenching of Fg-TATP and the formation of aggregates in the extracellular medium. These aggregates had similar optical features than those observed on the cell membrane of fibroblasts. The same effects could be reproduced *in vitro* (isolated systems of heparan sulfate and Fg-TATP).

The enzymatic removal of heparan sulfate GAGs from the fibroblasts led to similar results, i.e., the inhibition of aggregate formation and TATP uptake.

To test cellular function, microphysiometry was employed and confirmed an activity of TATP on mouse embryo fibroblasts (NIH-3T3) on a similar time scale as observed with confocal microscopy. An exposure to the CPP resulted in a rapid, concentration-dependent decrease of the extracellular acidification rate (ECAR) of the fibroblasts. The decrease of the ECAR could be inhibited by a simultaneous administration of exogenous heparan sulfate. However, the ECAR decrease could not be mimicked by an equivalent concentrations of the same amino acids added as monomers.

Ryser, in his work published in 1968 (Ryser, 1968), stressed already the difference between *adsorption* and *uptake*. In our study, these two concepts could be translated into A) "aggregate formation" and B) "fluorescent label internalization". B) is most probably the consequence of A), and A) seems to require the presence of the GAG heparan sulfate in order to occur. These findings, in agreement with others (Tyagi et al., 2001), suggest that also the internalization of HIV-1 requires an adsorption at the cell surface with heparan sulfate or similar proteoglycans of the glycocalix. The aggregates observed in the present work are new findings for this particular CPP. However, a similar phenomenon has been reported in the past for specific antibodies against heparan sulfate (Martinho et al., 1996) and its proteoglycan syndecan-1 (Carey et al., 1994). Such antibodies induced aggregates on cells and enhanced the cellular uptake, including the transfer to the cell nucleus (Ishihara et al., 1986). Importantly, this phenomenon was also observed at 4 °C (Martinho et al., 1996) and is therefore in surprisingly close analogy to the reported, temperature-independence of the TAT uptake (Vives et al., 1997) and polylysine uptake (Ryser, 1968).

While the adsorptive process of TATP seems to be confirmed with these experiments, it could not be answered how the subsequent internalization mechanism proceeds. It could be a new type of transport that include a rapid translocation to the nucleus, or a more classical adsorptive endocytosis. However, inverted micelle formation with lipids (Derossi et al., 1996; Prochiantz, 2000) appears to be very unlikely.

Therefore, the evident adsorption reported in this work strengthens the hypothesis of endocytosis as a likely mechanism for the uptake of CPPs. Adsorptive endocytosis should

involve the formation of endosomes, which were seen in fixated cells (Console et al., 2003), but could not be observed with the techniques employed in the present study.

Finally, as seen in microphysiometry experiments, the potential toxicity of CPP should be seriously taken into account and caution should be used before the formulation of attractive clinical methods for the improvement of drug delivery and gene therapies involving these CPPs.

# Part Three: Functional Magnetic Resonance Imaging of the Mouse Brain

## General Introduction

Functional magnetic resonance (fMRI) is one of the most modern imaging applications based on nuclear magnetic resonance (NMR). It is not the aim of this work to present the theory of NMR in general, as this is extensively reported in textbooks (Levitt, 2001). In order to outline the complexity of the experiments performed in the present project it is, however, necessary to shortly review the historical steps leading to the fMRI development both from the technical as well as from the biological point of view.

The discovery of NMR, reported for the first time in 1946 (Bloch, 1946; Bloch et al., 1946; Bloch et al., 1946; Purcell et al., 1946), awarded Edward Purcell and Felix Bloch with the Nobel Prize in Physics 1952. Twenty-five years later the first NMR experiment on living organisms was performed by Raymond Damadian (Damadian, 1971). In this experiment, Damadian found that the relaxation times of malignant tumors differed significantly from those of normal tissues, suggesting the potential use of $^{1}$H-NMR for clinical diagnostics. In the same period, Moon and Richards (Moon and Richards, 1973) showed how the intracellular pH could be determined in intact erythrocytes by chemical shift differences using high-resolution $^{31}$P-NMR spectroscopy.

Between 1973 and 1974, Lauterbur (Lauterbur, 1973) and Mansfield (Garroway et al., 1974) described the first NMR imaging experiment (or MRI, for Magnetic Resonance Imaging). This technique involved the superposition of position-dependent magnetic fields gradients to the static magnetic field, which allowed the reconstruction of the spatial distribution of spins in the form of an image. Further improvements of planar imaging techniques, included the 2-dimensional Fourier imaging technique (2DFT), introduced in 1975 by Kumar, Welti and Ernst (Kumar et al., 1975; Kumar et al., 1975). Pulsed NMR in combination with Fourier Transform represents nowadays the heart of modern NMR experiments. The achievements of Richard Ernst in pulsed Fourier Transform NMR and MRI were acknowledged with the Nobel Prize in Chemistry 1991. The Nobel laureates in medicine were awarded to Mansfield and Lauterbur just recently (2003).

In 1977, Damadian demonstrated MRI of the whole body. In the same year, Peter Mansfield developed the echo-planar imaging (EPI) (Mansfield, 1977; Mansfield and Maudsley, 1977; Mansfield and Maudsley, 1977), a technique that allowed NMR imaging at video rates (30 ms / image).

In 1980, Edelstein and coworkers adapted Ernst's technique to the imaging of the body (Edelstein et al., 1980; Edelstein et al., 1980; Hutchison et al., 1980). At this time, the temporal resolution of image acquisition was in the order of five minutes. By 1986, the imaging time could be reduced to about five seconds mainly as a result of stronger magnetic fields (no longer need for averaging) and faster switching gradients (for the use of EPI).

Since then, improvement of technical aspects, e.g. superconducting technologies, allowed the construction of scanners with higher and more homogeneous magnetic fields. In 1987 echo-planar sequences could be used to image a single cardiac cycle in real-time (Chapman et al., 1987). In the same year Charles Dumoulin was perfecting magnetic resonance angiography (MRA), which allowed imaging of flowing blood without the use of contrast agents (Dumoulin et al., 1987; Dumoulin et al., 1987; Wood et al., 1987).

Functional MRI (fMRI) was developed in 1993 and included the use of Gadolinium (however, the effect of Gadolinium as contrast agent for MRI was already found in 1988 (Villringer et al., 1988)). Functional MRI allows the mapping of activated regions of a living organism in response to a neuronal excitation. In neurosciences the development of fMRI opened up a new non-invasive way to map the activated brain regions responsible for cognitive and motor processes.

In parallel, other imaging techniques were developed. In 1994, researchers at the State University of New York at Stony Brook and Princeton University developed MRI of hyperpolarized 129Xe gas for lung imaging (Albert et al., 1994). Lung imaging is a challenge because the thin alveoli have many air-to-tissue interfaces so that the local magnetic field is disturbed (susceptibility differences) resulting in non-coherent spins for MRI. Nowadays, NMR spectroscopy and MRI are world-wide used techniques, which find applications from routine clinical diagnostic and surgery (open scanners), to basic science solid-state spectroscopy, and cognitive sciences.

# Chapter 3. fMRI of the Murine Brain

## 3.1 Introduction

Functional MRI finds its main application in brain research and neurocognitive studies using fMRI have rapidly increased in the last few years. The technique is based on the finding, that tissue activation causes changes of blood flow (hemodynamic modulations) and oxygen consumption. Various phenomena based on hemodynamic modulations of activated brain regions are exploited for fMRI acquisitions: i) blood-oxygenation level dependent (BOLD) effect (Ogawa et al., 1992), ii) arterial spin labeling (ASL) techniques, based on $T_1$ in cerebral blood flow (CBF) (Kwong et al., 1992), and iii) relative cerebral blood volume differences (rCBV) (Belliveau et al., 1991; Belliveau et al., 1990). The latter method, also called bolus technique, requires the use of intravascular contrast agents that alter the magnetic susceptibility of the microscopic vessels.

The promise of fMRI for mapping brain function extends also to animal models and thus has the potential to link fundamental and clinical research. The first application of fMRI to animal models goes back to Hyder and coworkers (Hyder et al., 1994) who could localize with BOLD contrast an activated volume of brain tissue in chloralose-anaesthetized rats during electrical stimulation of the forepaw. A similar experiment in rats highlighted the correlation between BOLD response and the frequency of electrical peripheral stimulation (Gyngell et al., 1996). These studies, together with T2*-weighted imaging (Brinker et al., 1999), provided evidence that the hemodynamic signal observed with fMRI is tightly coupled to the neural electrical activity in the activated brain areas. This correlation is called *neurovascular coupling*.

As a result, fMRI in rat models has been extended to study cerebral tissue pathologies. Functional alterations upon pharmacological stimulation with the $GABA_A$ antagonist bicuculline could be observed in cases of ischemic seizures (Dijkhuizen et al., 2000; Hoehn et al., 2001; Reese et al., 2000). These findings highlighted the potential of fMRI for pre-clinical research. It is a non-invasive imaging modality able to provide functional, i.e. physiological, readouts for the assessment of brain function even in the absence of structural evidences for tissue impairment (see (Rudin et al., 1999) for review).

Other contrast methods, based on $T_1$ (ASL) or $T_2$ (CBV) weighted imaging, have been tested in fMRI preclinical studies on animals (see (Beckmann et al., 2001) for review), both during electrical (Kerskens et al., 1996; Silva et al., 1999) and pharmacological (Chen et al., 2001) stimulation paradigms. Contrast agent enhanced fMRI techniques were shown to provide a signal-to-noise ratio (SNR) 1.5 to 6 times higher than BOLD imaging, depending on the magnetic field strength of the scanner (Mandeville et al., 1998).

In parallel to the development of fMRI, an increasing number of animal models for various diseases have emerged, mainly based on transgenic mice. This requires further technical improvements due to the smaller brain size in mice as compared to rats. Indeed, the sensitivity of MR scans decreases with decreasing voxel size which directly affects the spatial resolution of the MR image obtained. This problem can be compensated by longer acquisition times (higher number of averaged scans). However, the fact that *in vivo* MRI with animals requires the employment of systemic anaesthesia limits the total experimental time. The monitoring and controlling of physiological parameters (body temperature, respiration, blood gas levels) is another fundamental requirement for performing fMRI on anaesthetized animals and this is still a challenge considering the small size of mice. Recently, the first fMRI studies on mice have been published by Müggler and coworkers (Mueggler et al., 2001; Mueggler et al., 2003; Mueggler et al., 2002). Using a state of the art equipment, these works reported for the first time relative CBV variations in healthy mice, using fMRI in response to a pharmacological stimulation (Mueggler et al., 2001). Subsequently, the same technique was applied to detect hemodynamic response impairments in transgenic amyloid precursor protein (APP23) murine models, using an electrical stimulation paradigm (Mueggler et al., 2002). The evolution of the hemodynamic response could be determined in a long-time scheduled experiment with the same model (Mueggler et al., 2003). Such methods will replace in part invasive techniques, and thus improve the animal welfare and decrease the number of animals that are currently employed in basic research.

The aim of the present work was to apply functional MR imaging to the mouse brain, using a transgenic mouse model to measure the brain response to the neuro-transmitter gamma-amino-butyric acid (GABA). A first goal was to identify *in vivo* cerebral areas related to GABA(B) receptor activation. For this purpose, a pharmacological stimulation paradigm (using the acknowledged GABA agonist baclofen) was chosen. A second goal was to assess with fMRI functional differences between wild type and GABA(B)-$R1^{-/-}$ knock-out mice. In

1997, a gamma-amino-butyric acid receptor type B (GABA(B)) knock out mouse model was produced for the first time (Kaupmann et al., 1997). Mice with a GABA(B)-R1 knock out genotype present a number of phenotypic peculiarities, i.e., hyperactivity (typical clock-wise compulsive running in the cage), epileptic seizures, almost permanent piloerection (which is an indicator of a frightened attitude) and disordered behaviour (in burrow organization, social life). As a third goal, we investigated whether drugs suspected to interact with GABAB receptors act on specific brain regions. Among them was γ-hydroxy-butyrate (GHB), a precursor of γ-amino-butyric-acid (GABA). Recently, GHB has become a popular party drug. Indeed, people ingesting GHB are subject to hypnotic-like cognitive and emotional alterations, not devoid of side effects. Finally, the potential use of *in vivo* $^{13}$C-NMR spectroscopy to study the GHB metabolism in mice was evaluated.

## 3.2 Theory

### Measuring Relative Cerebral Blood Volume Changes

Cerebral blood volume changes can be measured with fMRI with two different methods, using either exogenous intravascular contrast agents that can affect the protons relaxivity (Moseley et al., 1992) or the local magnetic susceptibility (Hamberg et al., 1996). The first method involves the fast injection of a contrast agent into the cardiovascular system of the organism. Subsequently, the signal drop during the first pass of the contrast agent through the microvasculature is quantified (see (Rudin et al., 1997) for a comparison between intra-arterial and intravenous injection). This method is called *Bolus technique* or dynamic susceptibility contrast technique (for a detailed description of tracer kinetics, see (Buxton, 2002), page 318). In short, this technique correlates the variation of the effective spin-spin relaxivity, $\Delta R_2^*$, with the cerebral blood volume, CBV:

$$\int_0^\infty \Delta R_2^*(t)dt \propto CBV \qquad [1]$$

According to this equation, CBV maps[1] can be calculated from measured changes in $\Delta R_2^*$ performed pixel-by-pixel. This relation is valid, because $\Delta R_2^*$ is proportional to the local concentration of the tracer, $C_T(t)$, that changes as a function of CBV. However, it seems that for spin-echo studies the relationship between $\Delta R_2$ and $C_T(t)$ is non-linear, which makes the calculation of the relative CBV (rCBV) less accurate compared to other techniques.

The second method assumes a stable plasma concentration of the contrast agent in the brain. After an intravenous (i.v.) injection, the concentration of the intravascular contrast agent reaches a *steady-state*. The non-linear relationship between $\Delta R_2$ (or $\Delta R_2^*$) and $C_T(t)$ does no longer affect the accuracy, because $C_T(t)$ is theoretically constant. In practice, the stability of steady-state depends on the half-life of the contrast agent in the vascular system, which can become a limiting factor in the duration of an experiment. The use of intravascular contrast agents with a long half-life in blood is recommended.

[1] CBV maps are images where the image intensity represents a certain CBV value.

The measured NMR signal intensity in a particular brain area is influenced by the local contrast agent concentration that changes when the regional cerebral blood volume (CBV) changes. Consequently, changes in signal amplitude reflect changes of the rCBV in that brain area. This method is called *steady-state contrast-enhanced technique*.

After injection of the contrast agent, the transverse relaxation rate ($\Delta R_2$ or $\Delta R_2^*$) in the animal brain varies from the pre-injection baseline. This change is proportional to the local CBV, times some function (f) of the plasma concentration of the paramagnetic contrast agent [P] (Belliveau et al., 1990); (Boxerman et al., 1995). Under steady-state conditions, the plasma concentration of the contrast agent is constant and the transverse relaxation rate is directly proportional to the CBV:

$$\Delta R_2^*(t) = k \cdot CBV(t) \qquad [2]$$

where the constant *k* depends on the injected amount of the contrast agent.

Relative changes of CBV (%), for example during a functional stimulus, can be calculated assuming monoexponential decay of the MR signal and neglecting other interferences, e.g. BOLD effect:

$$S(t) = S_0 e^{-TE \cdot K \cdot CBV(t)} \qquad [3]$$

where $S_0$ is the equilibrium signal before injection of contrast agent, TE is the echo delay and $k \cdot CBV(t)$ describes the transverse relaxation rate $R_2$ (= $1/T_2$) or $R_2^*$ (= $1/T_2^*$), for SE or GRE acquisitions, respectively.

In functional imaging, the relative CBV change related to the functional stimulus can be calculated by correlating the signal intensities measured before the injection of the contrast agent, $S_0$, the signal at steady-state after the injection of the contrast agent, S(0), and the signal during the functional stimulation, S(f). The resulting fractional volume change $\Delta CBV = CBV(t) - CBV(0)$ can thus be expressed as

$$\frac{\Delta CBV(t)}{CBV(0)} = \frac{\Delta R_2^*(t)}{\Delta R_2^*(0)} - 1 = \frac{\ln\left(\frac{S(t)}{S(0)}\right)}{\ln\left(\frac{S(0)}{S_0}\right)} \qquad [4]$$

During exogenous contrast enhanced functional imaging, an opposing effect can occur between increases in $\Delta R_2$* due to the increased blood volume and decreases in $\Delta R_2$* due to endogenous (deoxyhemoglobin) agent (BOLD effects). Therefore, sufficiently high amounts of exogenous contrast agent must be used in order to induce relaxation rate changes that significantly exceed BOLD effects. Recently, Scheffler and coworkers (Scheffler et al., 1999) could quantify rCBV changes and blood oxygenation level and thus separate the competing influences of oxygenation and blood volume changes in $T_2^*$-weighted images, by using an acoustic stimulation paradigm in humans.

## 3.3 Material and Methods

All animal experiments were performed according to the Swiss federal laws for animal protection (animal experiment licence #1897: "GABA-B Rezeptorstudien am Mausmodell").

### Animal Models

Wild type Balb/c and $GABA_{B(1)}$ – deficient (Balb/c $GABA_{B(1)}^{-/-}$) mice were kindly provided by Prof. Dr. Bernhard Bettler (Pharmazentrum, Basel, CH). For the transformation, the $GABA_{B(1)}$ gene of Balb/c embryonic stem (ES) cells (Dinkel et al., 1999) was knocked out by homologous recombination with a targeting vector containing a neomycin (neo) resistance marker flanked by 4.6 and 1.4 kb of 129Sv DNA. The targeted mutagenesis caused a deletion of a 8.5 kb in the $GABA_{B(1)}$ locus carrying the exons 7, 8, 9 and 10 which, together with exons 3-15, are responsible for the encoding of the N-terminal and transmembrane (TM) domains 1-6 of the polypeptidic receptor. The mutant genome was therefore isogenic for all Balb/c genes, except the 6kb recombined 129Sv DNA fragment that replaced the 8.5 kb of the $GABA_{B(1)}$ allele. The resulting $GABA_{B(1)}^{+/-}$ Balb/c cells were injected into C57BL/6 blastocysts and chimeric males were crossed with Balb/c females. The resulting F1 generation of inbred Balb/c $GABA_{B(1)}^{+/-}$ mutant mice was thus heterozygous only for the $GABA_{B(1)}$ mutant allele. Finally, homozygous knocked-out Balb/c $GABA_{B(1)}^{-/-}$ mice were obtained at Mendelian ratio from Balb/c $GABA_{B(1)}^{+/-}$ X Balb/c $GABA_{B(1)}^{+/-}$ breeding pairs (Schuler et al., 2001).

Balb/c $GABA_{B(1)}^{-/-}$ mice present several phenotypic peculiarities at molecular, physiological and behavioural level, e.g., loss of detectable $GABA_B$ binding sites and GABA-induced $GTP_\gamma[^{35}S]$ binding, downregulation of the $GABA_{B(2)}$ subunit, loss of both pre- and postsynaptic $GABA_B$ responses, spontaneous epileptiform activity, hyperlocomotion, hyperalgesia and impairments in passive avoidance learning (Schuler et al., 2001).

### Compounds

Sterile isotonic (0.9% NaCl, which is 9 g/L) NaCl solution was purchased from Fresenius (Stans, CH), Isoflurane was from Abbot (Cham, CH), Endorem (11.2 mg/mL) was from

Guerbet (France), γ-amino butyric acid (GABA) and γ-butyrolactone (GBL) were from Fluka, baclofen was from Novartis (Basel) and 1-$^{13}$C-labelled γ-hydroxy-butyrate was synthesized in our laboratory by Peter Ganz.

## NMR and MRI Scanners

### *In Vivo functional Magnetic Resonance Imaging*

MRI and fMRI experiments were performed on a Biospec 70/20 (Bruker, Karlsruhe, Germany) with a gradient system of 14 cm inner diameter and a permanent magnetic field strength of 7 Tesla. All directives for the pulse sequences were managed through the Bruker manufactured softwares XwinNMR v3.1 and Paravision v2.0/v3.0 running on both Unix and Linux platforms.

### *In Vitro High Resolution $^{1}$H and $^{13}$C NMR spectroscopy*

$^{1}$H and $^{13}$C NMR spectroscopy of the compounds used were conducted on a Bruker DRX 400 (9.4 Tesla) and experimental conditions were chosen as described in chapter 1.

## Animal Preparation for fMRI

Prior to the measurements, mice were kept in type II cages (2-3 animals per cage) in a quiet environment with 12 hours dark/light cycles and had access to fresh water and complete food *ad libitum*.

For the experiments, wild type Balb/c mice and knock-out Balb/c $GABA_{B(1)}^{-/-}$ mice were initially anaesthetized in a chamber where a gas mixture of 3 % Isoflurane in 200 mL·min$^{-1}$ $O_2$ and 600 mL·min$^{-1}$ $N_2O$ was dispensed. Mice were then transferred onto a home-made cradle (wood and plexiglas) and kept under 1.5-2.5 % isoflurane anaesthesia through a mask. Mouse eyes were kept humid with eye protective cream (Cibavision), to avoid damage from drying during the anaesthesia. For the infusions, a cannulation of the tail-vein was performed with a 30-gauge needle (Microlance3, 0.3 x 13 mm) connected to a syringe by a polyethylene tube (inner diameter = 0.4 mm). After cannulation, mice were carefully positioned in the cradle with removable adhesive tape. Particular care was necessary to immobilize the head (to avoid MRI motion artifacts), yet allowing free respiration at all times. A home-made respiration sensor was leant on the mouse abdomen, to record respiration frequency through

diaphragmatic/abdominal mouvements and adapt the dept of the anaesthesia. Finally, the prepared animal was introduced into the scanner for fMRI.

When the homoeothermic mouse heating system became available (formerly only water-operated system for rats), the cradle was replaced by a precasted electrical heating blanket and a lubricated rectal thermometer connected with the feedback heating system was employed to stabilize the mouse body temperature.

## MRI Protocol

The radiofrequency probe was an Alderman-Grant of 30 mm inner diameter. The imaging protocol for relative CBV changes visualization consisted of a fast spin-echo relaxation enhancement (RARE) sequence. Parameters: TR = 1100 ms; effective TE = 45 ms; RARE-factor = 8; FOV = 1.6 x 1.6 $cm^2$; matrix dimension (MTX) = 128 x 128; slice thickness (SLTH) = 1 mm; frequency sweep width = 50 kHz; 7 slices, resulting in an acquisition time of 18 s; number of averages/averaged experiments NA = 2 and NAE = 10, respectively, resulting in a total acquisition time of 6 min.

## fMRI Protocol

The protocol developed for functional NMR imaging of relative CBV changes, consisted of an automated repetition (20 times) of the above described series, resulting in a total experimental duration of 2 hours. After 3 scans (18 min) of a pre-contrast base line, 50 mg Fe/kg body weight of superferromagnetic nanoparticles (Endorem®) were injected i.v. as contrast agent. After 4 more scans (24 min) to reach stady state, 5 mg baclofen/kg body weight or a correspondent volume of isotonic NaCl solution (placebo) were infused through the intravenous (i.v.) tail cannulation.

## Analysis of fMRI Acquisitions

Images were analyzed according to signal intensity changes over time using the software BioMap 2.x (Martin Rausch, Novartis-Pharma AG, Basel) and CBVrel changes were calculated according to eq. 4.

## Monitoring of Physiological Parameters

### *Anaesthesia*

Mice were anaesthetized with a gas mixture of 0.7-3 % Isoflurane in 200 $mL \cdot min^{-1}$ $O_2$ and 600 $mL \cdot min^{-1}$ $N_2O$, through a face mask. The animals were allowed to breathe spontaneously and the isoflurane concentration was regulated in order to keep a constant breathing rate of ~ 60 $min^{-1}$.

### *Respiration*

The monitoring of the breathing rate was achieved using a home-made mechanical/fiber optic sensor, connected to the computer. The sensor (consisting of a thin plexiglas strip connected to a light gate) was carefully situated on the abdomen of the mouse, near the costal arch. Shifts of the plexiglas strip induced by the respiratory movements, in turn interrupted the passage of a fiber optic beam and were monitored on the computer.

### *Temperature*

In initial experiments, regulation of the mouse body temperature could not be made. In a later moment, a homoeothermic blanket system (Harvard Apparatus, Holliston, MA, USA) became available. Here, mice were placed backside on the heating blanked and a rectal thermometer was used to record the body temperature. The thermometer was connected with a feedback system aiming at a stable measured temperature of 37 °C.

## 3.4 Results

The purpose of the present chapter was to develop a fMRI protocol to identify specific activated brain regions in mice after pharmacological stimulation of GABA-B receptors.

### Determination of Tissue-specific Relaxation Times in the Mouse Brain

The sensitivity to detect minute changes in CBV measurements is highest if the effective TE of the fMRI sequence is chosen close to the T2 of the tissue (Figure 3.1).

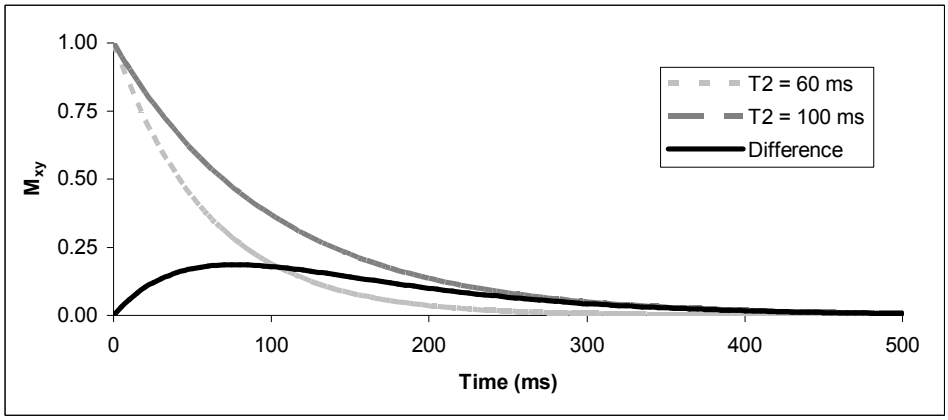


Fig. 3.1. *Decay of the transverse magnetization $M_{xy}$ after a spin excitation as a function of the relaxation times*. Two spin populations with different relaxation times T2 = 60 and 100 ms were plotted. Here, changes in R2 can be best detected at a time point where the difference between the relaxation curves is maximized, i.e. exactly between both relaxation times (here 80 ms).

Therefore, determination of T2 in different brain areas are required especially with addition of the contrast agent Endorem® (see Figure 3.2)

For this purpose, the relaxation times of different brain areas were measured by using a multislice-multiecho spin echo (MSME) imaging sequence, where the echo spacing between consecutive images were set to a 20 ms spacing. This sequence is a modified Carr-Purcell-Meiboom-Gill (CPMG) sequence where the spins are first excited with a 90° pulse and the signal is repeatedly measured during consecutive 180° refocusing pulses:

$$(\pi/2)_X - \tau - \pi_Y - 2\tau - \pi_Y - 2\tau - \pi_Y - \ldots$$

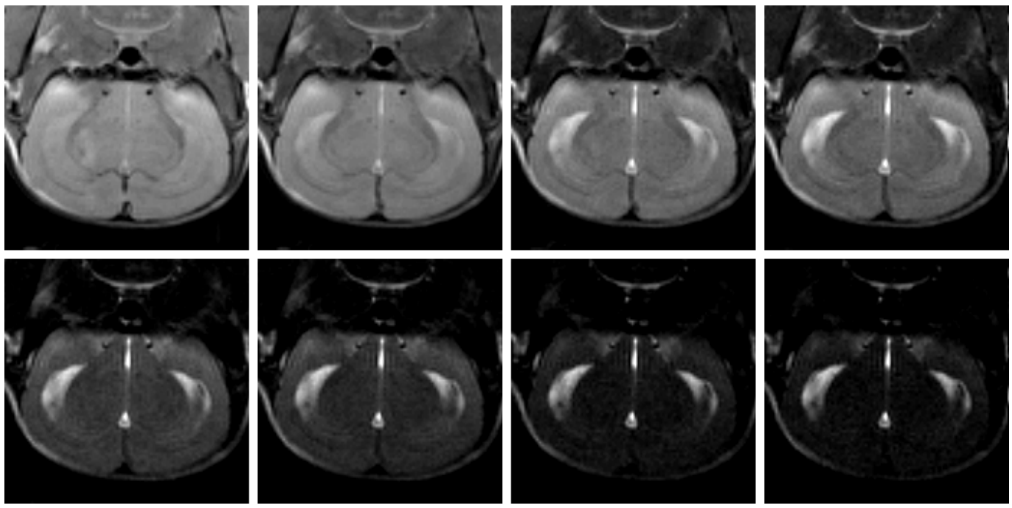

Figure 3.2. *Determination of tissue-specific T2 in the Mouse Brain* using a multislice-multiecho (MSME) spin-echo MRI sequence with a echo spacing of TE = n·20 ms between adjacent images; taken without (upper row) or after (lower row) intravenous injection of the intravascular contrast agent Endorem® (50 mg/kg body weight). Field strength B = 7T, TR = 2500 ms. The decay of the MR signal (due to the differential relaxation rates) in different brain areas represents a critical factor to choose (i) an optimal TE in fMRI (ii) the preservation of sufficient signal from the fast-relaxing cerebral regions must be chosen.

The images of Figure 3.2 show that the NMR signal in some brain areas relaxes slower than in others. A quantitative analysis of the image intensity in the different brain regions was fitted to $M = M_0[\exp(-t/T_2)]$. Long relaxation times were found in the brain areas with high water motility, such as ventricle (average T2 of 170 ms and 125 ms for normal brain and in the presence of 50 mg/kg body weight Endorem®, respectively) or a high fat content (average T2 = 90 and 80 ms). The shortest relaxation rates could be observed in the muscular tissues where the water motility is restricted (average T2 = 35 and 25 ms). Data are reported in Figure 3.3.

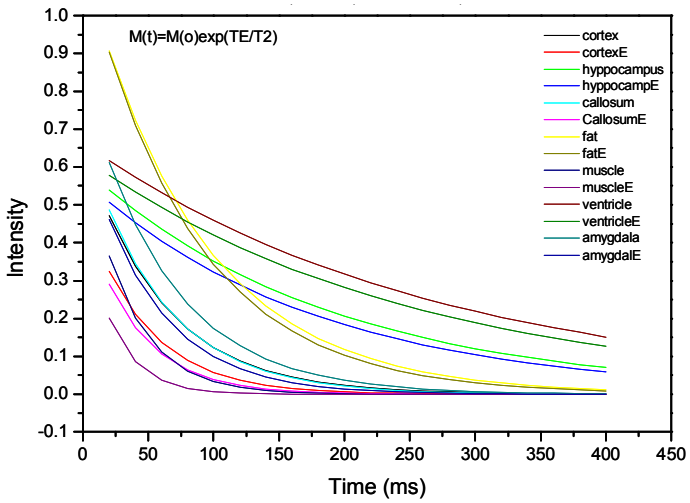


| T2 (ms) | control | Endorem |
|---|---|---|
| cortex | 50-60 | 40-50 |
| ventricle | 140-20 | 100-150 |
| amygdala | 55-65 | 45-50 |
| muscle | 30-40 | 20-30 |
| fat | 80-100 | 70-90 |

Figure 3.3. *Tissue-specific Relaxation Time T2 in different Brain Areas*. The spin-spin relaxation time T2 at 7T was calculated from MSME MRI scans in several brain areas of the mouse prior and after i.v. injection of 50 mg/kg body weight of the intravascular superparamagnetic contrast agent (Endorem®) according to the monoexponential decay function $M = M_0[\exp(-t/T_2)]$. Average values resulting from the analysis are reported in the table on the right.

As reported by Kaupmann and coworkers (Kaupmann et al., 1997), GABAB receptors are distributed homogeneously throughout the brain (see Figure 3.4). However, it is not possible to foresee which specific anatomical regions are activated upon systemic baclofen administration - an agonist of the GABAB receptor. The fact, that analogues compounds to baclofen, such as GHB (also found to be a weak GABAB agonist) affects emotional and sensorial processes, may suggest an involvement of brain regions connected to the limbic system. For our experiments, we thus adapted the TE of the RARE sequence to the T2 measured in the cortical and amygdaloid regions in the presence of endorem (average T2 of 60 ms). At the same time, however, we performed multislice (7) scans, in order to cover an extensive brain volume.

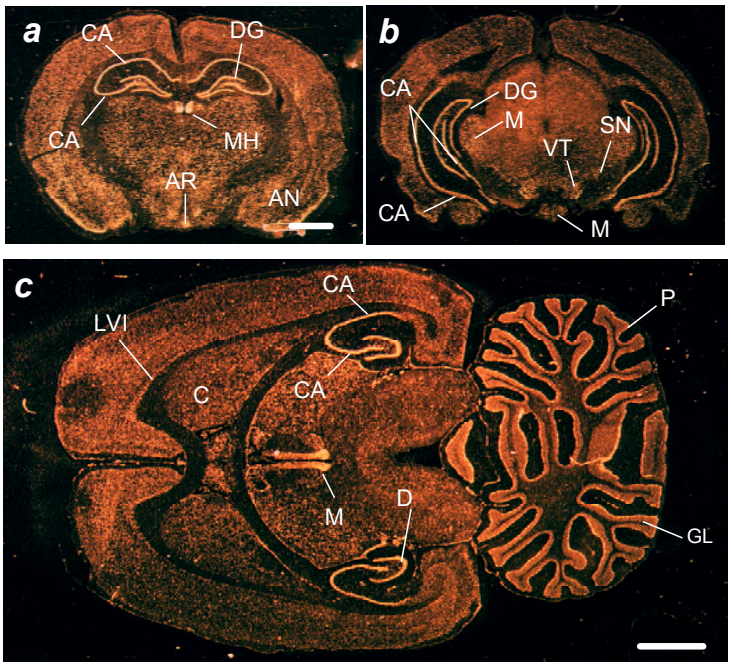


Figure 3.4 *In situ hybridization analysis of GABAB-R1 transcripts in rat brain*. Tissue sections were hybridized to $^{35}$S-labelled antisense probes. Darkfield illuminations of representative autoradiograms of coronal (a,b) and horizontal (e) sections. A) dorsal hippocampus plane; b) ventral hippocampus plane; c) dorsal tier of the brain. Transcripts are abundant in all cerebral cortical layers, especially in the layer IVb (LVIb), and many subcortical structures. CA1-CA3: pyramidal cell layer subfields of hippocampus; DG: dentate gyrus; MH: medial habenula; MG: nucleus geniculatus medialis; SNc: substantia nigra, pars compacta; VTA: ventral tegmental area; AN: amygdaloid nuclei; ARH: nucleus arcuatus hypothalami; MM: corpora mammillaria; P: Purkinje cells of the cerebellum; GL: granular layer of cerebellum. The pictures are a personal courtesy of Prof. Bernhard Bettler, university of Basel. Adapted from (Kaupmann et al., 1997).

## Baclofen-Induced Cerebral Blood Volume Changes in wt Mice

To assess changes in the relative CBV of specific brain regions of wild type Balb/c mice, modulations of the MRI signal from the post-contrast base-line were recorded, then roughly screened on a pixel-to-pixel basis with a Paravision analysis tool and then with the software Biomap (Martin Rausch, Novartis-Pharma AG, Basel). After defining an intensity threshold, groups of voxels corresponding to specific brain regions were merged into selected regions of interest (Roi). From Roi, the relative cerebral blood volume change ($CBV_{rel}$) upon baclofen systemic injection was calculated considering the NMR signal intensities pre- and post-injection of the contrast agent, according to the equation (4). After screening of several regions in the different slices of the mouse brain, one region was identified, that presented significant activation in both hemispheres, after injection of baclofen (5 mg/kg body weight). The two vertical red dashed lines define the brain volume included in the MRI scans shown in Figure 3.5 B) and C). As an histological reference, Figure 3.5 A) reports a pictorial representation of the murine brain surface.

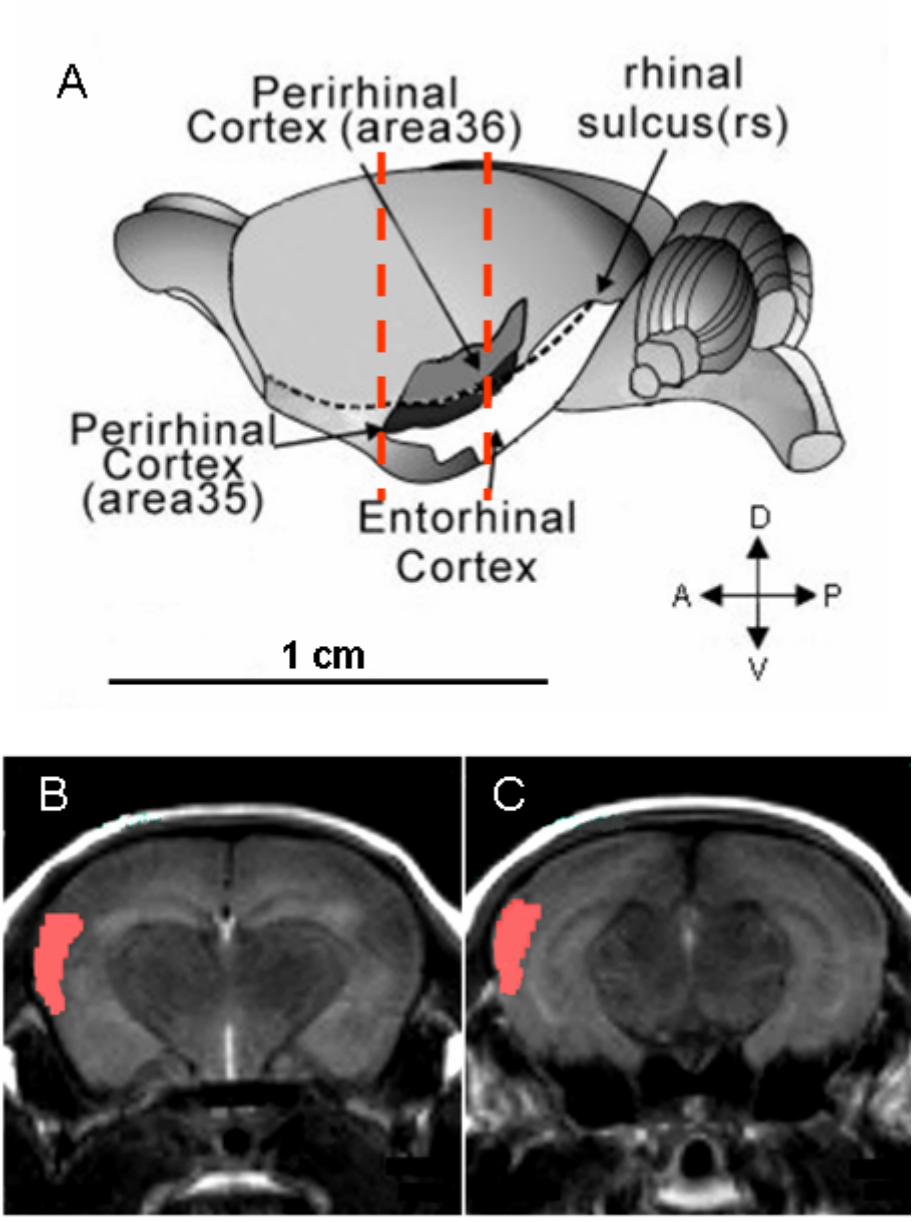


Figure 3.5. *Activated Regions of Interest (ROIs) in the Mouse Brain*. A) Sketch of the murine brain surface: the dashed red lines display the imaging planes selected for fMRI scans B) and C); the indicative topography of the sulcus rhinalis (rs), cortex perirhinalis (areas 35 and 36) and cortex entorhinalis is highlighted in dark grey. A,P,D,V indicate anterior, posterior, dorsal and ventral orientations of the brain, respectively.
B) and C): steady-state contrast enhanced fMRI of a Balb/c mouse (coronal scans): after reaching steady-state with the contrast agent (i.v. injection of 50 mg/kg body weight of Endorem®), a dose of 5 mg/kg body weight of the GABA agonist baclofen was injected i.v. The red areas include the regions of interest (Roi) in which a significant change in CBV was observed.
RARE sequence at 7T: TR = 1100 ms; effective TE = 45 ms; RARE-factor = 8; FOV = 1.6 x 1.6 $cm^2$; MTX = 128 x 128; SLTH = 1 mm; frequency sweep width = 50 kHz; number of averages/averaged experiments NA = 2 and NAE = 10, number of repetitions NR = 20 including pre-contrast scans. Slice positions are B) ~ -1 mm and C) ~ -2.5 mm from Bregma.

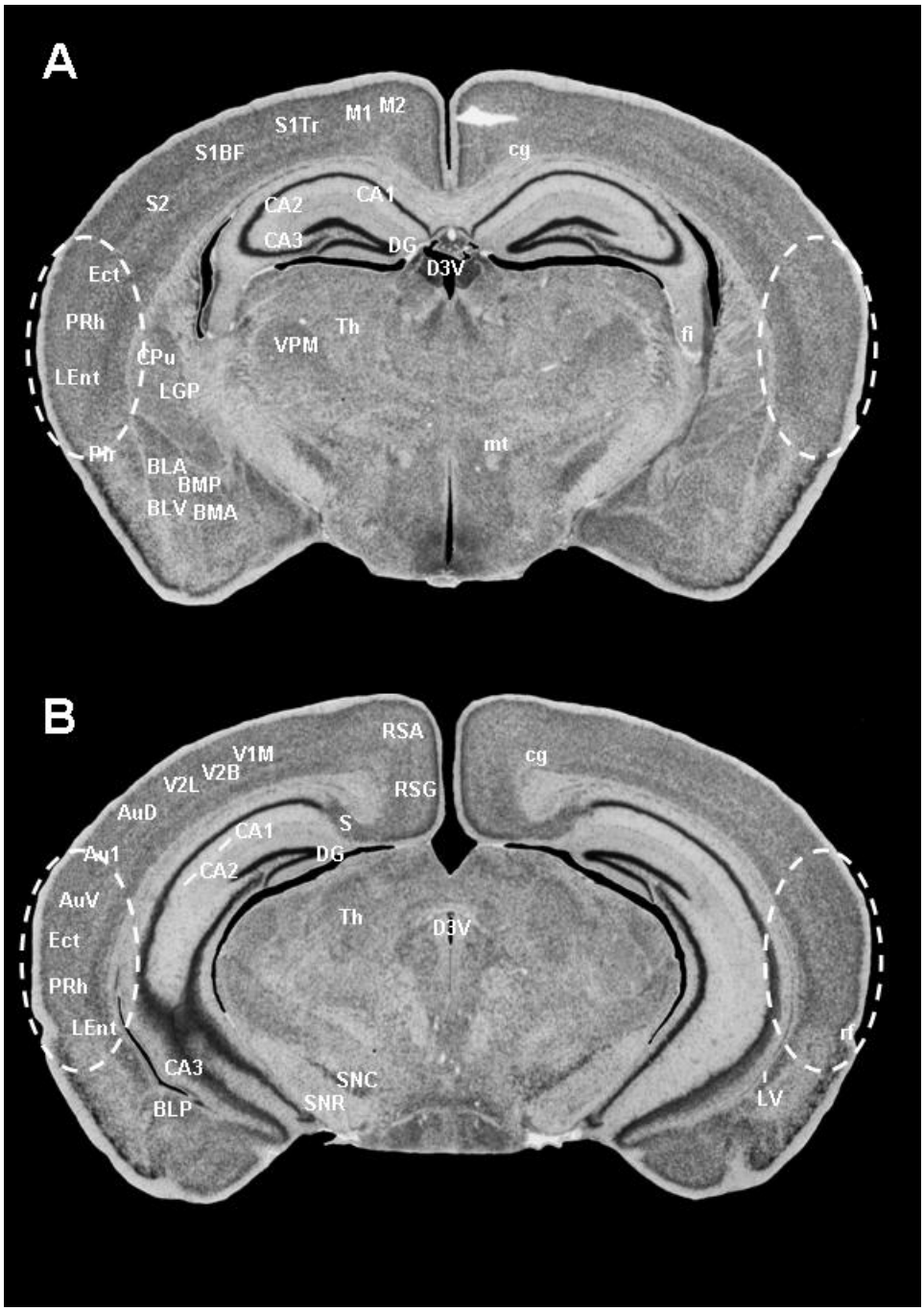


*Figure 3.6 Histological Sections of the Mouse Brain*. Slices positions: A) Bregma: -1.64 mm; interaural: 2.16 mm; B) Bregma: -2.75 mm; interaural: 1.05 mm. The dashed white lines include the regions activated upon baclofen exposure, as shown by fMRI at 7T. Anatomical abbreviations: Ect: cortex entorhinalis; PRh: cortex perirhinalis; LEnt: cortex entorhinalis lateralis; AuV: auditory cortex, pars ventralis; Au1: primary auditory cortex; AuD: auditory cortex, pars dorsalis BMA, BMP, BLA, BLV, BLP: nuclei corpum amygdaloideum; S2: second somatosensory cortex; RSA, RSG: retrosplenial agranular/granular cortex; cg: cingulum; D3V: ventriculus tertius (dorsal part); CPu: putamen and ncl. caudatus (striatum); LGP: ncl. pallidus lateralis (ncl. lentiformis); CA1,CA2,CA3: hippocampal fields; DG: gyrus dentatus; fi: fimbria hippocampus; S: subiculum; mt: tractus mammillothalamicus; rf: fissura rhinalis; Pir: cortex piriformis; SNC, SNR: substantia nigra (pars compacta and pars reticularis); LV: lateral ventricle; S1BF, S1Tr, S2: somatosensory cortex (primary and secondary); M1, M2: primary and secondary motor cortex; V1M, V2B, V2L: visual cortex (primary and secondary); Th: thalamic area; VPM: thalamic nucleus (ventral posteromedial). Adapted from "The Mouse Brain Library" (National Institute of Mental Health, USA).

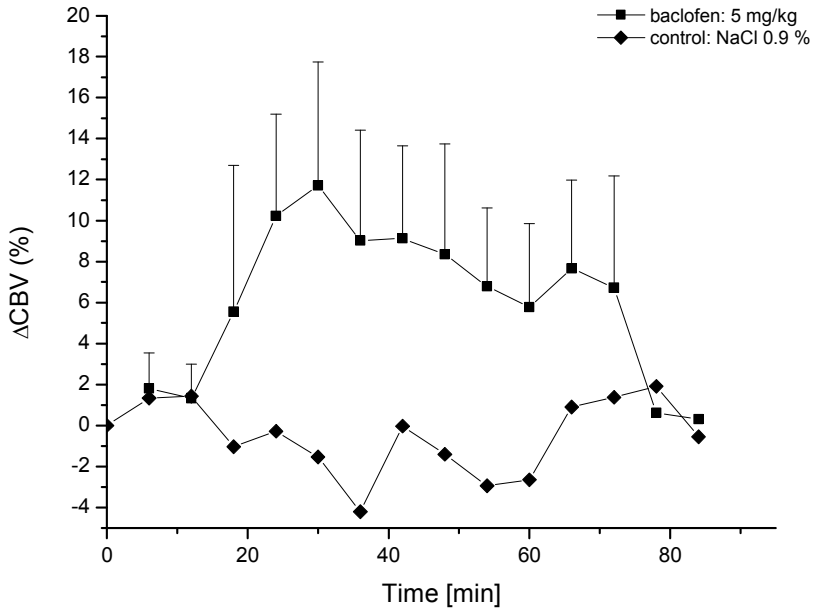


Figure 3.7. *Baclofen-induced Brain Activation in Balb/c Mice*. Relative CBV changes are plotted as a function of time since administration of baclofen (min). In a group of four Balb/c mice (black squares), i.v. injection of baclofen at a dose of 5 mg/kg body weight was injected. In a control animal (dark diamonds), a correspondent volume of saline isotonic solution (NaCl 0.9 %) was administered instead of baclofen.. A significant ($P<0.001$) ΔCBV(%) of ~ 10-12 % appears bilaterally in cortical regions including auditory, perirhinal and entorhinal cortex. Vertical bars represend SD. Mice are freely breathing. No heating system. Isoflurane concentration of 0.6-1.2% in the gas mask.

Figure 3.7 displays the relative change of CBV in wild type Balb/c mice brain, against time. The data were extracted from the highlighted region of interest situated in the brain cortex (Figure 3.5 B) and C), red ROI), comprising the auditory, perirhinal and entorhinal cortical areas (see Figure 3.6). In figure 3.7, the first three points (corresponding to scans 0-2), were considered as steady-state baseline Endorem concentration. In a group of 4 mice, the injection of the GABA agonist baclofen caused a decrease of the signal intensity in the selected cortical area, corresponding to a $CBV_{rel}$ increase of ~ 5 %. The $\Delta CBV_{rel}$ reached a maximum of 10-12 % after 18 minutes after the agonist injection (black squares). The baseline was reached again after 48 minutes. Data correspond to mean values ± standard deviation from 4 different animals. As a control, an equivalent amount of isotonic NaCl solution was injected in a mouse of the same progeny (black diamonds). In this case, no larger changes in $\Delta CBV_{rel}$ were observed. The difference in the median hemodynamic response

measured between the control and positive subjects was assessed by non-parametrical analysis (Mann-Whitney) and showed statistical significance ($P<0.001$).

These initial experiments were performed without an appropriate system to keep a constant mouse body temperature. Considering the temperature evolution reported in Figure 3.9, it is clear that the animals were measured in hypothermic conditions and the consequence of this will be discussed in the next section. We therefore limited the number of animals used to 5 (4 positive stimulations and 1 placebo control).

When a homoeothermic blanket system became available (see material and methods in section 3.2), further experiments were performed with the new experimental setup. In these cases, two wild type and one knock out model were measured at a constant measured rectal temperature of 37 °C. For the evaluation of the temperature regulation device, a few observations deserve attention: 1) to keep a rectal temperature of 37 °C, the blanked surface had a temperature of 54 °C, which is a dangerous condition for the animal skin in contact; 2) under these heated conditions, the same concentration of 5 mg/kg body weight of baclofen was much less tolerated than under hypothermic conditions which resulted in a deep respiratory depression at the limit of respiratory failure. We therefore limited the investigation with this second experimental setup to 3 animals (2 wt and 1 ko). Future experiments should aime at reducing the baclofen concentration at these temperatures and at stabilizing the temperature over a longer time (to avoid larger T differences between rectum and blanket).

Comparison between wt and ko strains led to the following conclusions: paralysis and strong respiratory depression after baclofen administration was only observed in wt mice and such instability was not only limited to the brain, but was a generalized effect (oscillation even in muscular tissues), fMRI data show (Figure 3.8) that a change in CBV in wild type mice was observed, in contrast with GABAB-R1 k.o. animals. However, this significant cortical activation observed in the first experimental setup (see Figure 3.7) could not be reproduced when using the heating device. The possible reasons for these differences will be discussed in the next section.

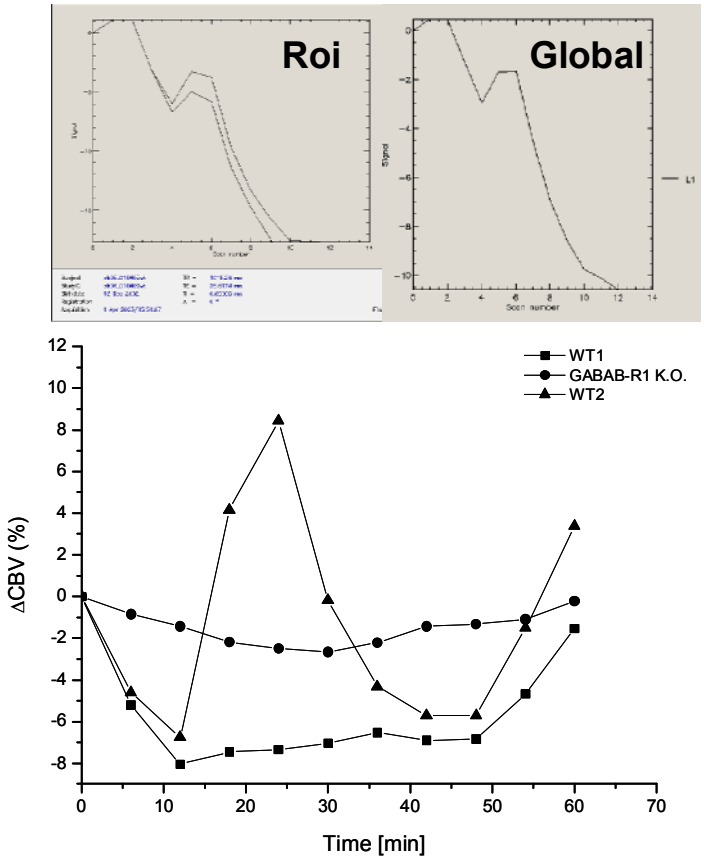


Figure 3.8. *Baclofen-induced Brain Activation in Balb/c Mice*. Percent CBV changes in cortical Roi as in Figure 3.5 are reported as a function of time (min), after administration of baclofen at 5 mg/kg body weight. Experiments were performed with two Balb/c wild type (black squares and triangles) and one GABAB-R1 knock-out (black circles) mice. Freely breathing animals. Rectal temp. = 37 °C kept stable through electrical heating blanket. Isoflurane concentration of 2-2.5% in the gas mask.

## Correlation Between Mouse Body Temperature, Respiration and Anesthesia

In our experiments, mice were allowed to breathe freely and were kept under anaesthesia through a face mask. Under anaesthesia, the endogenous capacity to regulate body temperature is impaired. For this reason, we investigated the evolution of body temperature of anaesthetized mice left at room temperature (20 °C), in the absence and presence of a heating device. In parallel, we monitored the breathing rate and the concentration of isoflurane required to keep the mouse anaesthetized.

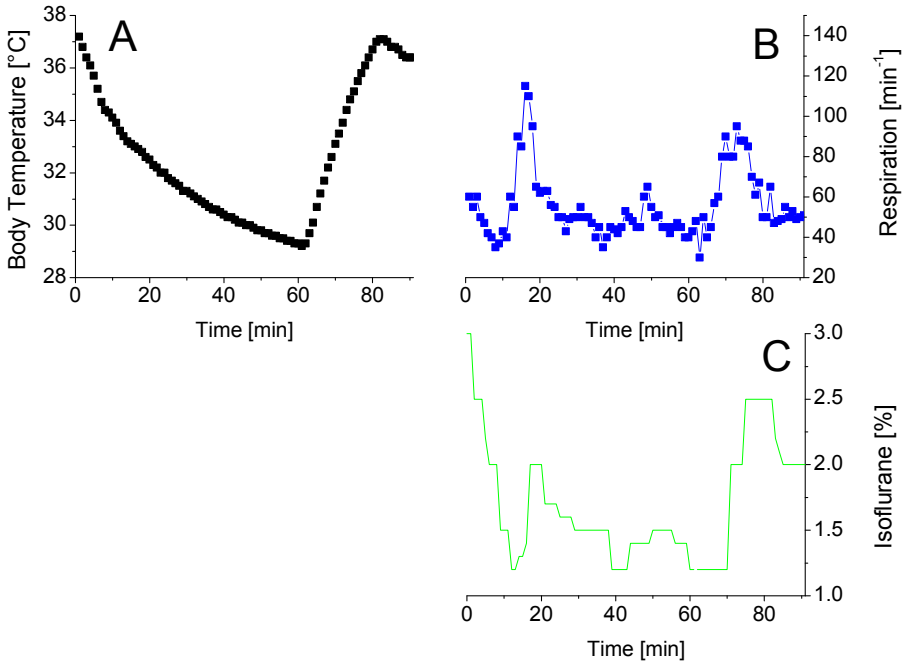


Figure 3.9. *Evolution of temperature and Breathing Rate during Anaesthesia*. The plots report: A) the measured rectal temperature of a Balb/c mouse breathing under face-mask anaesthesia with Isoflurane/$O_2$/$N_2O$; B) the breathing rate of the animal during the same experiment (blue squares), and C) the required concentration of Isoflurane necessary to keep the animal anaesthetized (green line).

In figure 3.9 A) the variation of mouse body temperature is displayed against time (black squares). Here, the temperature decreases exponentially with time. In the experiment shown, already in the first minutes, the rectal temperature decreases by approximately 0.4 °C/min. After 60 minutes, the temperature decreased to 29.3°C indicating the need for a heating device. At time t = 62 min., the heating blanket was turned on, leading to a rapid increase of

the body temperature up to 37 °C, which was the programmed temperature in the homeothermic system. At all times, the concentration of isoflurane was adjusted to limit respiratory depression and stage IV narcosis (= asphyxia), (Figure 3.9 C), green line): after 10 minutes, isoflurane was set to 1.2 % and the mouse came to a breathing rate of 30-35 breathes/min (Figure 3.9 B). Note that at this time the rectal temperature droped to 33 °C. By keeping this isoflurane concentration, the respiration frequency increased a few minutes later up to 100 breathes/min and the mouse tended to wake up. The isoflurane was shortly increased to 2.0 %. As a consequence, a respiration was depressed again to 40 breathes/min. After 40 min, however, isoflurane concentration could be decreased again to 1.2 %, without waking up the mouse (in other mice, isoflurane concentration could be even kept as low as 0.6 %) having a rectal temperature of 30 °C. 62 minutes after the beginning of the experiment, the mouse rectal temperature was of 29 °C. The heating blanket was then turned on, leading to a rapid increase of the mouse rectal temperature up to 37 °C. As a consequence of the temperature increase, the breathing rate increased distinctly after a 2-3 minutes delay, and the mouse started to wake up. The isoflurane concentration was subsequently increased, to keep the animal anesthetized. At a rectal temperature of 37 °C, the mouse could not be kept under anesthesia with an isoflurane concentration lower than 2 %. These observations indicate that a heating device is necessary to maintain the mice at physiological temperatures even during 60 min fMRI experiments and that a tracheal intubation (artificial ventilation) of the mouse would facilitate the regulation of the anaesthesia.

## Analysis of GABA precursors for *in vivo* $^{13}$C-NMR spectroscopy

Activation of brain regions with GABA agonist leads to the question of how the GABA agonists are metabolized in the mouse brain. With the goal to investigate the GABA metabolism in the mouse brain *in vivo*, we first recorded *in vitro* high resolution $^{13}$C-NMR spectra in order to characterize the molecules of interest. Three compounds, namely GABA, GBL and GHB, were considered.

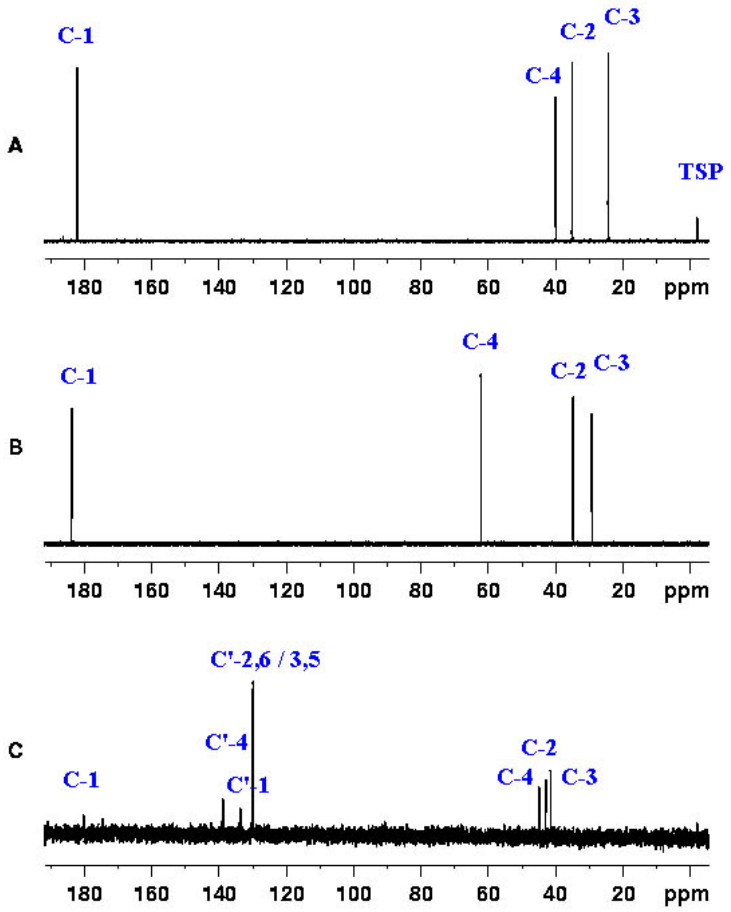


Figure 3.10. *$^{13}$C-NMR Spectroscopy of GABA and Related Metabolites*. (A) GABA, (B) GHB and (C) baclofen.

In Figure 3.10, $^{13}$C-NMR Spectra of GABA, GHB and baclofen are shown. The main differences are represented by the C-4 shift induced by the -OH residue of GHB (in comparison to GABA) and the phenyl ring of baclofen, indicated by the resonances C'.

The biosynthesis of GABA occurs in the brain via decarboxylation of glutamate by 1-Glutamic Acid Decarboxylase (GAD). The metabolism of GABA proceeds via transamination to succinic semialdehyde by the enzyme GABA transaminase (GABA-T). After a dehydrogenase step, the molecule re-enters the TCA cycle as succinate acid (Daikhin and Yudkoff, 1998). The resonances C-4 and C-3 should thus be sensitive in vivo NMR parameters as they are strongly affected by all 3 enzymatic steps. Small changes in carbon C-3, however, will be hard to detect by *in vivo* spectroscopy because it overlaps with much stronger signals from tissue lipids (-CH2- groups, 24-32 ppm) - in contrast to C-4. Carbon C-1 is also unsuited for 13C labeling experiments because it also overlaps with tissue lipids (-COOH group, 180 ppm) and has a long relaxation T1 time which causes signal saturation during rapid pulsing experiments.

## 3.5 Discussion

The aim of the present study was to develop an fMRI protocol for imaging mouse brain activity after GABAB activation. To target GABABergic activation, we chose a pharmacological stimulation paradigm involving a systemic infusion of the known GABA agonist baclofen. The experiments were carried out on Balb/c mice. In addition to wild type mice, our study included a recently established strain derived from Balb/c mice by Bettler and coworkers (Schuler et al., 2001), in which the genes coding for GABAB-R1 receptor subunits have been stably knocked out. The goal was to compare wild type vs K.O. mice, in order to elucidate neural patterns underlying cerebral GABABergic activity. We were also interested in γ-hydroxybutyrate (GHB), a GABA derivative with agonistic affinity for GABAB receptors (Lingenhoehl et al., 1999) which is increasingly employed as life style drug (Wong et al., 2004).

In a group of four Balb/c wild-type mice, a significant transient increase (30-40 min) of $CBV_{rel}$ in the order of 10-12% was observed after the systemic injection of 5 mg/kg body weight of baclofen. The hemodynamically activated brain regions included parts of the perirhinal, entorhinal and ventral auditory cortical areas. The maximum $\Delta CBV_{rel}$ was observed at ~20 min after baclofen infusion and returned to basal values after ~ 1 hour.

The activation could be monitored by fMRI at 7T with a spatial resolution of 125 x 125 μm in the in-plane dimensions and a slice thickness of 1mm.

Especially for small animals with limited tissue volume such as mice, MRI tends to be a compromise between image resolution and physiological stability: the higher the resolution, the less signal per voxel, the more signal averaging (= accumulation time) is required for an acceptable contrast. Signal averaging, however, is not only limited because of the stability of the animal in anaesthesia, but also because of the time window of the observed effect and the desired temporal resolution to follow such processes. In our experiments, the pharmacological GABAB receptors stimulation was expected to result in a long-lasting effect (slow synaptic inhibition; in the order of minutes), different from an electric stimulation with only a short transient effect (in the order of seconds). Considering a total experimental time above one hour, the number of averages were chosen such as to yield a good image quality, yet still a good temporal resolution for the drug effect: the time to record 7 brain slices was 6 min for the present experiments.

## Relation between observed CBV Changes, Physiological Parameters and Anesthesia

The appropriate monitoring and control of physiological parameters such as respiration, body temperature and blood gases concentration is crucial for a correct experimentation and interpretation of experimental results especially in fMRI. The small size of mice, which are one order of magnitude smaller than rats, make this task particularly challenging.

In the present experiments, the mice had no tracheal intubation which is routinely used in humans in clinical anaesthesia. This procedure allows a mechanical regulation of the breathing rate, though this might cause severe injuries of the trachea when performed in such small organisms as mice. Therefore, the anaesthesia gas was provided by a face mask and the breathing rate was maintained at 60/min by adjusting the amount of isoflurane (reciprocal correlation). At physiological temperature (38°C in mice), the drop from 100 breathes/min to 60/min as caused by the isoflurane provides usually a reasonable anaesthesia. On the one hand, free breathing is advantageous for handling. On the other hand, respiratory depression caused by anaesthesia and pharmacological stimulation, together with the physiological breathing irregularities, such as respiratory sinus arrhythmia (Neff et al., 2003) can lead to artifacts (blood gases and blood pressure changes) and critical conditions for the animal.

The anaesthesia regulation used in our experiments has an important co-variable that might be fundamental for the discussion of the fMRI results: the breathing rate does not only depend on the amount of isoflurane (reciprocal relation), but also on the temperature (proportional relation).

The first set of experiments was carried out in the absence of the appropriate mice heating device. To keep a stable mouse body temperature at physiological conditions (38 °C), an electrical homoeothermic feedback system was introduced in the later experimental setup. By inducing a hypothermic state (29°C) when the mouse heating device was not yet available, the first group of mice lowered their breathing rate already by hypothermia, so that less isoflurane was required to adjust the breathing rate to 60/min (0.5 - 1.2% instead of 2 - 2.5%, compared to mice at 37°C). The anaesthesia was less pronounced in this group of mice and the mice were more sensitive to sensorial (auditory and olfactory) stimulation under the influence of baclofen. In contrast, the thermo-stabilized mice (37°C) experienced a more profound anaesthesia (higher isoflurane content 2-2.5%). Therefore, the previously observed brain activation was not observed in the second group. In addition to the more pronounced

anaesthesia, isoflurane causes a general lowering of neural processes (Simon et al., 2001; Sugimura et al., 2001), has strong vasodilatory effects (Matta et al., 1999) and can interact with baclofen activity (Sugimura et al., 2002).

Comparison of both mice groups allows the following two conclusions: (i) in fMRI, the existence of activated brain areas might be highly dependent on the depth of the anaesthesia. (ii) In order to eliminate breathing artefacts, the breathing gas should be administered by mechanical ventilation.

The mice heating device could also be improved: heat was provided only by a half-body through which lacked a heating blanket on top of the animal. The feedback system, however, is regulated according to the input from the rectal thermometer and mice have a very low thermal inertia because of the high body surface/volume ratio. To keep 37°C rectal temperature, the single-sided heating blanket needed a temperature of 54°C, which is a dangerous condition for the mouse skin. Consequently, the surface temperature of the abdomen is much colder, because of its contact with cold air in the MRI tube (16-18 °C). This strong temperature gradient results in an instability of the vascular circulation, and thus affects the CBF and $\Delta CBV_{rel}$ measurements in fMRI. This technical system could be improved either by a double-sided heating device or by heating the entire MRI tube (including the mice) with hot air. However, this would be only possible in combination with intratracheal intubation.

Beside the less pronounced anaesthesia, also the direct effects of hypothermia on CBV could be responsible for the large CBV changes observed in the first group of mice. Hypothermia reduces CBF and CBV as a consequence of the reduced metabolism (Thomas et al., 2001). Such conditions have been shown to increase the signal amplitude originating from $CBV_{rel}$ changes during fMRI (T. Mueggler, personal communication).

Finally, the biological effects of baclofen on respiration (Olpe et al., 1978) and its different pharmacodynamics at different temperatures must also be considered. Besides its relaxant activity on muscles, baclofen has been shown to reduce the respiratory rate in rats, (Sved and Tsukamoto, 1992; Trippenbach, 1995). Moreover, it can alter blood dependent parameters such as CBV although there is non consense in the existing literature. Depending on the dose and site of injection (Chahl and Walker, 1980), baclofen can lower the blood pressure (Saito et al., 1999), especially in combination with anaesthesia (Brouillette and Couture, 2002; Lyew et al., 2003) or induce an increase of arterial pressure (Landulpho et al., 2003) and heart rate (Trippenbach and Lake, 1994). In contrast, it has also been reported that

baclofen has no effect on arterial pressure, but modulates the carotid chemoreceptor reflex (Suzuki et al., 1999).

It can be concluded that the moderate hypothermia and anaesthesia technique used for the first group of mice had some advantages to detect CBV changes after systemic baclofen infusion.

## $CBV_{rel}$ Changes in the Auditory Cortex after Systemic Baclofen Infusion in Wild-type Balb/c Mice.

The discussion of the observed brain activation (auditory cortical areas) requires a brief summary of known brain anatomy. The auditory pathways starts from the nervus vestibulocochlearis, which projects separately toward vestibular and cochlear nuclei. From there, the auditory tract continues through the corpus trapezoideum and the lemniscus lateralis, and the information is projected to the colliculus inferior (IC), which is a crucial switching centre for acoustic reflexes. Through the pedunculus colliculi inferioris, the auditory tract continues to the medial geniculate body, which is then connected tonotopically to the auditory cortex. Few years ago, highly organized corticocollicular projections were described (Herbert et al., 1991).

The colliculus inferior was recently shown to be sensitive to baclofen (Ma et al., 2002; Zhang and Wu, 2000). According to those findings, GABAergic inhibition in the auditory midbrain can be suppressed by a presynaptic activation of GABAB receptors. Here, stimulation with baclofen was shown to decrease the amplitude of inhibitory postsynaptic potential (IPSP) in the inferior colliculus (Ma et al., 2002), and thus promote the induction of long-term potentiation (LTP), in the presence of electrical activity in more peripherical regions of the auditory network, such as the lemniscus lateralis (Zhang and Wu, 2000).

Our fMRI data show an activity change in auditory cortical areas, in terms of $CBV_{rel}$ changes, under the influence of baclofen. In our experiments, a continuous auditory stimulation is provided by the MRI gradients noise. Baclofen in the CNS could open the “IC gate”, which would lead to the alteration of the auditory excitation. Ultimately, this temporal pattern would correlate with a metabolic degradation of baclofen. On the basis of this auditory stimulation, it becomes more evident why one group of mice (not thermoregulated, ~ 0.5 – 1.2 % isoflurane) did show this activation, whereas another group of mice (thermostabilized, ~2 – 2.5 % isoflurane) was no longer sensitive to this baclofen-enhanced auditory stimulation. Our

project started with the screening of brain regions that could be activated under the influence of baclofen. Now that an activated brain region has been found and plausible interpretations have been proposed, a more detailed investigation should test this hypothesis. For example, the experiments could be repeated by isolating the animal from external auditory stimuli, using different degrees of anaesthesia and sire more attention to anatomical parts connected with the auditory network, such as the IC.

## $CBV_{rel}$ Changes in the Perirhinal/Entorhinal Cortex after Systemic Baclofen Infusion in Wild-type Balb/c Mice.

Baclofen systemic administration resulted in a selective activation of cortical areas comprising brain regions including the auditory, perirhinal and entorhinal cortex of Balb/c wild-type mice.

On the basis of the present experiments, it is not possible to elucidate the neurophysiological mechanisms causing the activation. However, a comparison with other studies allows a better understanding of how the activation of GABAB receptors could lead to such regional CBV changes.

The effect of baclofen and other GABA agonists (such as GHB) on the functioning of memory has been discussed before (Teter and Guthrie, 2001). Behavioural studies in rats and mice describe impairing (Pitsikas et al., 2003; Stackman and Walsh, 1994), as well as enhancing (Saha et al., 1993; Sharma and Kulkarni, 1993) effects of baclofen on the achievement of memory requiring tasks. Memory and learning are highly complex tasks that involve many brain areas that are part of the limbic system. A schematic representation of the connections between these brain regions is shown in Figure 3.11. It is assumed that long-term potentiation (LTP) plays a crucial role in memory formation and that LTP induction is modulated through GABAB autoreceptors involved in the limbic system (Davies et al., 1991). As a GABAB agonist, baclofen directly interferes with these processes. Elucidation of such GABA activations in fMRI would ideally require the absence of anaesthesia. However, sensory stimuli may still influence the cerebral activity of an anesthetized animal, allowing a pavlonian-like conditioning under moderate anaesthesia (A. Lüthi, personal communication).

In the pathways involved in recognition, the perirhinal cortex, as well as the entorhinal cortex and hippocampus occupy a crucial role (Brown and Aggleton, 2001; Wan et al., 1999). Only the first two areas were found to be activated in the present study (in addition to the already discussed auditory cortex). The following outline could provide an interpretation for such selectivity.

The perirhinal cortex is connected with the medial dorsal thalamic nucleus, while the hippocampus is connected with the anterior thalamic nucleus and the entorhinal cortex has both connections. Perirhinal and parahippocampal cortex together provide two thirds of the connections with entorhinal cortex, which is the gateway to the hippocampus.

Although perirhinal cortex and hippocampus are anatomically linked, they are not necessarily dependent on each other, as shown, for example, in their independent roles in encoding episodic information and familiarity-based recognition (Aggleton and Brown, 1999).

Studies focusing on the perirhinal cortex have shown differences in GABA transmission between temporal and entorhinal inputs including the differential activation of presynaptic GABAB receptors and differential regulation of inhibitory synaptic transmission in this region. These properties may be important in the control of neuronal activity in this region (Garden et al., 2002) and thus in its selective activation under specific stimulation.

Unfamiliar information has shown to activate selectively perirhinal and parahippocampal regions, whereas retrieval activates more hippocampus and subiculum (Gabrieli et al., 1997).

Moreover, the perirhinal cortex is strongly connected with the amygdala, a centre responsible for emotional processes. An activation in this regions upon GABAB receptor stimulation could be therefore expected, considering the amnesic and hypnotic effects observed in patients treated with other GABAB agonists, such as GHB (Teter and Guthrie, 2001).

Properties that distinguish the perirhinal cortex from the hippocampus, include parameters that could suggest why we observe an activation in these areas under our experimental conditions. The most studied memory-requiring tasks involve the visual system. However, the perirhinal cortex can receive multimodal sensory inputs (Burwell et al., 1995). For example, perirhinal/entorhinal cortex, but not hippocampus, were shown to be involved in olfaction-based recognition (Petrulis and Eichenbaum, 2003).

Recent works support an influence of baclofen on the olfactory system in vitro (Belluzzi et al., 2004; Isaacson and Vitten, 2003) and on olfactory related learning tasks in rats in vivo (Okutani et al., 2003).

Considering also the fact, that in the rodent brain, the olfactory system is more developed than in humans, the localization of CBV change in the perirhinal cortical areas of mice may be triggered by some incidence of the experimental conditions, i.e., a synergistic effect of baclofen and an olfactory stimulation coming from isoflurane under moderate hypotherma. Indeed, the pungent odour of isoflurane is a well known adverse feature of this inhalant, so that in the clinical literature it is often suggested to treat patients with other pre-medication anaesthetics, such as short acting barbiturates. Under deep narcosis, the patient is obviously not conscious of such irritant aspect of isoflurane. However, especially in the light anaesthesia of the first animal group and considering the rodent olfactory system, it is probable that the substance can induce a neural excitation in the olfactory bulbs, and thus transmit information to the linked cortical areas, in particular the perirhinal cortex. According to this hypothesis, the GABAergic modulatory effect of baclofen would induce CBV changes in this region.

A future study could look systematically at these originally unexpected factors to prove whether this effect can be avoided by switching the administration of isoflurane from the face mask to an intratracheal intubation of the animal, which, by directly reaching the bronchi, would suppress the trigger of olfactory receptors.

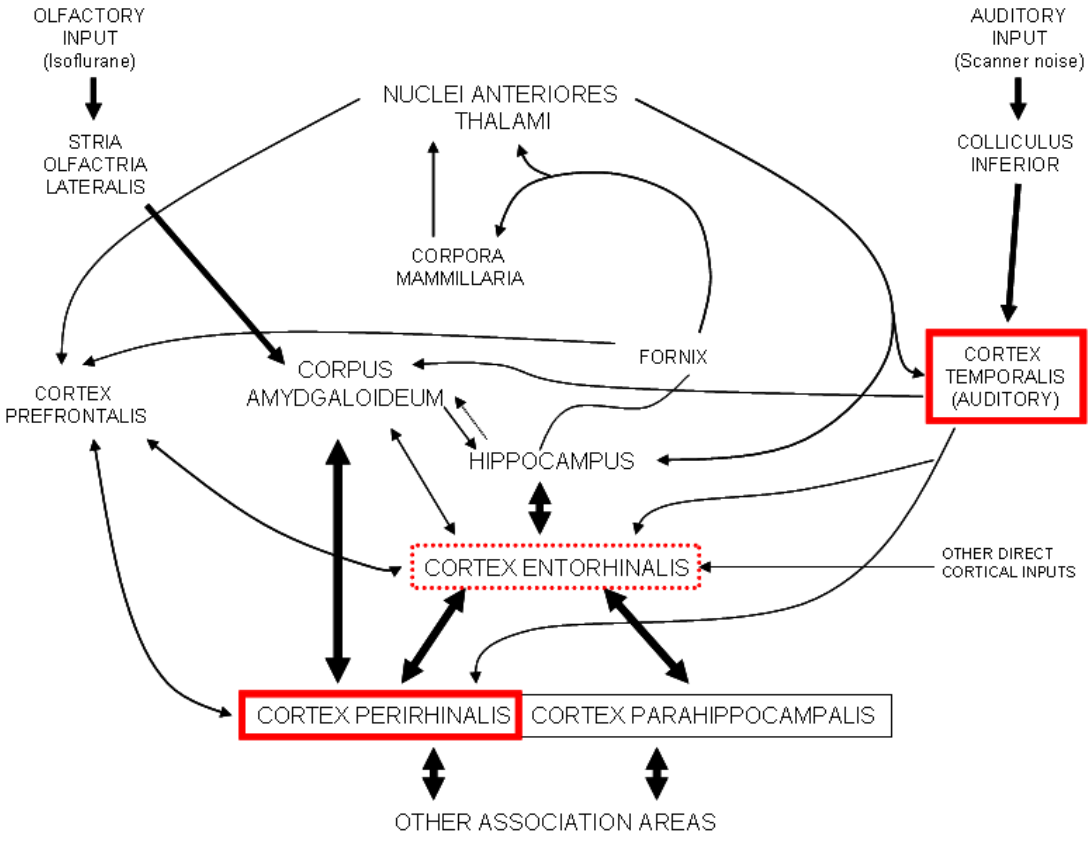


Figure 3.11 *Schematic diagram of the principal pathways underlying encoding and recollection of information in the brain*. The areas where $\Delta CBV_{rel}$ changes were observed by fMRI upon baclofen systemic administration (auditory, perirhinal, entorhinal cortex) are highlighted in red boxes. The influence of additional sensorial stimulation (olfactory, auditory) is reported over a classical diagram that relies brain structures of the limbic system involved in the encoding of episodic information and recollective aspects of recognition. The relative thickness of the lines indicates the putative importance of the connections.

## Practical Considerations for *in vivo* $^{13}$C-NMR Spectroscopy on GABAB ko Mice

*In vivo* $^{13}$C-NMR spectroscopy is much less sensitive than $^{1}$H-NMR imaging. First, the carbon atoms has 2 isotopes, 98.9 % $^{12}$C and only 1.1 % $^{13}$C. The latter is the isotope able to produce a NMR signal. This results in a much lower sensitivity, compared to the NMR signal generated from $^{1}$H. Secondly, the gyromagnetic ratio of the $^{13}$C nucleus is smaller than that of $^{1}$H, which again affects the sensitivity. Moreover, spectroscopy does not focus on the single resonance from abundant tissue water, but on the spectral dispersion of compounds that are much less concentrated in living tissue (usually < 5 mmoles/L tissue), compared to water (40 moles/L tissue).

For two types of metabolites, namely lipids and glycogen, their concentration in living tissues is sufficient to quantify differences using just the natural abundance $^{13}$C signals. In most cases, however, $^{13}$C-NMR spectroscopy of natural abundance $^{13}$C signal is not sensitive enough to differentiate minute changes in tissue metabolites (concentration usually < 5 mmoles/L tissue). In addition, the "background" $^{13}$C signals of lipids may mask the smaller signal from metabolites. Therefore, $^{13}$C NMR spectroscopy most often relies on stable isotope labelling. The molecule of interest, or a metabolic precursor, is synthesized with one or more selected carbon atoms replaced entirely by the $^{13}$C isotope. In this way, the $^{13}$C-NMR sensitivity can be increased by up to a factor $10^2$, depending on how much of the endogenous metabolite can be replaced within the tissue (= fractional enrichment). To maintain physiological conditions, the absolute tissue level of the metabolite should not change, whereas for a good NMR observation, the fractional enrichment should rapidly increases to 100% at the same time. This goal can only be achieved if the turnover rate of this molecule is very high or after longer infusion times.

The background signal from lipids, which in general changes slowly over time, is simply subtracted during the infusion of the $^{13}$C enriched compounds. In this way, the pathway and the rate of metabolism for the $^{13}$C labelled molecule can be followed throughout the catabolic (or anabolic) process. For several reasons, however, the position of the $^{13}$C label within the molecule must be chosen with care.

Carbon atoms with a short NMR $T_1$-relaxation time (e.g. methyl groups) are usually preferred over those with a longer relaxation time (e.g. carboxylic groups), in order to avoid saturation of the signal (and thus sensitivity decrease) induced by too rapid a pulsing. Indeed, to maintain an equal signal strength, carbons with a long relaxation time would require a very long repetition time ($TR > 5 \cdot T1$) between the repetitive RF pulses, which is not suitable for *in vivo* experiments.

Another factor that must be considered for the design of an appropriately labelled compound is its metabolic fate. An early “loss” of the labelled atoms in the metabolic pathways (e.g. via decarboxylation) should be avoided, in order to follow the metabolite for a sufficient number of metabolic steps. A third reason is purely technical: not every carbon position of a molecule is easily accessible for chemical labelling.

Considering the aspects mentioned above, the neurotransmitter and drugs used in the fMRI experiments were subjected to various NMR measurements and considerations in order to focus on what carbon position would be the most appropriate for *in vivo* $^{13}C$ NMR spectroscopy on mouse brains. Figure 3.12 shows the chemical structures of the compounds investigated, namely the endogenous neurotransmitter GABA (A), the medical GABA agonist baclofen (B) and the "party drug" GHB (C).

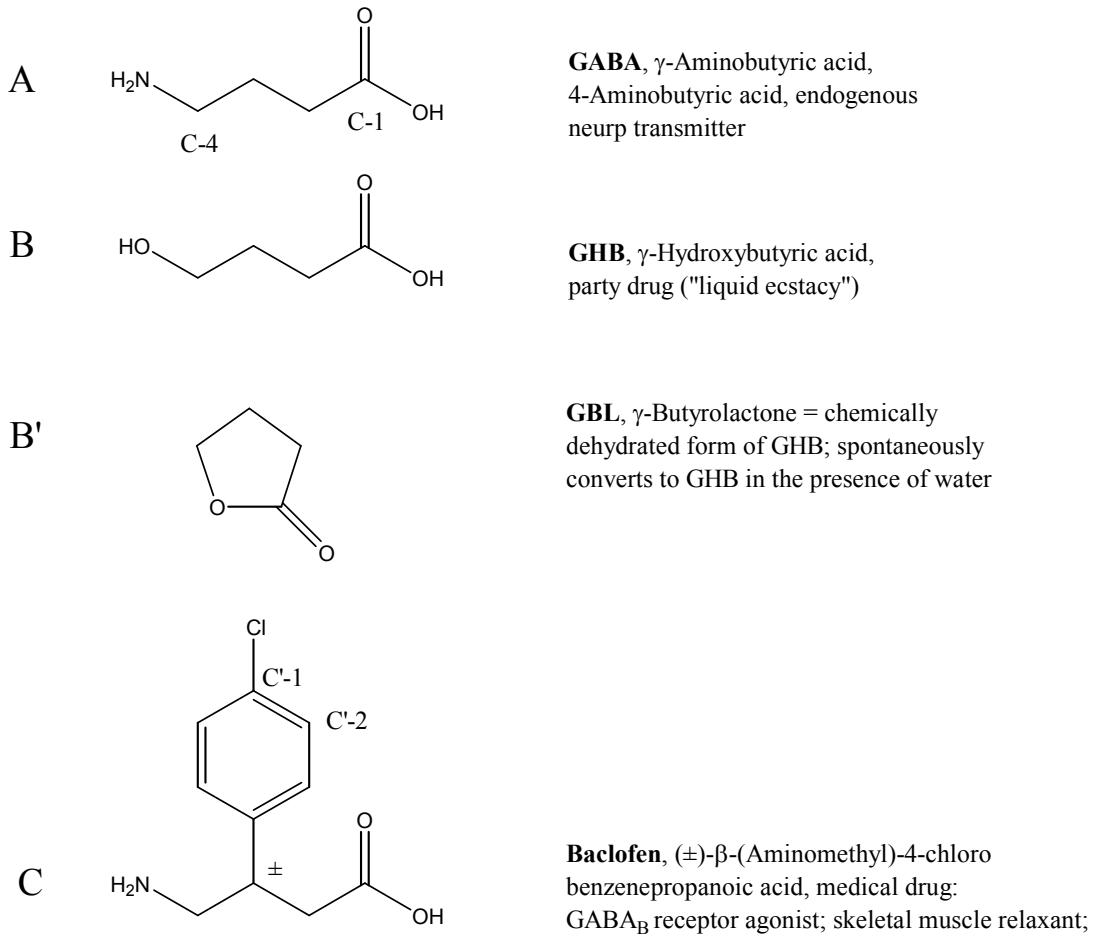


Figure 3.12. Chemical Structures of GABA and related Compounds.

Using high resolution $^{13}C$ NMR at 9.4 T, the following parameters were investigated, i.e., i) the chemical shift of the carbons with special consideration of a possible overlap with lipid resonances, ii) the effect of *in vivo* repetition times (~ 2 s) on relaxation/saturation, and iii) expected signal-to-noise ratios for a 60 min spectrum. The latter factor is based on the assumption that for a mouse of 30 g body weight, doses of GHB and baclofen of not more than 60 µg and 1.35 mg, respectively, can be administered because of the toxicity of the compounds. Indeed, the LD50 is 2 mg/kg (i.v.; male rats) and 45 mg/kg (i.v.; male mice) for GHB and baclofen, respectively (data from The Merck Index 12$^{th}$ ed.). In the case of baclofen, the dose used in our fMRI experiments was ~ 5 mg / kg mouse, and presented already toxic effects in few cases. For the evaluation of the signal-to-noise in a realistic *in vivo* MRS experiment (repetition time of 2s and 2000 scans), the effective amount of baclofen

present in the mouse brain has to be considered, which would be a small percentage (≤ 2-4% of the body volume) of the total amount injected. This would correspond to ~ 6 µg baclofen for an injection of 5 mg/kg body weight into a 30 g mouse. For $^{13}$C-MRS, 6 µg baclofen enriched with $^{13}$C to 100% would correspond to an equal amount of $^{13}$C present in ~ 0.6 mg of natural abundance baclofen (at only 1.1% fractional enrichment). The latter amount of non-enriched compound was therefore chosen for *in vitro* $^{13}$C-NMR spectroscopy, as shown in Fig. 3.10.

From a metabolic view, positions 2 to 4 are much more appropriate to be labelled, because the position C-1 can undergo rapid decarboxylation. Figure 3.10 C) also illustrates that under usual *in vivo* spectral conditions (repetition time = 2 s), the carboxylic C-1 is highly saturated and the signal-to-noise is much worse than for all other carbons. Although recorded at 9.4 Tesla (and not at 7 Tesla as in the *in vivo* magnet), these spectra give a good estimate for the expected signal-to-noise at 7 Tesla. Labelling the position C-1 for *in vivo* experiments is inappropriate for a third reason: the carboxylic C-1 group of all compounds in Figure 3.10 overlaps with the carboxylic resonances of lipids (175-185 ppm). Slight changes in the lipid composition during the experimental time might cause severe artifacts when subtracting NMR spectra before and after the infusion. An overlap with the lipid resonances at 22-32 ppm (-CH2-) and 55-65 ppm (glycerol backbone and N-(CH3)3 groups) is also expected for the C-3 of all compounds and the C-4 of GHB, respectively, so that positions C-2 (eventually C-4) seems to be the most appropriate position to be labelled for *in vivo* $^{13}$C spectroscopy.

Despite these obvious disadvantages to label position C-1 for *in vivo* NMR spectroscopy, C-1 is the easiest position to label from a chemical point of view.

## 3.5 Conclusion

In the present study, fMRI could be successfully applied to *in vivo* measurements of mice. Baclofen-induced changes in cerebral blood volume ($CBV_{rel}$) were detected in healthy mice *in vivo*. The CBV changes were localized in the auditory and perirhinal brain regions and might reflect the baclofen-enhanced response to sensorial (auditory and olfactory) stimuli.

Several conclusions can be drawn, i.e., i) functional information can be obtained from fMRI in mice; ii) monitoring and stabilization of physiological conditions is of fundamental importance in such experiments for the appropriate evaluation of cerebral hemodynamic responses; iii) concomitant sensory stimulations can influence the localization of hemodynamic changes. This is an important aspect for the choice of new technical methods in the study of systemic pharmacological compounds acting on a wide area of the CNS, and especially with pharmaca that induce sensorial alterations, such as baclofen or GHB.

# References


Aggleton, J.P. and Brown, M.W. (1999) Episodic memory, amnesia, and the hippocampal-anterior thalamic axis. *Behav Brain Sci*, **22**, 425-444; discussion 444-489.

Albert, M.S., Cates, G.D., Driehuys, B., Happer, W., Saam, B., Springer, C.S. and Wishnia, A. (1994) Biological Magnetic-Resonance-Imaging Using Laser Polarized Xe-129. *Nature*, **370**, 199-201.

Aliautdin, R.N., Kreuter, J. and Kharkevich, D.A. (2003) [Drug delivery to the brain with nanoparticles]. *Eksp Klin Farmakol*, **66**, 65-68.

Ambudkar, S.V., Cardarelli, C.O., Pashinsky, I. and Stein, W.D. (1997) Relation between the turnover number for vinblastine transport and for vinblastine-stimulated ATP hydrolysis by human P-glycoprotein. *J Biol Chem*, **272**, 21160-21166.

Ambudkar, S.V., Dey, S., Hrycyna, C.A., Ramachandra, M., Pastan, I. and Gottesman, M.M. (1999) Biochemical, cellular, and pharmacological aspects of the multidrug transporter. *Annual Review of Pharmacology and Toxicology*, **39**, 361-398.

Aronica, E., Gorter, J.A., Jansen, G.H., van Veelen, C.W., van Rijen, P.C., Leenstra, S., Ramkema, M., Scheffer, G.L., Scheper, R.J. and Troost, D. (2003) Expression and cellular distribution of multidrug transporter proteins in two major causes of medically intractable epilepsy: focal cortical dysplasia and glioneuronal tumors. *Neuroscience*, **118**, 417-429.

Banerjee, S.K., Jagannath, C., Hunter, R.L. and Dasgupta, A. (2000) Bioavailability of tobramycin after oral delivery in FVB mice using CRL-1605 copolymer, an inhibitor of P-glycoprotein. *Life Sci*, **67**, 2011-2016.

Batrakova, E., Lee, S., Li, S., Venne, A., Alakhov, V. and Kabanov, A. (1999) Fundamental relationships between the composition of pluronic block copolymers and their hypersensitization effect in MDR cancer cells. *Pharm Res*, **16**, 1373-1379.

Batrakova, E.V., Li, S., Alakhov, V.Y., Miller, D.W. and Kabanov, A.V. (2003) Optimal structure requirements for pluronic block copolymers in modifying P-glycoprotein drug efflux transporter activity in bovine brain microvessel endothelial cells. *J Pharmacol Exp Ther*, **304**, 845-854.

Batrakova, E.V., Li, S., Elmquist, W.F., Miller, D.W., Alakhov, V.Y. and Kabanov, A.V. (2001) Mechanism of sensitization of MDR cancer cells by Pluronic block copolymers: Selective energy depletion. *Br J Cancer*, **85**, 1987-1997.

Batrakova, E.V., Li, S., Vinogradov, S.V., Alakhov, V.Y., Miller, D.W. and Kabanov, A.V. (2001) Mechanism of pluronic effect on P-glycoprotein efflux system in blood-brain barrier: contributions of energy depletion and membrane fluidization. *J Pharmacol Exp Ther*, **299**, 483-493.

Beck, W.T. (1989) Unknotting the Complexities of Multidrug Resistance - the Involvement of DNA Topoisomerases in Drug-Action and Resistance. *Journal of the National Cancer Institute*, **81**, 1683-1685.

Beckmann, N., Mueggler, T., Allegrini, P.R., Laurent, D. and Rudin, M. (2001) From anatomy to the target: contributions of magnetic resonance imaging to preclinical pharmaceutical research. *Anat.Rec.2001.Apr15.;265.(2.):85.-100.*, **265**, 85-100.

Belliveau, J.W., Kennedy, D.N., Jr, McKinstry, R.C., Buchbinder, B.R., Weisskoff, R.M., Cohen, M.S., Vevea, J.M., Brady, T.J. and Rosen, B.R. (1991) Functional mapping of the human visual cortex by magnetic resonance imaging. *Science*, **254**, 716-719.

Belliveau, J.W., Rosen, B.R., Kantor, H.L., Rzedzian, R.R., Kennedy, D.N., McKinstry, R.C., Vevea, J.M., Cohen, M.S., Pykett, I.L. and Brady, T.J. (1990) Functional cerebral imaging by susceptibility-contrast NMR. *Magn.Reson.Med.*, **14**, 538-546.

Belluzzi, O., Puopolo, M., Benedusi, M. and Kratskin, I. (2004) Selective neuroinhibitory effects of taurine in slices of rat main olfactory bulb. *Neuroscience*, **124**, 929-944.

Belting, M. (2003) Heparan sulfate proteoglycan as a plasma membrane carrier. *Trends Biochem Sci*, **28**, 145-151.

Benet, L.Z., Izumi, T., Zhang, Y., Silverman, J.A. and Wacher, V.J. (1999) Intestinal MDR transport proteins and P-450 enzymes as barriers to oral drug delivery. *J Control Release*, **62**, 25-31.

Bennett, R.P., Dalby, B. and Guy, P.M. (2002) Protein delivery using VP22. *Nat Biotechnol*, **20**, 20.

Biedler, J.L. and Riehm, H. (1970) Cellular Resistance to Actinomycin-D in Chinese Hamster Cells in-Vitro - Cross-Resistance, Radioautographic, and Cytogenetic Studies. *Cancer Research*, **30**, 1174-&.

Bittner, B., Guenzi, A., Fullhardt, P., Zuercher, G., Gonzalez, R.C. and Mountfield, R.J. (2002) Improvement of the bioavailability of colchicine in rats by co-administration of D-alpha-tocopherol polyethylene glycol 1000 succinate and a polyethoxylated derivative of 12-hydroxy-stearic acid. *Arzneimittelforschung*, **52**, 684-688.

Bloch, F. (1946) Nuclear Induction. *Physical Review*, **70**, 460-474.

Bloch, F., Hansen, W.W. and Packard, M. (1946) Nuclear Induction. *Physical Review*, **69**, 680-680.

Bloch, F., Hansen, W.W. and Packard, M. (1946) The Nuclear Induction Experiment. *Physical Review*, **70**, 474-485.

Bogman, K., Erne-Brand, F., Alsenz, J. and Drewe, J. (2003) The role of surfactants in the reversal of active transport mediated by multidrug resistance proteins. *J Pharm Sci*, **92**, 1250-1261.

Boxerman, J.L., Hamberg, L.M., Rosen, B.R. and Weisskoff, R.M. (1995) MR contrast due to intravascular magnetic susceptibility perturbations. *Magn.Reson.Med.*, **34**, 555-566.

Brinker, G., Bock, C., Busch, E., Krep, H., Hossmann, K.A. and Hoehn-Berlage, M. (1999) Simultaneous recording of evoked potentials and T2*-weighted MR images during somatosensory stimulation of rat. *Magn.Reson.Med.*, **41**, 469-473.

Brouillette, J. and Couture, R. (2002) Evidence for a GABA(B) receptor component in the spinal action of Substance P (SP) on arterial blood pressure in the awake rat. *Br J Pharmacol*, **136**, 1169-1177.

Brown, M.W. and Aggleton, J.P. (2001) Recognition memory: what are the roles of the perirhinal cortex and hippocampus? *Nat Rev Neurosci*, **2**, 51-61.

Buckingham, L.E., Balasubramanian, M., Safa, A.R., Shah, H., Komarov, P., Emanuele, R.M. and Coon, J.S. (1996) Reversal of multi-drug resistance in vitro by fatty acid-PEG-fatty acid diesters. *Int J Cancer*, **65**, 74-79.

Burkert, U. and Allinger, N.L. (1982) Molecular Mechanics. In *ACS Monograph 177*. American Chemical Society, Washington DC.

Burwell, R.D., Witter, M.P. and Amaral, D.G. (1995) Perirhinal and postrhinal cortices of the rat: a review of the neuroanatomical literature and comparison with findings from the monkey brain. *Hippocampus*, **5**, 390-408.

Buxton, R.B. (2002) *Introduction to functional magnetic resonance imaging: Principles and techniques*. Cambridge University Press, Cambridge.

Cai, J. and Gros, P. (2003) Overexpression, purification, and functional characterization of ATP-binding cassette transporters in the yeast, Pichia pastoris. *Biochimica Et Biophysica Acta-Biomembranes*, **1610**, 63-76.

Cardarelli, C.O., Aksentijevich, I., Pastan, I. and Gottesman, M.M. (1995) Differential-Effects of P-Glycoprotein Inhibitors on Nih3t3 Cells Transfected with Wild-Type (G185) or Mutant (V185) Multidrug Transporters. *Cancer Research*, **55**, 1086-1091.

Carey, D.J., Stahl, R.C., Tucker, B., Bendt, K.A. and Cizmecismith, G. (1994) Aggregation-Induced Association of Syndecan-1 with Microfilaments Mediated by the Cytoplasmic Domain. *Experimental Cell Research*, **214**, 12-21.

Chahl, L.A. and Walker, S.B. (1980) The effect of baclofen on the cardiovascular system of the rat. *Br J Pharmacol*, **69**, 631-637.

Chapman, B., Turner, R., Ordidge, R.J., Doyle, M., Cawley, M., Coxon, R., Glover, P. and Mansfield, P. (1987) Real-time movie imaging from a single cardiac cycle by NMR. *Magn Reson Med*, **5**, 246-254.

Chen, C.J., Chin, J.E., Ueda, K., Clark, D.P., Pastan, I., Gottesman, M.M. and Roninson, I.B. (1986) Internal Duplication and Homology with Bacterial Transport Proteins in the Mdr1 (P-Glycoprotein) Gene from Multidrug-Resistant Human-Cells. *Cell*, **47**, 381-389.

Chen, Y.C., Mandeville, J.B., Nguyen, T.V., Talele, A., Cavagna, F. and Jenkins, B.G. (2001) Improved mapping of pharmacologically induced neuronal activation using the IRON technique with superparamagnetic blood pool agents. *J Magn Reson Imaging 2001.Nov.;14.(5.):517.-24.*, **14**, 517-524.

Clavel, F., Guyader, M., Guetard, D., Salle, M., Montagnier, L. and Alizon, M. (1986) Molecular cloning and polymorphism of the human immune deficiency virus type 2. *Nature*, **324**, 691-695.

Cole, S.P.C., Bhardwaj, G., Gerlach, J.H., Mackie, J.E., Grant, C.E., Almquist, K.C., Stewart, A.J., Kurz, E.U., Duncan, A.M.V. and Deeley, R.G. (1992) Overexpression of a Transporter Gene in a Multidrug-Resistant Human Lung-Cancer Cell-Line. *Science*, **258**, 1650-1654.

Cole, S.P.C., Sparks, K.E., Fraser, K., Loe, D.W., Grant, C.E., Wilson, G.M. and Deeley, R.G. (1994) Pharmacological Characterization of Multidrug-Resistant Mrp-Transfected Human Tumor-Cells. *Cancer Research*, **54**, 5902-5910.

Console, S., Marty, C., Garcia-Echeverria, C., Schwendener, R. and Ballmer-Hofer, K. (2003) Antennapedia and HIV transactivator of transcription (TAT) "protein transduction domains" promote endocytosis of high molecular weight cargo upon binding to cell surface glycosaminoglycans. *J Biol Chem*, **278**, 35109-35114.

Cornaire, G., Woodley, J.F., Saivin, S., Legendre, J.Y., Decourt, S., Cloarec, A. and Houin, G. (2000) Effect of polyoxyl 35 castor oil and Polysorbate 80 on the intestinal absorption of digoxin in vitro. *Arzneimittelforschung*, **50**, 576-579.

Daikhin, Y. and Yudkoff, M. (1998) Ketone bodies and brain glutamate and GABA metabolism. *Dev Neurosci*, **20**, 358-364.

Damadian, R. (1971) Tumor Detection by Nuclear Magnetic Resonance. *Science*, **171**, 1151-&.

Davies, C.H., Starkey, S.J., Pozza, M.F. and Collingridge, G.L. (1991) GABA autoreceptors regulate the induction of LTP. *Nature*, **349**, 609-611.

Derossi, D., Calvet, S., Trembleau, A., Brunissen, A., Chassaing, G. and Prochiantz, A. (1996) Cell internalization of the third helix of the antennapedia homeodomain is receptor-independent. *Journal of Biological Chemistry*, **271**, 18188-18193.

Derossi, D., Chassaing, G. and Prochiantz, A. (1998) Trojan peptides: the penetratin system for intracellular delivery. *Trends in Cell Biology*, **8**, 84-87.

Derossi, D., Joliot, A.H., Chassaing, G. and Prochiantz, A. (1994) The third helix of the Antennapedia homeodomain translocates through biological membranes. *J Biol Chem*, **269**, 10444-10450.

Descoteaux, S., Ayala, P., Orozco, E. and Samuelson, J. (1992) Primary sequences of two P-glycoprotein genes of Entamoeba histolytica. *Mol Biochem Parasitol*, **54**, 201-211.

Dey, S., Ramachandra, M., Pastan, I., Gottesman, M.M. and Ambudkar, S.V. (1997) Evidence for two nonidentical drug-interaction sites in the human P-glycoprotein. *Proceedings of the National Academy of Sciences of the United States of America*, **94**, 10594-10599.

Dijkhuizen, R.M., JM, R., Mandeville, J.B., Marota, J., BR, R. and SP, F. (2000) Functional MRI of reorganisation in rat brain after stroke. In *Proccedings of the 8th Annual Meeting of ISMRM*, Denver, p. 282.

Dinkel, A., Aicher, W.K., Warnatz, K., Burki, K., Eibel, H. and Ledermann, B. (1999) Efficient generation of transgenic BALB/c mice using BALB/c embryonic stem cells. *J Immunol Methods*, **223**, 255-260.

Dintaman, J.M. and Silverman, J.A. (1999) Inhibition of P-glycoprotein by D-alpha-tocopheryl polyethylene glycol 1000 succinate (TPGS). *Pharm Res*, **16**, 1550-1556.

Doige, C.A., Yu, X. and Sharom, F.J. (1993) The effects of lipids and detergents on ATPase-active P-glycoprotein. *Biochim Biophys Acta*, **1146**, 65-72.

Dumoulin, C.L., Souza, S.P. and Feng, H. (1987) Multiecho Magnetic-Resonance Angiography. *Magnetic Resonance in Medicine*, **5**, 47-57.

Dumoulin, C.L., Souza, S.P. and Hart, H.R. (1987) Rapid Scan Magnetic-Resonance Angiography. *Magnetic Resonance in Medicine*, **5**, 238-245.

Edelstein, W.A., Hutchison, J.M.S., Johnson, G. and Redpath, T. (1980) Spin Warp NMR Imaging and Applications to Human Whole-Body Imaging. *Physics in Medicine and Biology*, **25**, 751-756.

Edelstein, W.A., Hutchison, J.M.S., Ling, C.R., Foster, M.A., Johnson, G. and Mallard, J.R. (1980) An NMR Whole-Body Imaging Machine and NMR-Studies of Tissue In vitro. *Physics in Medicine and Biology*, **25**, 776-776.

Eguchi, A., Akuta, T., Okuyama, H., Senda, T., Yokoi, H., Inokuchi, H., Fujita, S., Hayakawa, T., Takeda, K., Hasegawa, M. and Nakanishi, M. (2001) Protein transduction domain of HIV-1 Tat protein promotes efficient delivery of DNA into mammalian cells. *J Biol Chem*, **276**, 26204-26210.

Ekins, S., Kim, R.B., Leake, B.F., Dantzig, A.H., Schuetz, E.G., Lan, L.B., Yasuda, K., Shepard, R.L., Winter, M.A., Schuetz, J.D., Wikel, J.H. and Wrighton, S.A. (2002) Three-dimensional quantitative structure-activity relationships of inhibitors of P-glycoprotein. *Mol Pharmacol*, **61**, 964-973.

Endicott, J.A. and Ling, V. (1989) The Biochemistry of P-Glycoprotein-Mediated Multidrug Resistance. *Annual Review of Biochemistry*, **58**, 137-171.

Fawell, S., Seery, J., Daikh, Y., Moore, C., Chen, L.L., Pepinsky, B. and Barsoum, J. (1994) Tat-Mediated Delivery of Heterologous Proteins into Cells. *Proceedings of the National Academy of Sciences of the United States of America*, **91**, 664-668.

Fischer, H., Gottschlich, R. and Seelig, A. (1998) Blood-brain barrier permeation: Molecular parameters governing passive diffusion. *Journal of Membrane Biology*, **165**, 201-211.

Fischer, H., Seelig, A., Beier, N., Raddatz, P. and Seelig, J. (1999) New drugs for the Na+/H+ exchanger. Influence of Na+ concentration and determination of inhibition constants with a microphysiometer. *Journal of Membrane Biology*, **168**, 39-45.

Ford, J.M. and Hait, W.N. (1990) Pharmacology of drugs that alter multidrug resistance in cancer. *Pharmacol Rev*, **42**, 155-199.

Frankel, A.D. and Pabo, C.O. (1988) Cellular uptake of the tat protein from human immunodeficiency virus. *Cell*, **55**, 1189-1193.

Frankel, A.D. and Pabo, C.O. (1988) Fingering Too Many Proteins. *Cell*, **53**, 675-675.

Friche, E., Jensen, P.B., Sehested, M., Demant, E.J. and Nissen, N.N. (1990) The solvents cremophor EL and Tween 80 modulate daunorubicin resistance in the multidrug resistant Ehrlich ascites tumor. *Cancer Commun*, **2**, 297-303.

Gabrieli, J.D., Brewer, J.B., Desmond, J.E. and Glover, G.H. (1997) Separate neural bases of two fundamental memory processes in the human medial temporal lobe. *Science*, **276**, 264-266.

Garden, D.L., Kemp, N. and Bashir, Z.I. (2002) Differences in GABAergic transmission between two inputs into the perirhinal cortex. *Eur J Neurosci*, **16**, 437-444.

Garroway, A.N., Grannell, P.K. and Mansfield, P. (1974) Image-Formation in NMR by a Selective Irradiative Process. *Journal of Physics C-Solid State Physics*, **7**, L457-L462.

Gebhardt, R., Bellemann, P. and Mecke, D. (1978) Metabolic and Enzymatic Characteristics of Adult Rat-Liver Parenchymal-Cells in Non-Proliferating Primary Monolayer-Cultures. *Experimental Cell Research*, **112**, 431-441.

Gelderblom, H., Verweij, J., Nooter, K. and Sparreboom, A. (2001) Cremophor EL: the drawbacks and advantages of vehicle selection for drug formulation. *Eur J Cancer*, **37**, 1590-1598.

Gerlach, J.H., Kartner, N., Bell, D.R. and Ling, V. (1986) Multidrug Resistance. *Cancer Surveys*, **5**, 25-46.

Gottesman, M.M. (2003) Cancer gene therapy: an awkward adolescence. *Cancer Gene Therapy*, **10**, 501-508.

Gottesman, M.M. and Pastan, I. (1993) Biochemistry of Multidrug-Resistance Mediated by the Multidrug Transporter. *Annual Review of Biochemistry*, **62**, 385-427.

Green, M., Loewenstein, P.M., Pusztai, R. and Symington, J.S. (1988) An Adenovirus E1a-Protein Domain Activates Transcription Invivo and Invitro in the Absence of Protein-Synthesis. *Cell*, **53**, 921-926.

Gros, P., Croop, J. and Housman, D. (1986) Mammalian Multidrug Resistance Gene - Complete Cdna Sequence Indicates Strong Homology to Bacterial Transport Proteins. *Cell*, **47**, 371-380.

Gros, P., Croop, J., Roninson, I., Varshavsky, A. and Housman, D.E. (1986) Isolation and Characterization of DNA-Sequences Amplified in Multidrug-Resistant Hamster-Cells. *Proceedings of the National Academy of Sciences of the United States of America*, **83**, 337-341.

Gyngell, M.L., Bock, C., Schmitz, B., Hoehn-Berlage, M. and Hossmann, K.A. (1996) Variation of functional MRI signal in response to frequency of somatosensory stimulation in alpha-chloralose anesthetized rats. *Magn.Reson.Med.*, **36**, 13-15.

Hafeman, D.G., Parce, J.W. and Mcconnell, H.M. (1988) Light-Addressable Potentiometric Sensor for Biochemical Systems. *Science*, **240**, 1182-1185.

Hallbrink, M., Floren, A., Elmquist, A., Pooga, M., Bartfai, T. and Langel, U. (2001) Cargo delivery kinetics of cell-penetrating peptides. *Biochimica Et Biophysica Acta-Biomembranes*, **1515**, 101-109.

Hamberg, L.M., Boccalini, P., Stranjalis, G., Hunter, G.J., Huang, Z., Halpern, E., Weisskoff, R.M., Moskowitz, M.A. and Rosen, B.R. (1996) Continuous assessment of relative cerebral blood volume in transient ischemia using steady state susceptibility-contrast MRI. *Magn.Reson.Med.*, **35**, 168-173.

Heerklotz, H. and Seelig, J. (2000) Correlation of membrane/water partition coefficients of detergents with the critical micelle concentration. *Biophys J*, **78**, 2435-2440.

Herbert, H., Aschoff, A. and Ostwald, J. (1991) Topography of projections from the auditory cortex to the inferior colliculus in the rat. *J Comp Neurol*, **304**, 103-122.

Higgins, C.F. (1994) Flip-Flop - the Transmembrane Translocation of Lipids. *Cell*, **79**, 393-395.

Ho, A., Schwarze, S.R., Mermelstein, S.J., Waksman, G. and Dowdy, S.F. (2001) Synthetic protein transduction domains: Enhanced transduction potential in vitro and in vivo. *Cancer Research*, **61**, 474-477.

Hoehn, M., Nicolay, K., Franke, C. and van, d.S. (2001) Application of magnetic resonance to animal models of cerebral ischemia. *J Magn Reson Imaging 2001.Nov.;14.(5.):491.-509.*, **14**, 491-509.

Hollo, Z., Homolya, L., Davis, C.W. and Sarkadi, B. (1994) Calcein accumulation as a fluorometric functional assay of the multidrug transporter. *Biochim Biophys Acta*, **1191**, 384-388.

Howard, E.M., Zhang, H. and Roepe, P.D. (2002) A novel transporter, Pfcrt, confers antimalarial drug resistance. *J Membr Biol*, **190**, 1-8.

Hugger, E.D., Audus, K.L. and Borchardt, R.T. (2002) Effects of poly(ethylene glycol) on efflux transporter activity in Caco-2 cell monolayers. *J Pharm Sci*, **91**, 1980-1990.

Hugger, E.D., Novak, B.L., Burton, P.S., Audus, K.L. and Borchardt, R.T. (2002) A comparison of commonly used polyethoxylated pharmaceutical excipients on their ability to inhibit P-glycoprotein activity in vitro. *J Pharm Sci*, **91**, 1991-2002.

Hutchison, J.M.S., Edelstein, W.A. and Johnson, G. (1980) A Whole-Body NMR Imaging Machine. *Journal of Physics E-Scientific Instruments*, **13**, 947-955.

Hyder, F., Behar, K.L., Martin, M.A., Blamire, A.M. and Shulman, R.G. (1994) Dynamic magnetic resonance imaging of the rat brain during forepaw stimulation. *J.Cereb.Blood Flow Metab.*, **14**, 649-655.

Isaacson, J.S. and Vitten, H. (2003) GABA(B) receptors inhibit dendrodendritic transmission in the rat olfactory bulb. *J Neurosci*, **23**, 2032-2039.

Ishihara, M., Fedarko, N.S. and Conrad, H.E. (1986) Transport of heparan sulfate into the nuclei of hepatocytes. *J Biol Chem*, **261**, 13575-13580.

Jagannath, C., Wells, A., Mshvildadze, M., Olsen, M., Sepulveda, E., Emanuele, M., Hunter, R.L., Jr. and Dasgupta, A. (1999) Significantly improved oral uptake of amikacin in FVB mice in the presence of CRL-1605 copolymer. *Life Sci*, **64**, 1733-1738.

Johnson, B.M., Charman, W.N. and Porter, C.J. (2002) An in vitro examination of the impact of polyethylene glycol 400, Pluronic P85, and vitamin E d-alpha-tocopheryl polyethylene glycol 1000 succinate on P-glycoprotein efflux and enterocyte-based metabolism in excised rat intestine. *AAPS PharmSci*, **4**, 40.

Juliano, R., Ling, V. and Graves, J. (1976) Drug-Resistant Mutants of Chinese-Hamster Ovary Cells Possess an Altered Cell-Surface Carbohydrate Component. *Journal of Supramolecular Structure*, **4**, 521-526.

Juliano, R.L. and Ling, V. (1976) A surface glycoprotein modulating drug permeability in Chinese hamster ovary cell mutants. *Biochim Biophys Acta*, **455**, 152-162.

Kabanov, A.V., Batrakova, E.V. and Alakhov, V.Y. (2002) Pluronic block copolymers for overcoming drug resistance in cancer. *Adv Drug Deliv Rev*, **54**, 759-779.

Kabanov, A.V., Batrakova, E.V. and Miller, D.W. (2003) Pluronic block copolymers as modulators of drug efflux transporter activity in the blood-brain barrier. *Adv Drug Deliv Rev*, **55**, 151-164.

Kabanov, A.V., Slepnev, V.I., Kuznetsova, L.E., Batrakova, E.V., Alakhov, V., Melik-Nubarov, N.S., Sveshnikov, P.G. and Kabanov, V.A. (1992) Pluronic micelles as a tool for low-molecular compound vector delivery into a cell: effect of Staphylococcus aureus enterotoxin B on cell loading with micelle incorporated fluorescent dye. *Biochem Int*, **26**, 1035-1042.

Karn, J. (1999) Tackling Tat. *J Mol Biol*, **293**, 235-254.

Kartner, N., Riordan, J.R. and Ling, V. (1983) Cell-Surface P-Glycoprotein Associated with Multidrug Resistance in Mammalian-Cell Lines. *Science*, **221**, 1285-1288.

Kaupmann, K., Huggel, K., Heid, J., Flor, P.J., Bischoff, S., Mickel, S.J., McMaster, G., Angst, C., Bittiger, H., Froestl, W. and Bettler, B. (1997) Expression cloning of GABA(B) receptors uncovers similarity to metabotropic glutamate receptors. *Nature*, **386**, 239-246.

Kerr, K.M., Sauna, Z.E. and Ambudkar, S.V. (2001) Correlation between steady-state ATP hydrolysis and vanadate-induced ADP trapping in Human P-glycoprotein. Evidence for ADP release as the rate-limiting step in the catalytic cycle and its modulation by substrates. *J Biol Chem*, **276**, 8657-8664.

Kerr, K.M., Sauna, Z.E. and Ambudkar, S.V. (2001) Correlation between steady-state ATP hydrolysis and vanadate-induced ADP trapping in Human P-glycoprotein. Evidence for ADP release as the rate-limiting step in the catalytic cycle and its modulation by substrates. *J Biol Chem*, **276**, 8657-8664.

Kerskens, C.M., Hoehn-Berlage, M., Schmitz, B., Busch, E., Bock, C., Gyngell, M.L. and Hossmann, K.A. (1996) Ultrafast perfusion-weighted MRI of functional brain activation in rats during forepaw stimulation: comparison with T2 -weighted MRI. *NMR.Biomed.*, **9**, 20-23.

Komarov, P.G., Shtil, A.A., Buckingham, L.E., Balasubramanian, M., Piraner, O., Emanuele, R.M., Roninson, I.B. and Coon, J.S. (1996) Inhibition of cytarabine-induced MDR1 (P-glycoprotein) gene activation in human tumor cells by fatty acid-polyethylene glycol-fatty acid diesters, novel inhibitors of P-glycoprotein function. *Int J Cancer*, **68**, 245-250.

Kontoyiannis, D.P. and Lewis, R.E. (2002) Antifungal drug resistance of pathogenic fungi. *Lancet*, **359**, 1135-1144.

Kramer, S.D. and Wunderli-Allenspach, H. (2003) No entry for TAT(44-57) into liposomes and intact MDCK cells: novel approach to study membrane permeation of cell-penetrating peptides. *Biochimica Et Biophysica Acta-Biomembranes*, **1609**, 161-169.

Kreuter, J. (2001) Nanoparticulate systems for brain delivery of drugs. *Adv Drug Deliv Rev*, **47**, 65-81.

Kumar, A., Welti, D. and Ernst, R.R. (1975) Imaging of Macroscopic Objects by NMR Fourier Zeugmatography. *Naturwissenschaften*, **62**, 34-34.

Kumar, A., Welti, D. and Ernst, R.R. (1975) NMR Fourier Zeugmatography. *Journal of Magnetic Resonance*, **18**, 69-83.

Kwong, K.K., Belliveau, J.W., Chesler, D.A., Goldberg, I.E., Weisskoff, R.M., Poncelet, B.P., Kennedy, D.N., Hoppel, B.E., Cohen, M.S. and Turner, R. (1992) Dynamic magnetic resonance imaging of human brain activity during primary sensory stimulation. *Proc.Natl.Acad.Sci.U.S.A.*, **89**, 5675-5679.

Landulpho, C.D., Dias, A.C. and Colombari, E. (2003) Cardiovascular mechanisms activated by microinjection of baclofen into NTS of conscious rats. *Am J Physiol Heart Circ Physiol*, **284**, H987-993.

Landwojtowicz, E., Nervi, P. and Seelig, A. (2002) Real-time monitoring of P-glycoprotein activation in living cells. *Biochemistry*, **41**, 8050-8057.

Landwojtowicz, E., Nervi, P. and Seelig, A. (2002) Real-time monitoring of P-glycoprotein activation in living cells. *Biochemistry*, **submitted**.

Laspia, M.F., Rice, A.P. and Mathews, M.B. (1989) HIV-1 Tat protein increases transcriptional initiation and stabilizes elongation. *Cell*, **59**, 283-292.

Lauterbur, P.C. (1973) Image Formation by Induced Local Interactions - Examples Employing Nuclear Magnetic-Resonance. *Nature*, **242**, 190-191.

Levitt, M.H. (2001) *Spin Dynamics - Basic of Nuclear Magnetic Resonance*. John Wiley & Sons, LTD, New York.

Lewin, M., Carlesso, N., Tung, C.H., Tang, X.W., Cory, D., Scadden, D.T. and Weissleder, R. (2000) Tat peptide-derivatized magnetic nanoparticles allow in vivo tracking and recovery of progenitor cells. *Nat Biotechnol*, **18**, 410-414.

Liminga, G., Jonsson, B., Nygren, P. and Larsson, R. (1999) On the mechanism underlying calcein-induced cytotoxicity. *Eur J Pharmacol*, **383**, 321-329.

Lindgren, M., Hallbrink, M., Prochiantz, A. and Langel, U. (2000) Cell-penetrating peptides. *Trends in Pharmacological Sciences*, **21**, 99-103.

Lindsay, M.A. (2002) Peptide-mediated cell delivery: application in protein target validation. *Curr Opin Pharmacol*, **2**, 587-594.

Lingenhoehl, K., Brom, R., Heid, J., Beck, P., Froestl, W., Kaupmann, K., Bettler, B. and Mosbacher, J. (1999) Gamma-hydroxybutyrate is a weak agonist at recombinant GABA(B) receptors. *Neuropharmacology*, **38**, 1667-1673.

Linhardt, R.J., Turnbull, J.E., Wang, H.M., Loganathan, D. and Gallagher, J.T. (1990) Examination of the Substrate-Specificity of Heparin and Heparan-Sulfate Lyases. *Biochemistry*, **29**, 2611-2617.

Litman, T., Nielsen, D., Skovsgaard, T., Zeuthen, T. and Stein, W.D. (1997) ATPase activity of P-glycoprotein related to emergence of drug resistance in Ehrlich ascites tumor cell lines. *Biochimica Et Biophysica Acta-Molecular Basis of Disease*, **1361**, 147-158.

Litman, T., Zeuthen, T., Skovsgaard, T. and Stein, W.D. (1997) Structure-activity relationships of P-glycoprotein interacting drugs: kinetic characterization of their effects on ATPase activity. *Biochimica Et Biophysica Acta-Molecular Basis of Disease*, **1361**, 159-168.

Lo, Y.L. (2003) Relationships between the hydrophilic-lipophilic balance values of pharmaceutical excipients and their multidrug resistance modulating effect in Caco-2 cells and rat intestines. *J Control Release*, **90**, 37-48.

Lo, Y.L., Hsu, C.Y. and Huang, J.D. (1998) Comparison of effects of surfactants with other MDR reversing agents on intracellular uptake of epirubicin in Caco-2 cell line. *Anticancer Res*, **18**, 3005-3009.

Loe, D.W. and Sharom, F.J. (1993) Interaction of multidrug-resistant Chinese hamster ovary cells with amphiphiles. *Br J Cancer*, **68**, 342-351.

Long, K.S. and Crothers, D.M. (1995) Interaction of human immunodeficiency virus type 1 Tat-derived peptides with TAR RNA. *Biochemistry*, **34**, 8885-8895.

Loo, T.W. and Clarke, D.M. (1998) Nonylphenol ethoxylates, but not nonylphenol, are substrates of the human multidrug resistance P-glycoprotein. *Biochem Biophys Res Commun*, **247**, 478-480.

Lundberg, M. and Johansson, M. (2001) Is VP22 nuclear homing an artifact? *Nature Biotechnology*, **19**, 713-713.

Luo, Y., Madore, S.J., Parslow, T.G., Cullen, B.R. and Peterlin, B.M. (1993) Functional analysis of interactions between Tat and the trans-activation response element of human immunodeficiency virus type 1 in cells. *J Virol*, **67**, 5617-5622.

Lyew, M.A., Mondy, C., Eagle, S. and Chernich, S.E. (2003) Hemodynamic instability and delayed emergence from general anesthesia associated with inadvertent intrathecal baclofen overdose. *Anesthesiology*, **98**, 265-268.

Ma, C.L., Kelly, J.B. and Wu, S.H. (2002) Presynaptic modulation of GABAergic inhibition by GABA(B) receptors in the rat's inferior colliculus. *Neuroscience*, **114**, 207-215.

Mabrouk, K., Van Rietschoten, J., Vives, E., Darbon, H., Rochat, H. and Sabatier, J.M. (1991) Lethal neurotoxicity in mice of the basic domains of HIV and SIV Rev proteins. Study of these regions by circular dichroism. *FEBS Lett*, **289**, 13-17.

MacFarland, A., Abramovich, D.R., Ewen, S.W. and Pearson, C.K. (1994) Stage-specific distribution of P-glycoprotein in first-trimester and full-term human placenta. *Histochem J*, **26**, 417-423.

Mandel, L.J. (1986) Energy-Metabolism of Cellular Activation, Growth, and Transformation. *Current Topics in Membranes and Transport*, **27**, 261-291.

Mandeville, J.B., Marota, J.J., Kosofsky, B.E., Keltner, J.R., Weissleder, R., Rosen, B.R. and Weisskoff, R.M. (1998) Dynamic functional imaging of relative cerebral blood volume during rat forepaw stimulation. *Magn.Reson.Med.*, **39**, 615-624.

Mann, D.A. and Frankel, A.D. (1991) Endocytosis and Targeting of Exogenous Hiv-1 Tat Protein. *Embo Journal*, **10**, 1733-1739.

Mansfield, P. (1977) Multi-Planar Image-Formation Using NMR Spin Echoes. *Journal of Physics C-Solid State Physics*, **10**, L55-L58.

Mansfield, P. and Maudsley, A.A. (1977) Medical Imaging by NMR. *British Journal of Radiology*, **50**, 188-194.

Mansfield, P. and Maudsley, A.A. (1977) Planar Spin Imaging by NMR. *Journal of Magnetic Resonance*, **27**, 101-119.

Martin-Facklam, M., Burhenne, J., Ding, R., Fricker, R., Mikus, G., Walter-Sack, I. and Haefeli, W.E. (2002) Dose-dependent increase of saquinavir bioavailability by the pharmaceutic aid cremophor EL. *Br J Clin Pharmacol*, **53**, 576-581.

Martinho, R.G., Castel, S., Urena, J., FernandezBorja, M., Makiya, R., Olivercrona, G., Reina, M., Alonso, A. and Vilaro, S. (1996) Ligand binding to heparan sulfate proteoglycans induces their aggregation and distribution along actin cytoskeleton. *Molecular Biology of the Cell*, **7**, 1771-1788.

Matta, B.F., Heath, K.J., Tipping, K. and Summors, A.C. (1999) Direct cerebral vasodilatory effects of sevoflurane and isoflurane. *Anesthesiology*, **91**, 677-680.

Mcconnell, H.M., Owicki, J.C., Parce, J.W., Miller, D.L., Baxter, G.T., Wada, H.G. and Pitchford, S. (1992) The Cytosensor Microphysiometer - Biological Applications of Silicon Technology. *Science*, **257**, 1906-1912.

McConnell, H.M., Owicki, J.C., Parce, J.W., Miller, D.L., Baxter, G.T., Wada, H.G. and Pitchford, S. (1992) The cytosensor microphysiometer: biological applications of silicon technology. *Science*, **257**, 1906-1912.

Miller, D.W., Batrakova, E.V. and Kabanov, A.V. (1999) Inhibition of multidrug resistance-associated protein (MRP) functional activity with pluronic block copolymers. *Pharm Res*, **16**, 396-401.

Miller, D.W., Batrakova, E.V., Waltner, T.O., Alakhov, V. and Kabanov, A.V. (1997) Interactions of pluronic block copolymers with brain microvessel endothelial cells: evidence of two potential pathways for drug absorption. *Bioconjug Chem*, **8**, 649-657.

Mitchell, D.J., Kim, D.T., Steinman, L., Fathman, C.G. and Rothbard, J.B. (2000) Polyarginine enters cells more efficiently than other polycationic homopolymers. *Journal of Peptide Research*, **56**, 318-325.

Miyauchi, S., Komatsubara, M. and Kamo, N. (1992) In archaebacteria, there is a doxorubicin efflux pump similar to mammalian P-glycoprotein. *Biochim Biophys Acta*, **1110**, 144-150.

Moon, R.B. and Richards, J.H. (1973) Determination of Intracellular pH by P-31 Magnetic-Resonance. *Journal of Biological Chemistry*, **248**, 7276-7278.

Morad, N., Ryser, H.J.P. and Shen, W.C. (1984) Binding-Sites and Endocytosis of Heparin and Polylysine Are Changed When the 2 Molecules Are Given as a Complex to Chinese-Hamster Ovary Cells. *Biochimica Et Biophysica Acta*, **801**, 117-126.

Moseley, M.E., Chew, W.M., White, D.L., Kucharczyk, J., Litt, L., Derugin, N., Dupon, J., Brasch, R.C. and Norman, D. (1992) Hypercarbia-induced changes in cerebral blood

volume in the cat: a 1H MRI and intravascular contrast agent study. *Magn.Reson.Med.*, **23**, 21-30.

Mueggler, T., Baumann, D., Rausch, M. and Rudin, M. (2001) Bicuculline-induced brain activation in mice detected by functional magnetic resonance imaging. *Magn Reson Med*, **46**, 292-298.

Mueggler, T., Baumann, D., Rausch, M., Staufenbiel, M. and Rudin, M. (2003) Age-dependent impairment of somatosensory response in the amyloid precursor protein 23 transgenic mouse model of Alzheimer's disease. *J Neurosci*, **23**, 8231-8236.

Mueggler, T., Sturchler-Pierrat, C., Baumann, D., Rausch, M., Staufenbiel, M. and Rudin, M. (2002) Compromised hemodynamic response in amyloid precursor protein transgenic mice. *J.Neurosci.2002.Aug.15.;22.(16.):7218.-24.*, **22**, 7218-7224.

Nath, A., Psooy, K., Martin, C., Knudsen, B., Magnuson, D.S.K., Haughey, N. and Geiger, J.D. (1996) Identification of a human immunodeficiency virus type 1 tat epitope that is neuroexcitatory and neurotoxic. *Journal of Virology*, **70**, 1475-1480.

Neff, R.A., Wang, J., Baxi, S., Evans, C. and Mendelowitz, D. (2003) Respiratory sinus arrhythmia: endogenous activation of nicotinic receptors mediates respiratory modulation of brainstem cardioinhibitory parasympathetic neurons. *Circ Res*, **93**, 565-572.

Nervi, P. (2000) "From Soap to Drug Resistance". Role of Detergents as Specific Modulators of ATPase Activity of the Multidrug Transporter: a Novel Approach. *Department of Biophysical Chemistry*. Biozentrum of the University of Basel, 4056 Basel.

Nomarski, G. (1955) Nouveau Dispositif Pour Lobservation En Contraste De Phase Differentiel. *Journal De Physique Et Le Radium*, **16**, S88-S88.

Nori, A., Jensen, K.D., Tijerina, M., Kopeckova, P. and Kopecek, J. (2003) Tat-conjugated synthetic macromolecules facilitate cytoplasmic drug delivery to human ovarian carcinoma cells. *Bioconjug Chem*, **14**, 44-50.

Ogawa, S., Tank, D.W., Menon, R., Ellermann, J.M., Kim, S.G., Merkle, H. and Ugurbil, K. (1992) Intrinsic signal changes accompanying sensory stimulation: functional brain mapping with magnetic resonance imaging. *Proc.Natl.Acad.Sci.U.S.A.*, **89**, 5951-5955.

Okutani, F., Zhang, J.J., Otsuka, T., Yagi, F. and Kaba, H. (2003) Modulation of olfactory learning in young rats through intrabulbar GABA(B) receptors. *Eur J Neurosci*, **18**, 2031-2036.

Olpe, H.R., Demieville, H., Baltzer, V., Bencze, W.L., Koella, W.P., Wolf, P. and Haas, H.L. (1978) The biological activity of d- and l-baclofen (Lioresal). *Eur J Pharmacol*, **52**, 133-136.

Orlowski, S., Selosse, M.A., Boudon, C., Micoud, C., Mir, L.M., Belehradek, J., Jr. and Garrigos, M. (1998) Effects of detergents on P-glycoprotein atpase activity: differences in perturbations of basal and verapamil-dependent activities. *Cancer Biochem Biophys*, **16**, 85-110.

Owicki, J.C. and Parce, J.W. (1992) Biosensors Based on the Energy-Metabolism of Living Cells - the Physical-Chemistry and Cell Biology of Extracellular Acidification. *Biosensors & Bioelectronics*, **7**, 255-272.

Owicki, J.C., Parce, J.W., Kercso, K.M., Sigal, G.B., Muir, V.C., Venter, J.C., Fraser, C.M. and Mcconnell, H.M. (1990) Continuous Monitoring of Receptor-Mediated Changes in the Metabolic Rates of Living Cells. *Proceedings of the National Academy of Sciences of the United States of America*, **87**, 4007-4011.

Parce, J.W., Owicki, J.C., Kercso, K.M., Sigal, G.B., Wada, H.G., Muir, V.C., Bousse, L.J., Ross, K.L., Sikic, B.I. and Mcconnell, H.M. (1989) Detection of Cell-Affecting Agents with a Silicon Biosensor. *Science*, **246**, 243-247.

Petrulis, A. and Eichenbaum, H. (2003) The perirhinal-entorhinal cortex, but not the hippocampus, is critical for expression of individual recognition in the context of the Coolidge effect. *Neuroscience*, **122**, 599-607.

Piekarz, R.L., Cohen, D. and Horwitz, S.B. (1993) Progesterone regulates the murine multidrug resistance mdr1b gene. *J Biol Chem*, **268**, 7613-7616.

Pitsikas, N., Rigamonti, A.E., Cella, S.G. and Muller, E.E. (2003) The GABAB receptor and recognition memory: possible modulation of its behavioral effects by the nitrergic system. *Neuroscience*, **118**, 1121-1127.

Podda, S., Ward, M., Himelstein, A., Richardson, C., Delaflorweiss, E., Smith, L., Gottesman, M., Pastan, I. and Bank, A. (1992) Transfer and Expression of the Human Multiple-Drug Resistance Gene into Live Mice. *Proceedings of the National Academy of Sciences of the United States of America*, **89**, 9676-9680.

Pooga, M., Hallbrink, M., Zorko, M. and Langel, U. (1998) Cell penetration by transportan. *Faseb J*, **12**, 67-77.

Prochiantz, A. (2000) Messenger proteins: homeoproteins, TAT and others. *Curr Opin Cell Biol*, **12**, 400-406.

Purcell, E.M., Torrey, H.C. and Pound, R.V. (1946) Resonance Absorption by Nuclear Magnetic Moments in a Solid. *Physical Review*, **69**, 37-38.

Putman, M., Koole, L.A., van Veen, H.W. and Konings, W.N. (1999) The secondary multidrug transporter LmrP contains multiple drug interaction sites. *Biochemistry*, **38**, 13900-13905.

Rana, T.M. and Jeang, K.T. (1999) Biochemical and functional interactions between HIV-1 Tat protein and TAR RNA. *Arch Biochem Biophys*, **365**, 175-185.

Reese, T., Bjelke, B., Porszasz, R., Baumann, D., Bochelen, D., Sauter, A. and Rudin, M. (2000) Regional brain activation by bicuculline visualized by functional magnetic resonance imaging. Time-resolved assessment of bicuculline-induced changes in local cerebral blood volume using an intravascular contrast agent. *NMR.Biomed.*, **13**, 43-49.

Rege, B.D., Kao, J.P. and Polli, J.E. (2002) Effects of nonionic surfactants on membrane transporters in Caco-2 cell monolayers. *Eur J Pharm Sci*, **16**, 237-246.

Regev, R., Assaraf, Y.G. and Eytan, G.D. (1999) Membrane fluidization by ether, other anesthetics, and certain agents abolishes P-glycoprotein ATPase activity and modulates efflux from multidrug-resistant cells. *Eur J Biochem*, **259**, 18-24.

Riordan, J.R., Deuchars, K., Kartner, N., Alon, N., Trent, J. and Ling, V. (1985) Amplification of P-Glycoprotein Genes in Multidrug-Resistant Mammalian-Cell Lines. *Nature*, **316**, 817-819.

Rischin, D., Webster, L.K., Millward, M.J., Linahan, B.M., Toner, G.C., Woollett, A.M., Morton, C.G. and Bishop, J.F. (1996) Cremophor pharmacokinetics in patients receiving 3-, 6-, and 24-hour infusions of paclitaxel. *J Natl Cancer Inst*, **88**, 1297-1301.

Rizzi, M., Caccia, S., Guiso, G., Richichi, C., Gorter, J.A., Aronica, E., Aliprandi, M., Bagnati, R., Fanelli, R., D'Incalci, M., Samanin, R. and Vezzani, A. (2002) Limbic seizures induce P-glycoprotein in rodent brain: functional implications for pharmacoresistance. *J Neurosci*, **22**, 5833-5839.

Romsicki, Y. and Sharom, F.J. (2001) Phospholipid flippase activity of the reconstituted P-glycoprotein multidrug transporter. *Biochemistry*, **40**, 6937-6947.

Rosen, M.J. (1989) *Surfactants and Interfacial Phenomena*. John Wiley & Sohns, New York.

Rothbard, J.B., Garlington, S., Lin, Q., Kirschberg, T., Kreider, E., McGrane, P.L., Wender, P.A. and Khavari, P.A. (2000) Conjugation of arginine oligomers to cyclosporin A facilitates topical delivery and inhibition of inflammation. *Nat Med*, **6**, 1253-1257.

Rudin, M., Beckmann, N., Porszasz, R., Reese, T., Bochelen, D. and Sauter, A. (1999) In vivo magnetic resonance methods in pharmaceutical research: current status and perspectives. *NMR.Biomed.*, **12**, 69-97.

Rudin, M., Beckmann, N. and Sauter, A. (1997) Analysis of tracer transit in rat brain after carotid artery and femoral vein administrations using linear system theory. *Magn.Reson.Imaging*, **15**, 551-558.

Rusnati, M., Coltrini, D., Oreste, P., Zoppetti, G., Albini, A., Noonan, D., d'Adda di Fagagna, F., Giacca, M. and Presta, M. (1997) Interaction of HIV-1 Tat protein with heparin. Role of the backbone structure, sulfation, and size. *J Biol Chem*, **272**, 11313-11320.

Ryser, H.J.P. (1968) Uptake of Protein by Mammalian Cells - an Underdeveloped Ares - Penetration of Foreign Proteins into Mammalian Cells Can Be Measured and Their Functions Explored. *Science*, **159**, 390-&.

Sabatier, J.M., Vives, E., Mabrouk, K., Benjouad, A., Rochat, H., Duval, A., Hue, B. and Bahraoui, E. (1991) Evidence for neurotoxic activity of tat from human immunodeficiency virus type 1. *J Virol*, **65**, 961-967.

Saha, N., Chugh, Y., Sankaranaryanan, A. and Sharma, P.L. (1993) Effects of post-training administration of (-)-baclofen and chlordiazepoxide on memory retention in ICRC Swiss mice: interactions with GABAA and GABAB receptor antagonists. *Pharmacol Toxicol*, **72**, 159-162.

Saito, T., Yamamoto, I., Huang, X.L., Yukawa, N., Osawa, M. and Takeichi, S. (1999) Effects of muscle relaxants on EEG, ABR and EMG in rabbits. *Hum Exp Toxicol*, **18**, 718-723.

Sandgren, S., Cheng, F. and Belting, M. (2002) Nuclear targeting of macromolecular polyanions by an HIV-Tat derived peptide. Role for cell-surface proteoglycans. *J Biol Chem*, **277**, 38877-38883.

Sauna, Z.E. and Ambudkar, S.V. (2000) Evidence for a requirement for ATP hydrolysis at two distinct steps during a single turnover of the catalytic cycle of human P-glycoprotein. *Proc Natl Acad Sci U S A*, **97**, 2515-2520.

Sauna, Z.E., Andrus, M.B., Turner, T.M. and Ambudkar, S.V. (2004) Biochemical basis of polyvalency as a strategy for enhancing the efficacy of P-glycoprotein (ABCB1) modulators: stipiamide homodimers separated with defined-length spacers reverse drug efflux with greater efficacy. *Biochemistry*, **43**, 2262-2271.

Scheffler, K., Seifritz, E., Haselhorst, R. and Bilecen, D. (1999) Titration of the BOLD effect: separation and quantitation of blood volume and oxygenation changes in the human cerebral cortex during neuronal activation and ferumoxide infusion. *Magn.Reson.Med.*, **42**, 829-836.

Schinkel, A.H., Arceci, R.J., Smit, J.J., Wagenaar, E., Baas, F., Dolle, M., Tsuruo, T., Mechetner, E.B., Roninson, I.B. and Borst, P. (1993) Binding properties of monoclonal antibodies recognizing external epitopes of the human MDR1 P-glycoprotein. *Int J Cancer*, **55**, 478-484.

Schinkel, A.H., Wagenaar, E., Mol, C.A. and van Deemter, L. (1996) P-glycoprotein in the blood-brain barrier of mice influences the brain penetration and pharmacological activity of many drugs. *J Clin Invest*, **97**, 2517-2524.

Schuldes, H., Dolderer, J.H., Zimmer, G., Knobloch, J., Bickeboller, R., Jonas, D. and Woodcock, B.G. (2001) Reversal of multidrug resistance and increase in plasma membrane fluidity in CHO cells with R-verapamil and bile salts. *Eur J Cancer*, **37**, 660-667.

Schuler, V., Luscher, C., Blanchet, C., Klix, N., Sansig, G., Klebs, K., Schmutz, M., Heid, J., Gentry, C., Urban, L., Fox, A., Spooren, W., Jaton, A.L., Vigouret, J., Pozza, M., Kelly, P.H., Mosbacher, J., Froestl, W., Kaslin, E., Korn, R., Bischoff, S., Kaupmann,

K., van der Putten, H. and Bettler, B. (2001) Epilepsy, hyperalgesia, impaired memory, and loss of pre- and postsynaptic GABA(B) responses in mice lacking GABA(B(1)). *Neuron*, **31**, 47-58.

Schulz, J.G., Megow, D., Reszka, R., Villringer, A., Einhaupl, K.M. and Dirnagl, U. (1998) Evidence that glypican is a receptor mediating beta-amyloid neurotoxicity in PC12 cells. *European Journal of Neuroscience*, **10**, 2085-2093.

Schwarze, S.R., Ho, A., Vocero-Akbani, A. and Dowdy, S.F. (1999) In vivo protein transduction: delivery of a biologically active protein into the mouse. *Science*, **285**, 1569-1572.

Schwarze, S.R., Hruska, K.A. and Dowdy, S.F. (2000) Protein transduction: unrestricted delivery into all cells? *Trends in Cell Biology*, **10**, 290-295.

Seelig, A. (1987) Local-Anesthetics and Pressure - a Comparison of Dibucaine Binding to Lipid Monolayers and Bilayers. *Biochimica Et Biophysica Acta*, **899**, 196-204.

Seelig, A. (1998) A general pattern for substrate recognition by P-glycoprotein. *Eur J Biochem*, **251**, 252-261.

Seelig, A. (1998) A general pattern for substrate recognition by P-glycoprotein. *European Journal of Biochemistry*, **251**, 252-261.

Seelig, A., Blatter, X.L. and Wohnsland, F. (2000) Substrate recognition by P-glycoprotein and the multidrug resistance-associated protein MRP1: a comparison. *International Journal of Clinical Pharmacology and Therapeutics*, **38**, 111-121.

Seelig, A., Gatlik, E., Fischer, H. and Li-Blatter, X. (2005) Inhibitors of Multidrug Efflux Transporters: Their Membrane and Protein Interactions. *Mini-Reviews in Medicinal Chemistry*, **5**.

Seelig, A., Gottschlich, R. and Devant, R.M. (1994) A Method to Determine the Ability of Drugs to Diffuse through the Blood-Brain-Barrier. *Proceedings of the National Academy of Sciences of the United States of America*, **91**, 68-72.

Seelig, A. and Landwojtowicz, E. (2000) Structure-activity relationship of P-glycoprotein substrates and modifiers. *Eur J Pharm Sci*, **12**, 31-40.

Sehested, M., Jensen, P.B., Skovsgaard, T., Bindslev, N., Demant, E.J., Friche, E. and Vindelov, L. (1989) Inhibition of vincristine binding to plasma membrane vesicles from daunorubicin-resistant Ehrlich ascites cells by multidrug resistance modulators. *Br J Cancer*, **60**, 809-814.

Sharma, A.C. and Kulkarni, S.K. (1993) (+/-)Baclofen sensitive scopolamine-induced short-term memory deficits in mice. *Indian J Exp Biol*, **31**, 348-352.

Silhol, M., Tyagi, M., Giacca, M., Lebleu, B. and Vives, E. (2002) Different mechanisms for cellular internalization of the HIV-1 Tat-derived cell penetrating peptide and recombinant proteins fused to Tat. *European Journal of Biochemistry*, **269**, 494-501.

Silva, A.C., Lee, S.P., Yang, G., Iadecola, C. and Kim, S.G. (1999) Simultaneous blood oxygenation level-dependent and cerebral blood flow functional magnetic resonance imaging during forepaw stimulation in the rat. *J.Cereb.Blood Flow Metab.*, **19**, 871-879.

Silverman, J.A. and Schrenk, D. (1997) Hepatic canalicular membrane 4: expression of the multidrug resistance genes in the liver. *Faseb J*, **11**, 308-313.

Simon, W., Hapfelmeier, G., Kochs, E., Zieglgansberger, W. and Rammes, G. (2001) Isoflurane blocks synaptic plasticity in the mouse hippocampus. *Anesthesiology*, **94**, 1058-1065.

Sodroski, J., Patarca, R., Rosen, C., Wong-Staal, F. and Haseltine, W. (1985) Location of the trans-activating region on the genome of human T-cell lymphotropic virus type III. *Science*, **229**, 74-77.

Soomets, U., Lindgren, M., Gallet, X., Hallbrink, M., Elmquist, A., Balaspiri, L., Zorko, M., Pooga, M., Brasseur, R. and Langel, U. (2000) Deletion analogues of transportan. *Biochim Biophys Acta*, **1467**, 165-176.

Stackman, R.W. and Walsh, T.J. (1994) Baclofen produces dose-related working memory impairments after intraseptal injection. *Behav Neural Biol*, **61**, 181-185.

Stein, S., Weiss, A., Adermann, K., Lazarovici, P., Hochman, J. and Wellhoner, H. (1999) A disulfide conjugate between anti-tetanus antibodies and HIV (37-72)Tat neutralizes tetanus toxin inside chromaffin cells. *FEBS Lett*, **458**, 383-386.

Sturm, A., Cravedi, J.P. and Segner, H. (2001) Prochloraz and nonylphenol diethoxylate inhibit an mdr1-like activity in vitro, but do not alter hepatic levels of P-glycoprotein in trout exposed in vivo. *Aquat Toxicol*, **53**, 215-228.

Sugimura, M., Kitayama, S., Morita, K., Imai, Y., Irifune, M., Takarada, T., Kawahara, M. and Dohi, T. (2002) Effects of GABAergic agents on anesthesia induced by halothane, isoflurane, and thiamylal in mice. *Pharmacol Biochem Behav*, **72**, 111-116.

Sugimura, M., Kitayama, S., Morita, K., Irifune, M., Takarada, T., Kawahara, M. and Dohi, T. (2001) Effects of volatile and intravenous anesthetics on the uptake of GABA, glutamate and dopamine by their transporters heterologously expressed in COS cells and in rat brain synaptosomes. *Toxicol Lett*, **123**, 69-76.

Suzuki, M., Tetsuka, M. and Endo, M. (1999) GABA(B) receptors in the nucleus tractus solitarii modulate the carotid chemoreceptor reflex in rats. *Neurosci Lett*, **260**, 21-24.

Suzuki, T., Futaki, S., Niwa, M., Tanaka, S., Ueda, K. and Sugiura, Y. (2002) Possible existence of common internalization mechanisms among arginine-rich peptides. *Journal of Biological Chemistry*, **277**, 2437-2443.

Sved, A.F. and Tsukamoto, K. (1992) Tonic stimulation of GABAB receptors in the nucleus tractus solitarius modulates the baroreceptor reflex. *Brain Res*, **592**, 37-43.

ten Tije, A.J., Verweij, J., Loos, W.J. and Sparreboom, A. (2003) Pharmacological effects of formulation vehicles: implications for cancer chemotherapy. *Clin Pharmacokinet*, **42**, 665-685.

Teter, C.J. and Guthrie, S.K. (2001) A comprehensive review of MDMA and GHB: two common club drugs. *Pharmacotherapy*, **21**, 1486-1513.

Thiebaut, F., Tsuruo, T., Hamada, H., Gottesman, M.M., Pastan, I. and Willingham, M.C. (1987) Cellular localization of the multidrug-resistance gene product P-glycoprotein in normal human tissues. *Proc Natl Acad Sci U S A*, **84**, 7735-7738.

Thiebaut, F., Tsuruo, T., Hamada, H., Gottesman, M.M., Pastan, I. and Willingham, M.C. (1989) Immunohistochemical localization in normal tissues of different epitopes in the multidrug transport protein P170: evidence for localization in brain capillaries and crossreactivity of one antibody with a muscle protein. *J Histochem Cytochem*, **37**, 159-164.

Thomas, D.L., Lythgoe, M.F., Calamante, F., Gadian, D.G. and Ordidge, R.J. (2001) Simultaneous noninvasive measurement of CBF and CBV using double-echo FAIR (DEFAIR). *Magn Reson Med*, **45**, 853-863.

Tishler, D.M., Weinberg, K.I., Hinton, D.R., Barbaro, N., Annett, G.M. and Raffel, C. (1995) MDR1 gene expression in brain of patients with medically intractable epilepsy. *Epilepsia*, **36**, 1-6.

Torchilin, V.P., Rammohan, R., Weissig, V. and Levchenko, T.S. (2001) TAT peptide on the surface of liposomes affords their efficient intracellular delivery even at low temperature and in the presence of metabolic inhibitors. *Proc Natl Acad Sci U S A*, **98**, 8786-8791.

Trippenbach, T. (1995) Baclofen-induced block of the Hering-Breuer expiratory-promoting reflex in rats. *Can J Physiol Pharmacol*, **73**, 706-713.

Trippenbach, T. and Lake, N. (1994) Excitatory cardiovascular and respiratory effects of baclofen in intact rats. *Can J Physiol Pharmacol*, **72**, 1200-1207.

Turnbull, J.E. and Gallagher, J.T. (1991) Distribution of Iduronate 2-Sulfate Residues in Heparan-Sulfate - Evidence for an Ordered Polymeric Structure. *Biochemical Journal*, **273**, 553-559.

Tyagi, M., Rusnati, M., Presta, M. and Giacca, M. (2001) Internalization of HIV-1 Tat requires cell surface heparan sulfate proteoglycans. *Journal of Biological Chemistry*, **276**, 3254-3261.

Ullman, B. (1995) Multidrug resistance and P-glycoproteins in parasitic protozoa. *J Bioenerg Biomembr*, **27**, 77-84.

Urbatsch, I.L., Sankaran, B., Weber, J. and Senior, A.E. (1995) P-Glycoprotein Is Stably Inhibited by Vanadate-Induced Trapping of Nucleotide at a Single Catalytic Site. *Journal of Biological Chemistry*, **270**, 19383-19390.

Van Bambeke, F., Balzi, E. and Tulkens, P.M. (2000) Antibiotic efflux pumps. *Biochem Pharmacol*, **60**, 457-470.

Van Bambeke, F., Glupczynski, Y., Plesiat, P., Pechere, J.C. and Tulkens, P.M. (2003) Antibiotic efflux pumps in prokaryotic cells: occurrence, impact on resistance and strategies for the future of antimicrobial therapy. *J Antimicrob Chemother*, **51**, 1055-1065.

Van Bambeke, F., Michot, J.M. and Tulkens, P.M. (2003) Antibiotic efflux pumps in eukaryotic cells: occurrence and impact on antibiotic cellular pharmacokinetics, pharmacodynamics and toxicodynamics. *J Antimicrob Chemother*, **51**, 1067-1077.

van Zuylen, L., Verweij, J. and Sparreboom, A. (2001) Role of formulation vehicles in taxane pharmacology. *Invest New Drugs*, **19**, 125-141.

Villringer, A., Rosen, B.R., Belliveau, J.W., Ackerman, J.L., Lauffer, R.B., Buxton, R.B., Chao, Y.S., Wedeen, V.J. and Brady, T.J. (1988) Dynamic Imaging With Lanthanide Chelates in Normal Brain - Contrast Due to Magnetic-Susceptibility Effects. *Magnetic Resonance in Medicine*, **6**, 164-174.

Vives, E., Brodin, P. and Lebleu, B. (1997) A truncated HIV-1 Tat protein basic domain rapidly translocates through the plasma membrane and accumulates in the cell nucleus. *Journal of Biological Chemistry*, **272**, 16010-16017.

Wan, H., Aggleton, J.P. and Brown, M.W. (1999) Different contributions of the hippocampus and perirhinal cortex to recognition memory. *J Neurosci*, **19**, 1142-1148.

Warburg, O. (1926) *Uber den Stoffwechsel der Tumoren.* Springer Verlag, Berlin.

Weeks, K.M., Ampe, C., Schultz, S.C., Steitz, T.A. and Crothers, D.M. (1990) Fragments of the HIV-1 Tat protein specifically bind TAR RNA. *Science*, **249**, 1281-1285.

Weis, K. (2003) Regulating access to the genome: nucleocytoplasmic transport throughout the cell cycle. *Cell*, **112**, 441-451.

Wender, P.A., Rothbard, J.B., Jessop, T.C., Kreider, E.L. and Wylie, B.L. (2002) Oligocarbamate molecular transporters: design, synthesis, and biological evaluation of a new class of transporters for drug delivery. *J Am Chem Soc*, **124**, 13382-13383.

Willker, W., Engelmann, J., Brand, A. and Leibfritz, D. (1995) Identification of Pyro-Glutamate and Glucosyl-Aminoacids in cell culture media. *J. Magn. Res. Anal*, **1**, 20-24.

Wirsching, S., Michel, S. and Morschhauser, J. (2000) Targeted gene disruption in Candida albicans wild-type strains: the role of the MDR1 gene in fluconazole resistance of clinical Candida albicans isolates. *Mol Microbiol*, **36**, 856-865.

Wong, C.G., Gibson, K.M. and Snead, O.C., 3rd. (2004) From the street to the brain: neurobiology of the recreational drug gamma-hydroxybutyric acid. *Trends Pharmacol Sci*, **25**, 29-34.

Wood, G.W., Dumoulin, C.L., Souza, S.P., Hart, H.R., Wagle, W.A. and Eames, F.A. (1987) Magnetic-Resonance Angiography of Craniocervical Vascular- Lesions. *American Journal of Neuroradiology*, **8**, 957-957.

Woodcock, D.M., Linsenmeyer, M.E., Chojnowski, G., Kriegler, A.B., Nink, V., Webster, L.K. and Sawyer, W.H. (1992) Reversal of multidrug resistance by surfactants. *Br J Cancer*, **66**, 62-68.

Zastre, J., Jackson, J., Bajwa, M., Liggins, R., Iqbal, F. and Burt, H. (2002) Enhanced cellular accumulation of a P-glycoprotein substrate, rhodamine-123, by Caco-2 cells using low molecular weight methoxypolyethylene glycol-block-polycaprolactone diblock copolymers. *Eur J Pharm Biopharm*, **54**, 299-309.

Zhang, Y. and Wu, S.H. (2000) Long-term potentiation in the inferior colliculus studied in rat brain slice. *Hear Res*, **147**, 92-103.

Zhao, M. and Weissleder, R. (2004) Intracellular cargo delivery using tat peptide and derivatives. *Med Res Rev*, **24**, 1-12.

Ziegler, A., Blatter, X.L., Seelig, A. and Seelig, J. (2003) Protein transduction domains of HIV-1 and SIV TAT interact with charged lipid vesicles. Binding mechanism and thermodynamic analysis. *Biochemistry*, **42**, 9185-9194.

Ziegler, A. and Seelig, J. (2004) Interaction of the Protein Transduction Domain of HIV-1 TAT with Heparan Sulfate: Binding Mechanism and Thermodynamic Parameters. *Biophys J*, **86**, 254-263.

Zielke, H.R., Zielke, C.L. and Ozand, P.T. (1984) Glutamine - a Major Energy-Source for Cultured Mammalian-Cells. *Federation Proceedings*, **43**, 121-125.

Zordan-Nudo, T., Ling, V., Liu, Z. and Georges, E. (1993) Effects of nonionic detergents on P-glycoprotein drug binding and reversal of multidrug resistance. *Cancer Res*, **53**, 5994-6000.

# Acknowledgements

Many thanks go to the following persons:

PD Dr. Anna Seelig for directing the P-glycoprotein project and for proposing to me to work as special volunteer at NIH.

Prof. Dr. Joachim Seelig, who supported me and warmly proposed to me to continue my thesis with the TAT and fMRI projects.

Dr. André Ziegler, who leaded the TAT project and teached me MRI. He has been an example for me, with his friendship, modesty, professionalism, eclectic competences and his uncommonly generous help.

PD Dr. Markus Rudin and his coworkers at Novartis Pharma AG: Dr. Nicolau Beckman, Dr. Martin Rausch and especially Dr. Thomas Müggler, for the precious help in fMRI data analysis.

The people that, like me, invested a lot of time for the development and improvement of the Cytosensor technique for the study of P-glycoprotein: Holger Fisher and Ewa Landwojtowicz.

The members of the research group of Joachim and Anna Seelig and people from the department of biophysical chemistry, in particular Gunnar Karelson, Bernhard Steinbauer, Sandro Keller, Gregory Gerebtzoff, Thomas Ahrens, Simon Hellstern, Heiko Heerklotz.

Roland Geiser and René Zedi, for their important work with laboratory animals.

Leo Faletti, Gernot Hänisch, Hans Vogt, Franz Biry and Ralf for the nice technical assistance.

Dr. Michael Gottesman, Dr. Suresh Ambudkar, Carol Cardarelli and all the group members of the laboratory of cell biology at the National Cancer Institute, NIH, Bethesda (MD), USA.

Prof. Dr. Bernhard Bettler and coworkers, for providing the mice for the fMRI project.

Prof. Dr. Andreas Lüthi, for the interesting comments.

The Lions Club Alto Ticino, for the financial support.

Dr. Lorenzo Mauri, for his brilliant and inspiring comments and his friendship.

All the other people who were near to me in this period, in particular Teo, Andrea, Chantal, Boris, Eric, Sergio, Laura, Alessandro, Lucia, Bonnie, Johanna, John, Dennis, Lara, Caterina, Joel, Lorenzo, Belinda, Suraj, Philippe, Christian, Stefano, Benedetta, Martina, Nadia and the many others that I forgot to mention.

My family, Anna, Alfredo, Rosaria and Julian, for their precious help, patience and love.

My PhD title will be dedicated to all young idealist people who could not realize their wishes, and in particular to the memory of my dear friend Federico Ducci.